The Astrophysical Journal, 947:25 (62pp), 2023 April 10 https://doi.org/10.3847/1538-4357/acba13

The Evolution of Protostellar Outflow Cavities, Kinematics, and Angular Distribution of Momentum and Energy in Orion A: Evidence for Dynamical Cores

Cheng-Han Hsieh (謝承翰)[1], Héctor G. Arce[1], Zhi-Yun Li[2], Michael Dunham[3], Stella Offner[4], Ian W. Stephens[5], Amelia Stutz[6], Tom Megeath[7], Shuo Kong[8], Adele Plunkett[9], John J. Tobin[9], Yichen Zhang[2,10], Diego Mardones[11], Jaime E. Pineda[12], Thomas Stanke[13], and John Carpenter[14]
[1] Department of Astronomy, Yale University, New Haven, CT 06511, USA; cheng-han.hsieh@yale.edu
[2] Department of Astronomy, University of Virginia, Charlottesville, VA 22904, USA
[3] Department of Physics, State University of New York at Fredonia, Fredonia, NY 14063, USA
[4] Department of Astronomy, University of Texas at Austin, Austin, TX 78712-1710, USA
[5] Department of Earth, Environment, and Physics, Worcester State University, Worcester, MA 01602, USA
[6] Departamento de Astronomía, Universidad de Concepción, Concepción, Chile
[7] Department of Astronomy, University of Toledo, Toledo, OH 43606, USA
[8] Department of Astronomy and Steward Observatory, University of Arizona, Tucson, AZ 85721, USA
[9] National Radio Astronomy Observatory, 520 Edgemont Road, Charlottesville, VA 22903, USA
[10] RIKEN Cluster for Pioneering Research, Wako, Saitama 351-0198, Japan
[11] Departamento de Astronomía, Universidad de Chile, Región Metropolitana, Chile
[12] The Center for Astrochemical Studies, Max Planck Institute for Extraterrestrial Physics, Garching bei München D-85748, Germany
[13] Max Planck Institute for Extraterrestrial Physics, Gießenbachstraße 1, D-85748 Garching, Germany
[14] Joint ALMA Observatory (JAO), Santiago, Chile
Received 2022 September 21; revised 2023 February 3; accepted 2023 February 6; published 2023 April 14

Abstract

We present Atacama Large Millimeter/submillimeter Array observations of the ∼10,000 au environment surrounding 21 protostars in the Orion A molecular cloud tracing outflows. Our sample is composed of Class 0 to flat-spectrum protostars, spanning the full ∼1 Myr lifetime. We derive the angular distribution of outflow momentum and energy profiles and obtain the first two-dimensional instantaneous mass, momentum, and energy ejection rate maps using our new approach: the pixel flux-tracing technique. Our results indicate that by the end of the protostellar phase, outflows will remove ∼2–4 $M_{\odot}$ from the surrounding ∼1 $M_{\odot}$ low-mass core. These high values indicate that outflows remove a significant amount of gas from their parent cores and continuous core accretion from larger scales is needed to replenish core material for star formation. This poses serious challenges to the concept of *cores as well-defined mass reservoirs*, and hence to the simplified core-to-star conversion prescriptions. Furthermore, we show that cavity opening angles, and momentum and energy distributions all increase with protostar evolutionary stage. This is clear evidence that even garden-variety protostellar outflows: (a) effectively inject energy and momentum into their environments on 10,000 au scales, and (b) significantly disrupt their natal cores, ejecting a large fraction of the mass that would have otherwise fed the nascent star. Our results support the conclusion that protostellar outflows have a direct impact on how stars get their mass, and that the natal sites of individual low-mass star formation are far more dynamic than commonly accepted theoretical paradigms.

Unified Astronomy Thesaurus concepts: Star formation (1569); Protostars (1302); Stellar feedback (1602); Giant molecular clouds (653); Stellar-interstellar interactions (1576); Stellar winds (1636); Stellar jets (1607); Star forming regions (1565); Observational astronomy (1145); Radio interferometry (1346); Circumstellar envelopes (237); Circumstellar matter (241)

1. Introduction

Protostellar outflows are one of the most important ingredients of star formation for a variety of reasons. In particular, outflows are believed to be one of the main mechanisms that help disperse the protostellar core and terminate the infall phase, and assist in the removal of disk angular momentum, which drives accretion (Machida & Hosokawa 2013; Frank et al. 2014; Offner & Arce 2014; Bally 2016). Through these processes, outflows impact the mass-assembly process, the final masses of stars, and the initial mass function (IMF; Alves et al. 2007; Arce et al. 2007; Guszejnov et al. 2021; Pascucci et al. 2022).

Comparing the core mass function (CMF) with the IMF suggests that the mass of stars strongly depends on the mass of their parent cores with a core-to-star efficiency of about 30% (e.g., Motte et al. 1998, 2001; Testi & Sargent 1998; Stanke et al. 2006; Alves et al. 2007; Enoch et al. 2008; André et al. 2010; Könyves et al. 2015; Motte et al. 2022, and references therein). If gas dispersal by outflows is the main cause of this relatively low efficiency, then this would imply that outflows are capable of dispersing about 70% of the cores' mass. Some observations have shown outflows have enough energy and momentum to disperse the material in the surrounding parent core within 1 Myr (Dunham et al. 2014; Zhang et al. 2016). In addition, a number of studies have found that the outflow opening angle broadens with time (Arce & Sargent 2006;

Velusamy et al. 2014; Hsieh et al. 2017), thereby facilitating the gas clearing process in the surrounding envelope.

On the other hand, other studies have shown that outflow mass-loss rates are too low to be the main agent of core dispersal (Hatchell et al. 2007; Curtis et al. 2010). A recent study of outflow cavities using Hubble Space Telescope (HST) near-IR (NIR) images of the scattered light around protostars in Orion found no evidence for the widening of outflow cavities as protostars evolve (Habel et al. 2021). Their results indicate that gas dispersal by outflows cannot be the main process that produces the low star formation efficiency of 30%. However, there are no other known mechanisms that can explain the low star formation efficiency in cores.

Resolving this problem, requires characterizing outflows based on their structure and morphology (e.g., opening angle), as well as other physical properties (e.g., mass, momentum, and energy loss rate) and linking them to their evolutionary status. Although outflows have been studied since the early 1980s (Snell et al. 1980; Solomon et al. 1981), they remain complicated systems for which accurate measurements of their physical properties and their evolutionary stage are hard to ascertain without high angular resolution, high dynamic range observations of sizeable samples of sources.

In this paper, to address the problems above, we use a method to obtain accurate outflow properties. This involves a new method that we call the pixel flux-tracing (PFT) technique as well as a modified version of an annulus method developed by Bontemps et al. (1996). We also use our sensitive observations to derive outflow momentum and energy opening angles. With this information, we establish a powerful new technique for observing outflow–core interaction that complements traditional opening angles in determining how much core material is impacted by the outflow.

To study the protostellar outflow–core interactions, we use the Atacama Large Millimeter/submillimeter Array (ALMA) to survey protostars at different evolutionary stages in the Orion A molecular cloud. The Orion A giant molecular cloud (GMC) is the closest star-forming region that harbors both high and low-mass star formation. This GMC is at a distance of about 400 pc and has a gas mass of about $10^5\,M_\odot$ (Bally 2008). The cloud and the young stellar sources in it have been studied extensively with large, multiwavelength, surveys covering multiple scales, (e.g., Megeath et al. 2012, 2016; Stutz et al. 2013; Furlan et al. 2016; Kong et al. 2018; Fischer et al. 2020; Tobin et al. 2020; Stanke et al. 2022). The availability of these rich data sets makes Orion A a perfect target to study outflow evolution and its impact on protostellar cores.

In Section 2, we describe the sample selection for this study. In Section 3, we describe the observational data, the calibration, and the imaging process. In Section 4, we describe the methods we use to obtain outflow properties and show the results of our observations. In Section 5, we analyze and discuss the evolution of the outflow properties (opening angle, mass, momentum, and energy ejection rate) and the impact on cores. In Section 6, we summarize the main findings and give our conclusions.

2. Sample Selection

Our survey consists of 21 protostellar sources evenly distributed in three different evolutionary stages: Class 0, Class I, and flat spectrum. The sources were all observed by the Herschel Orion Protostar Survey (HOPS), from which we obtain the derived properties of the protostars, including evolutionary class, bolometric temperature, and luminosity (Furlan et al. 2016). All sources are located in the northern part of the L1641 region, a relatively low-density star-forming region south of the Orion Nebula Cluster, that is far (at least ~8 pc) from high-mass protostars and photodissociation regions. The positions of the sources are overplotted on the Herschel-Planck dust opacity map at 353 GHz from Lombardi et al. (2014) in Figure 1. The blue-filled circles, red triangles, and green squares mark the positions of Class 0, Class I, and flat-spectrum sources.

We chose targets that were thought to have no binary or multiple companions by the time we submitted the observing proposal, and to be relatively isolated with no neighboring young stellar objects (YSOs) closer than 0.12 pc (60.″0), in order to avoid possible contamination from nearby outflows. Only one source in our sample (HOPS 150) was recently discovered to be part of a binary system with a projected binary separation of ~3.″0 (~1200 au Tobin et al. 2020, 2022). All sources have been observed in the NIR by the VISTA Orion A Survey and at 1.6–870 μm with the Hubble, Spitzer, and Herschel space telescopes (e.g., Megeath et al. 2012; Furlan et al. 2016; Kounkel et al. 2016). In addition, the sample spans a limited range in $L_{\rm bol}$ (~0.4–15) and this range is comparable in all three evolutionary classes. A summary of the source properties is shown in Table 1.

3. Observations

The results presented here come from Cycle 6 ALMA multiline observations of the environment around protostars in the the Orion A cloud (Project ID: 2018.1.00744.S, PI: H. Arce). The observations were conducted using ALMA Band 6, which simultaneously observed the 1.29 mm dust continuum emission and the following six molecular lines, which trace different density and kinematic regimes: ^{12}CO(2–1), ^{13}CO(2–1), C^{18}O(2–1), $H_2CO(3_{0,3}–2_{0,2})$, SiO(5–4), and N_2D^+(3–2).

In this paper, we concentrate on the ^{12}CO(2–1), ^{13}CO(2–1), and C^{18}O(2–1) lines, which have rest frequencies of 230.53800, 220.39868, and 219.56035 GHz, respectively. After H_2, ^{12}CO is the most abundant molecule in molecular clouds, and is typically the most easily observed since H_2 lacks dipole rotational transitions. Together with the less abundant ^{13}CO and C^{18}O they trace regions across a wide range of (column) densities ($5 \leqslant A_v \leqslant 15$) (Gratier et al. 2021). We use these three CO isotopologues to probe the outflow properties. The other lines we observed that trace the infalling gas, energetic jets, and cold, and warm core regions will be presented in forthcoming papers.

Each source in our sample was observed using a 12 m array seven-pointing mosaic (in the C43-2 configuration), and a three-pointing mosaic using the 7 m array. This allowed us to cover the environment surrounding each source over a region of about 0.1 pc or ~50.″0 and ensured the maps had an approximately uniform sensitivity within the primary beam of the 12 m array at the observed frequencies, about 25″ (~0.05 pc), centered at the source.

The 12 m array observations were made between 2018 December 21 and 2019 January 15, and consisted of 15 executions, with an on-source integration of 35.4 minutes for each of the seven-pointing mosaics used to cover each source. J0423-0120 was used for bandpass and flux calibration and J0542-0913 was used for phase calibration. Between 45 and 50

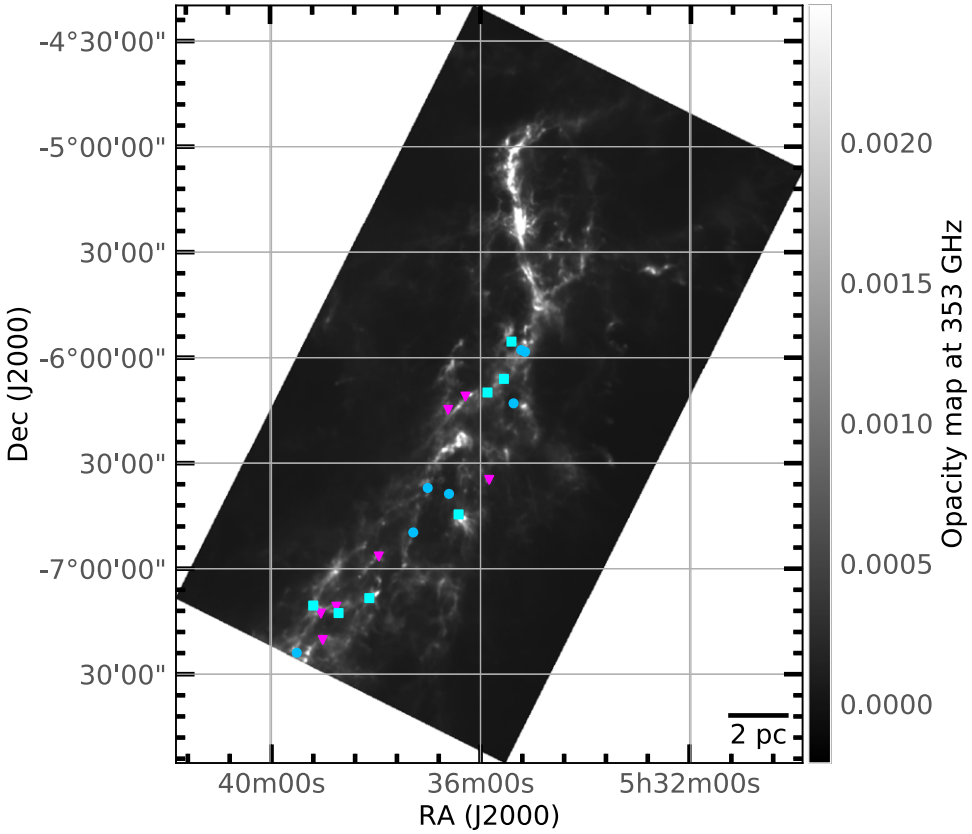

Figure 1. Sources from this survey overplotted on the Orion A Herschel-Planck dust opacity map at 353 GHz (Lombardi et al. 2014). The blue-filled circles, red triangles, and green squares mark the position of Class 0, Class I, and flat-spectrum sources, respectively.

antennas were used on different observation dates, which included baselines ranging from about 15.1–500.2 m, which sample scales between 1.″1 and 16.″2 (440 and 6480 au). The 7 m array observations, which were conducted using 70 executions between 2018 October 3 and 2018 November 23, used J0522-3627 for bandpass and flux calibration and J0501-0159 for the phase calibration. The average 7 m array integration time for each 3-pointing mosaic around each source in our sample was 2 hr and 20.5 minutes. These observations used between nine and 12 antennas that included baselines ranging from approximately 8.9–48.9 m, sampling scales between 5.″5 and 29.″0 (2200–11,600 au).

We also obtained total power (TP) array data for our observations to trace the large-scale emission structure and recover all flux from the molecular line emission toward our sources of interest. The TP observations were conducted between 2018 September 19 and 2019 January 8, and provided 98.″0 by 96.″0 on-the-fly maps centered on each source. The on-source time for each of these maps was 6 hr and 51.6 minutes.

The pipeline in the Common Astronomy Software Applications (CASA) version 5.4.0-70 was used to calibrate the ALMA data. Additional data flagging was performed by the North American ALMA Science Center to remove artifacts in the 12 m continuum data caused by insufficient sampling at the shortest baselines.

We used the CASA task *tclean* to image the combined 12 and 7 m array interferometer data. We ran this task with automasking, which automatically defines different cleaning regions for each channel, and may vary for different iterations. The deconvolver option was set to hogbom, which proved to be more stable than the multiscale option, which produced artifacts in many cases. We also set the velocity resolution parameter to −1, which ensures the output cleaned maps have the same velocity resolution as the original *uv* data: 0.079 km s^{-1} for ^{12}CO (2–1), and 0.083 km s^{-1} for ^{13}CO and C^{18}O (2–1). We set the cyclefactor parameter to 2.0 to terminate the minor cycle (deconvolving the observed image from the telescope beam) faster and trigger the next major cycle. The criteria for stopping a minor cycle in *tclean* is set by the product of peak residual level, maximum point-spread function sidelobe level, and the value of the cyclefactor parameter. Using the default value for the cyclefactor parameter (1.0) caused the minor cycle to generate artifacts at the low sensitivity edge of our mosaics. Such artifacts did not appear (i.e., the algorithm would be stable) only when both the *cyclefactor* was set to a value equal to or greater than 2, and *automasking* was turned on. For imaging, we used natural weighting to maximize the signal-to-noise ratio (S/N) while maintaining a similar beam size of about 1.″1 for all line maps. Primary beam correction was applied to each map resulting in higher noise at the edge of the mosaic maps.

We then used the CASA task *Feather* to combine the array data with the TP data. The resulting synthesized beam size, velocity resolution, and the average rms noise level of the CO, ^{13}CO, and C^{18}O maps are shown in Table 2.

Table 1
Summary of Source Properties

Source	R.A. (J2000)	Decl. (J2000)	Distance[a] (pc)	V_{syst}[b] (km s^{-1})	T_{bol}[c] (K)	Class[c]	L_{bol}[c] ($L_\odot$)	ALMA Core Mass ($M_\odot$)[d]	JCMT Core Mass ($M_\odot$)[e]
HOPS 10	05:35:09	−05:58:26	388.2	8.19	46.2	0	3.33	1.33	0.90
HOPS 11	05:35:13	−05:57:57	388.3	7.18	48.8	0	9.0	1.09	1.34
HOPS 13	05:35:24	−05:55:33	388.7	6.00	383.6	Flat	1.15	0.27	0.50
HOPS 127	05:39:00	−07:20:22	394.5	4.68	133.3	I	0.39	0.27	0.26
HOPS 129	05:39:11	−07:10:34	393.8	3.40	191.3	Flat	1.67	0.57	0.42
HOPS 130	05:39:02	−07:12:52	393.2	3.46	156.7	I	1.48	0.18	0.26
HOPS 134	05:38:42	−07:12:43	391.2	6.05	781.9	Flat	7.77	0.32	0.19
HOPS 135	05:38:45	−07:10:56	391.1	4.65	130.3	I	1.14	0.24	0.47
HOPS 150A	05:38:07	−07:08:29	388.5	3.81	245.2	Flat	3.77	0.46	0.10
HOPS 150B[f]	05:38:07	−07:08:32	388.5	3.81	245.2	Flat	3.77	0.46	0.10
HOPS 157	05:37:56	−06:56:39	387.7	5.35	77.6	I	3.82	0.38	0.57
HOPS 164	05:37:00	−06:37:10	385.0	5.84	50.0	0	0.58	1.26	0.84
HOPS 166	05:36:25	−06:44:41	383.5	8.78	457.1	Flat	15.47	2.33	0.73
HOPS 169	05:36:36	−06:38:54	384.0	7.01	32.5	0	3.91	0.43	1.68
HOPS 177	05:35:50	−06:34:53	383.6	8.97	84.7	I	0.43	0.92	1.11
HOPS 185	05:36:36	−06:14:58	386.1	7.59	96.9	I	1.04	0.95	0.66
HOPS 191	05:36:17	−06:11:11	386.6	8.11	196.7	I	0.58	0.49	0.11
HOPS 194	05:35:52	−06:10:01	386.6	8.53	645.0	Flat	12.72	1.12	0.64
HOPS 198	05:35:22	−06:13:06	386.0	5.56	61.4	0	0.85	0.44	0.68
HOPS 200	05:35:33	−06:06:09	387.1	8.55	244.4	Flat	0.29	0.69	0.10
HOPS 355	05:37:17	−06:49:49	385.8	6.61	44.9	0	1.18	0.18	0.77
HOPS 408	05:39:30	−07:23:59	398.8	3.73	37.9	0	0.52	0.47	0.58

Notes.
[a] Distances are from Tobin et al. (2020), who use Gaia data of YSOs near each protostar to estimate their distances.
[b] We measured the system velocity by fitting a Gaussian to our $C^{18}O$ data. For details see Section 4.1.1.
[c] Results come from integration over the spectral energy distributions (SEDs) in Furlan et al. (2016).
[d] The ALMA core mass is measured from our Cycle 6 ALMA $C^{18}O$ data. The selected core size is 6500∼7500 au.
[e] The JCMT core mass is from JCMT 850 μm dust continuum data. The cores are identified by Lane et al. (2016) and have a typical core size of ∼6000 au.
[f] HOPS 150 was revealed to be a binary system, with a separation of ∼120 au, by Tobin et al. (2020, 2022). SED measurements of HOPS 150 by Furlan et al. (2016) were centered on HOPS 150A. However, the outflow cavity seen in HST IR images shown in Habel et al. (2021) is clearly centered on HOPS 150B, but contain the combined fluxes of both sources. The molecular outflow data for HOPS 150 discussed in this paper, likely arises from HOPS 150B instead of HOPS 150A.

4. Results

The outflows of our 21 HOPS sources are shown in Figure 2, where the red and blue colors represent the red- and blueshifted outflow lobes, respectively, traced by the ^{12}CO $J=2-1$. The green color represents the dense cores traced by $C^{18}O$ $J=2-1$. The source name and the bolometric temperature, an indicator of protostellar age (Myers & Ladd 1993; Chen et al. 1995), are also labeled for each source. The upper, middle, and bottom rows show Class 0, Class I, and flat-spectrum sources respectively. Most of the Class 0 and Class I sources show clear bipolar outflows, and flat-spectrum sources show complex and messy structures. HOPS 408 shows a very compact outflow possibly indicating its young age. The outflows from HOPS 157, HOPS 185, and HOPS 130 mostly show emission from blueshifted velocities. For HOPS 157 the peak of the $C^{18}O$ emission (shown in green) is coincident with the very compact redshifted lobe. The outflow from HOPS 185 is clearly bipolar, but we detect mostly blueshifted emission for both lobes. This could be due to the fact that for this system, the outflow axis is relatively close to the plane of the sky (see Section 4.1.4). Besides the unipolar outflows, asymmetrical features can be seen in many of the bipolar outflows in Figure 2. The outflow in HOPS 169 shows a clear "S-shape" indicating the source is precessing. The axis of the redshifted outflow lobe in HOPS 11 changes at the position where it appears to interact with the dense core traced by the $C^{18}O$. The lobes of the outflows from HOPS 355 and HOPS 164 appear to be misaligned. In addition, the outflow from HOPS 198 shows a clear difference in the width of its two lobes. In this section, we will derive the outflow properties for all the sources shown in Figure 2.

4.1. Determining Outflow Properties

Molecular outflow properties are key for assessing the impact protostars have on their surrounding medium. One of their most important properties is mass, as many of the other properties depend on it. This is calculated using the ^{12}CO line emission, which in most cases is optically thick. Hence, it is essential to correct the line opacity (which usually depends on the outflow velocity) to obtain an accurate mass estimate (as explained in Section 4.1.2) (Dunham et al. 2014; Bradshaw et al. 2015). Another issue in estimating the total outflow mass is that, in many cases, it is very difficult to separate the low-velocity outflow component from the cloud emission (Arce & Goodman 2001; Feddersen et al. 2020; Xu et al. 2022a). In general, the mass of the low-velocity component of a molecular outflow is significantly greater than the high-velocity outflow mass. Without including the low-velocity outflow component, the outflow mass can be severely underestimated by factors of about 2–10 (Offner et al. 2011; Dunham et al. 2014).

Table 2
Summary of ALMA Data Used in Analysis

Source	Line	Beam Size (″)	Beam Position Angle (deg)	Average rms in Field of View[a] (mJy beam^{-1})	rms in Central Region[b] (mJy beam^{-1})
HOPS 10	^{12}CO 2–1	1.″26 × 1.″00	82.1	9.7	6.8
	^{13}CO 2–1	1.″30 × 1.″04	81.9	13.0	9.2
	C^{18}O 2–1	1.″31 × 1.″04	83.7	10.1	7.1
HOPS 11	^{12}CO 2–1	1.″26 × 0.″99	79.3	4.0	7.2
	^{13}CO 2–1	1.″30 × 1.″04	80.7	13.0	9.1
	C^{18}O 2–1	1.″31 × 1.″04	82.4	10.2	7.1
HOPS 13	^{12}CO 2–1	1.″26 × 0.″99	79.9	12.3	7.4
	^{13}CO 2–1	1.″30 × 1.″04	80.7	13.0	9.3
	C^{18}O 2–1	1.″30 × 1.″04	82.4	10.2	7.0
HOPS 127	^{12}CO 2–1	1.″25 × 0.″98	−87.5	10.3	7.2
	^{13}CO 2–1	1.″29 × 1.″03	89.9	13.6	9.5
	C^{18}O 2–1	1.″30 × 1.″02	−88.9	11.8	9.4
HOPS 129	^{12}CO 2–1	1.″24 × 0.″98	−86.3	7.1	5.0
	^{13}CO 2–1	1.″29 × 1.″03	−89.6	13.5	9.4
	C^{18}O 2–1	1.″30 × 1.″02	−88.5	10.5	7.3
HOPS 130	^{12}CO 2–1	1.″25 × 0.″98	88.6	7.0	4.9
	^{13}CO 2–1	1.″29 × 1.″03	86.1	13.3	9.3
	C^{18}O 2–1	1.″30 × 1.″03	87.1	10.3	7.2
HOPS 134	^{12}CO 2–1	1.″26 × 0.″99	89.6	7.3	5.3
	^{13}CO 2–1	1.″30 × 1.″04	87.3	13.2	9.3
	C^{18}O 2–1	1.″31 × 1.″03	88.5	10.5	7.3
HOPS 135	^{12}CO 2–1	1.″26 × 0.″99	−89.7	7.1	5.0
	^{13}CO 2–1	1.″30 × 1.″03	88.2	13.6	9.4
	C^{18}O 2–1	1.″31 × 1.″03	89.5	13.6	11.8
HOPS 150	^{12}CO 2–1	1.″26 × 0.″99	−89.0	10.6	7.1
	^{13}CO 2–1	1.″29 × 1.″03	89.0	13.6	9.5
	C^{18}O 2–1	1.″30 × 1.″03	−89.7	10.6	7.4
HOPS 157	^{12}CO 2–1	1.″24 × 0.″98	84.7	6.9	4.9
	^{13}CO 2–1	1.″29 × 1.″03	84.6	13.5	9.7
	C^{18}O 2–1	1.″30 × 1.″03	86.0	10.6	7.5
HOPS 164	^{12}CO 2–1	1.″25 × 0.″98	84.2	9.5	7.4
	^{13}CO 2–1	1.″29 × 1.″03	84.4	14.4	12.1
	C^{18}O 2–1	1.″30 × 1.″03	85.8	10.3	7.3
HOPS 166	^{12}CO 2–1	1.″25 × 0.″98	86.3	9.2	6.5
	^{13}CO 2–1	1.″29 × 1.″03	85.3	13.5	9.6
	C^{18}O 2–1	1.″30 × 1.″03	86.7	10.4	7.0
HOPS 169	^{12}CO 2–1	1.″25 × 0.″99	88.5	9.9	7.1
	^{13}CO 2–1	1.″29 × 1.″03	85.9	13.2	9.3
	C^{18}O 2–1	1.″30 × 1.″03	87.1	4.1	2.9
HOPS 177	^{12}CO 2–1	1.″26 × 0.″99	83.6	6.8	4.8
	^{13}CO 2–1	1.″29 × 1.″03	84.1	13.0	9.1
	C^{18}O 2–1	1.″30 × 1.″03	85.3	10.2	7.2
HOPS 185	^{12}CO 2–1	1.″26 × 1.″00	82.1	6.7	4.8
	^{13}CO 2–1	1.″30 × 1.″04	82.3	13.1	9.1
	C^{18}O 2–1	1.″31 × 1.″04	83.9	10.1	7.2
HOPS 191	^{12}CO 2–1	1.″26 × 0.″99	79.5	6.8	4.8
	^{13}CO 2–1	1.″30 × 1.″04	80.9	13.1	9.2
	C^{18}O 2–1	1.″31 × 1.″04	82.6	10.2	7.1
HOPS 194	^{12}CO 2–1	1.″25 × 0.″99	83.9	10.1	7.1
	^{13}CO 2–1	1.″29 × 1.″03	84.3	13.1	9.3
	C^{18}O 2–1	1.″30 × 1.″03	85.5	10.2	7.1

Table 2
(Continued)

Source	Line	Beam Size (″)	Beam Position Angle (deg)	Average rms in Field of View[a] (mJy beam^{-1})	rms in Central Region[b] (mJy beam^{-1})
HOPS 198	^{12}CO 2–1	1.″26 × 0.″99	83.3	6.7	4.7
	^{13}CO 2–1	1.″30 × 1.″03	83.7	13.2	9.6
	C^{18}O 2–1	1.″31 × 1.″04	85.0	10.2	7.1
HOPS 200	^{12}CO 2–1	1.″26 × 0.″99	82.9	6.7	4.7
	^{13}CO 2–1	1.″30 × 1.″04	83.0	13.1	9.2
	C^{18}O 2–1	1.″31 × 1.″04	84.5	10.2	7.1
HOPS 355	^{12}CO 2–1	1.″26 × 0.″99	−89.8	7.0	4.9
	^{13}CO 2–1	1.″30 × 1.″03	88.0	13.6	9.7
	C^{18}O 2–1	1.″31 × 1.″03	89.2	10.4	7.3
HOPS 408	^{12}CO 2–1	1.″25 × 0.″98	−88.2	7.1	5.0
	^{13}CO 2–1	1.″29 × 1.″03	89.3	13.6	9.6
	C^{18}O 2–1	1.″30 × 1.″03	−89.5	10.6	7.4

Notes.
[a] Average rms noise out to a distance where the sensitivity is 40% that of the phase center (∼25.″0 from the center).
[b] Average rms noise out to a distance where the sensitivity is 80% that of the phase center (∼15.″0 from the center).

Sensitive ALMA observations can provide the means to obtain more accurate mass estimations than was previously possible (see, e.g., Zhang et al. 2016). Our ALMA observations clearly show low-velocity outflow structures in the low-opacity (or optically thin) ^{13}CO and C^{18}O(2–1) lines (see Figure 3), which trace the outflow down to velocities of 1 km s^{-1}, or less, from the system velocity. Emission from these rarer isotopologues also allows us to correct for optical depth effects (as explained in Section 4.1.2) needed to obtain accurate outflow mass estimates (e.g., Zhang et al. 2016).

Other important outflow properties, such as the momentum and kinetic energy, as well as the mass, momentum, and energy injection rates, depend on the outflow velocity. In order to obtain an accurate outflow velocity one needs to correct the observed velocity (which only probes the component of the velocity along the line of sight) by the inclination of the outflow axis with respect to the plane of the sky. Recent complementary ALMA observations allow us to obtain fairly accurate estimates of the inclination of the disk plane, which is expected to be perpendicular to the outflow (see Section 4.1.4).

In the subsections below we describe the procedure we use to obtain various outflow properties. In some cases, the methods are based on the techniques used by other recent studies (as is the case for the outflow mass and line opacity correction). In other cases, we introduce new methods, such as one way we use to derive the outflow mass ejection rate.

4.1.1. System Velocity

The envelope central velocity, also referred to as the system velocity ($v_{\rm syst}$), is needed to derive the outflow (radial) velocity, and hence the outflow momentum and energy. To obtain $v_{\rm syst}$ we use the central velocity determined from a Gaussian fit to the C^{18}O line averaged over an ∼18″ × 18″ region centered on the protostar. If there are multiple components in the C^{18}O average spectrum, then we only fit the component with the highest intensity. In order to corroborate our estimate of $v_{\rm syst}$, we create position–velocity diagrams perpendicular to the outflow direction for each source and check whether the envelope emission is centered at the system velocity, as expected from models of circumstellar envelopes with infall and rotation (e.g., Oya et al. 2022). Detailed position–velocity (PV) diagram modeling with an infall-rotation model will be presented in a future paper. The estimated system velocities for all sources are shown in Table 1. The outflow radial velocity ($v_{\rm out}$) is then the difference between the observed LSR velocity ($V_{\rm LSR}$) and the system velocity. That is, $v_{\rm out} = |V_{\rm LSR} - v_{\rm syst}|$.

4.1.2. ^{12}CO and ^{13}CO Opacity Correction

In Orion A, as in most other star-forming molecular clouds, the ^{12}CO(2–1) is optically thick (Kong et al. 2018). In our high-resolution ALMA data, we found that for many sources the ^{13}CO(2–1) is also optically thick near the system velocity. Thus, to obtain an accurate mass determination from the emission maps of these species, one needs to correct for the opacity of both the ^{12}CO and ^{13}CO(2–1) lines. Moreover, the opacity of these lines increases toward velocities closer to the system velocity (Dunham et al. 2014; Zhang et al. 2016). A proper opacity correction should take this into consideration.

We start by identifying the channels where there is clear outflow emission in the ^{12}CO maps, avoiding velocity channels near the system velocity as they are dominated by ambient cloud emission. We use these channels to produce integrated intensity maps that serve to delineate the boundaries of the redshifted and blueshifted outflow lobes. These outflow masks are created to help isolate the outflow emission from ambient gas. All outflow properties discussed here are measured within these outflow masks.

The optical depth correction factor is outlined by Dunham et al. (2014), who used ^{13}CO to correct for the opacity of the ^{12}CO line. An extension of this method, using C^{18}O to correct for the opacity of the ^{13}CO line, is described by Zhang et al. (2016). We followed their procedure, which we summarize below.

In general, the C^{18}O is thought to be optically thin (Kong et al. 2018). We also assume that the ^{12}CO, ^{13}CO, and C^{18}O emission associated with the molecular outflow are in local thermal equilibrium (LTE) with the same excitation temperature of about 50 K (Dunham et al. 2014). We assume that the

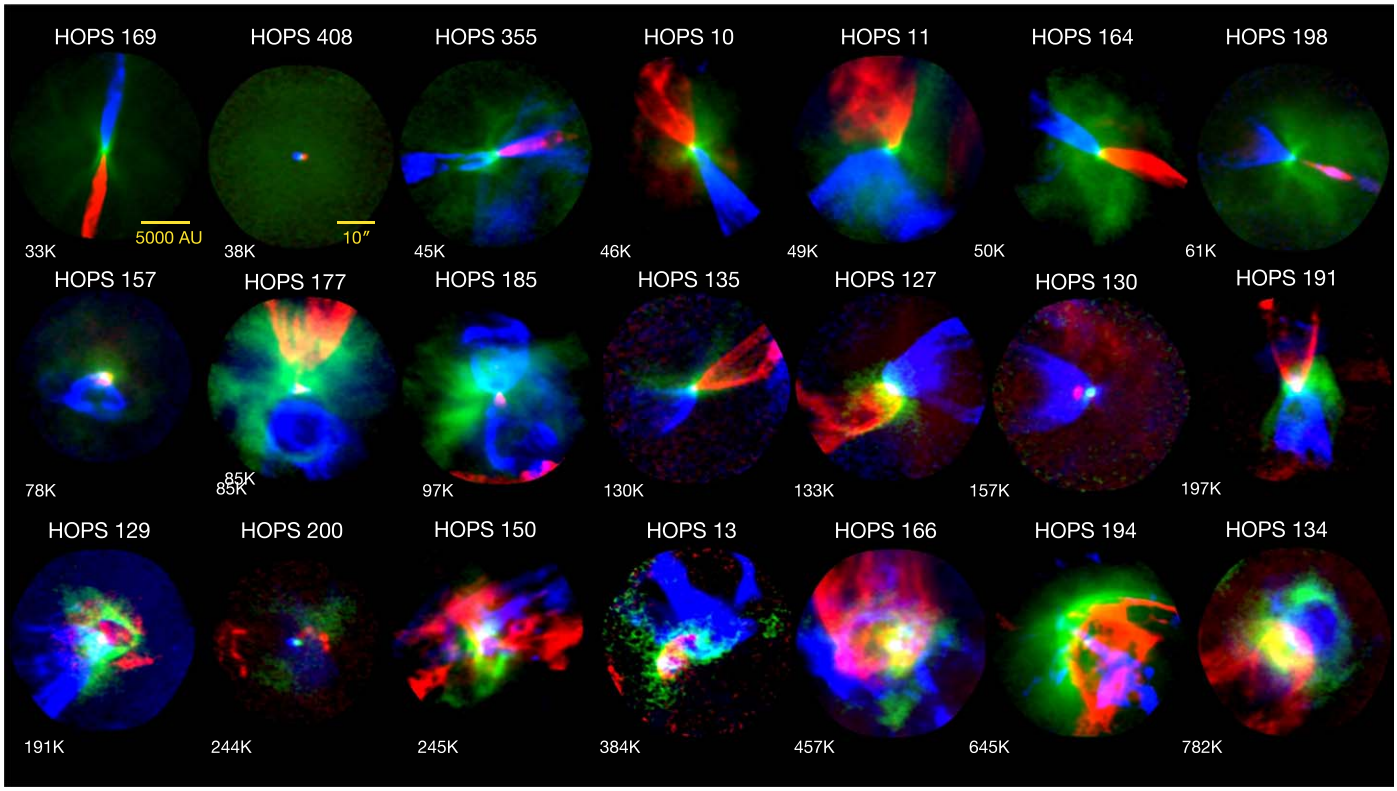

Figure 2. Protostellar outflows and envelopes in our survey, which include 21 sources at different evolutionary stages. ^{12}CO $J = 2-1$ integrated intensity maps trace the blueshifted (blue) and redshifted (red) molecular outflow lobes. C^{18}O $J = 2-1$ integrated intensity maps, shown in green, trace the dense circumstellar envelope. The upper, middle, and bottom rows show Class 0, Class I, and flat-spectrum protostars, respectively, and are arranged in order of increasing $T_{\rm bol}$ (which we use as a proxy for age) from left to right. Source names are shown above each map. Each map has a diameter of about 50.″4, which is set by the 40% primary beam power response (compared to the center of the map). The coordinates of the center of the panels are given in Table 1.

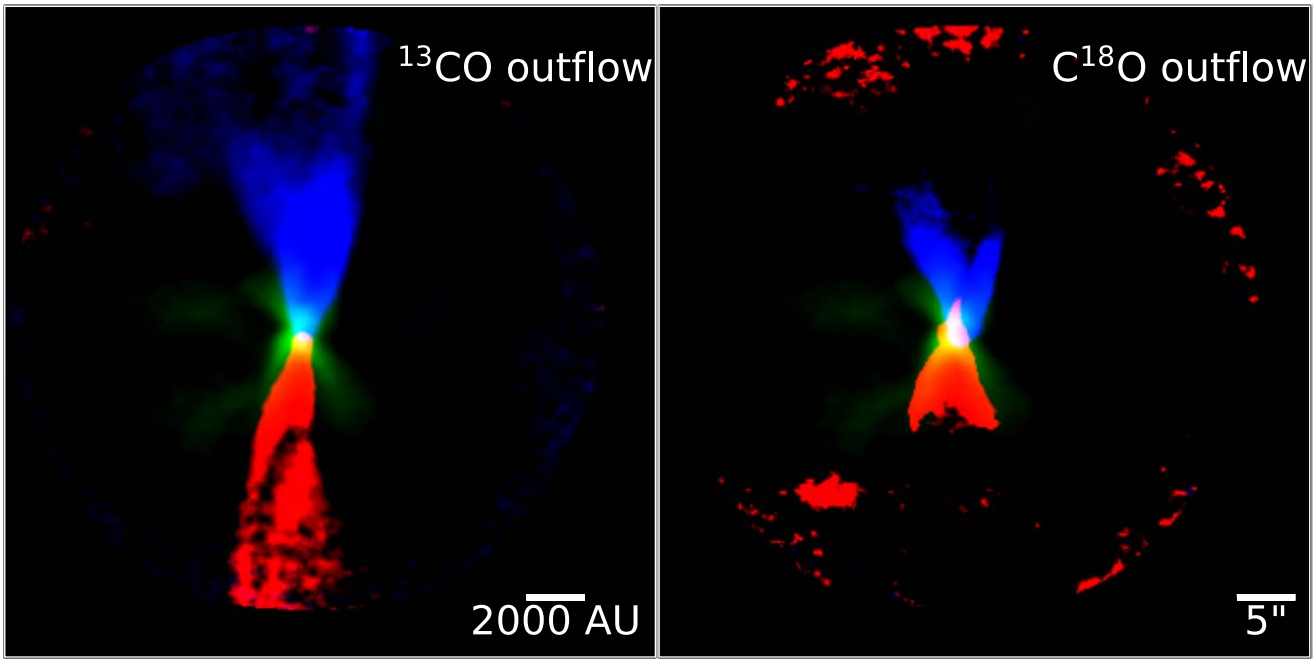

Figure 3. HOPS 169 outflow traced by ^{13}CO (left) and C^{18}O (right) centered at α (J2000) = $5^{\rm h}36^{\rm m}36.^{\rm s}1$, δ(J2000) = 06°38′54.″2). Left: ^{13}CO $J = 2-1$ integrated intensity maps are used to trace the blueshifted (blue) and redshifted (red) outflow lobes. Right: same outflow but traced by the C^{18}O $J = 2-1$ emission. In both plots, the C^{18}O $J = 2-1$ integrated intensity map (integrated over velocities close to the system velocity) traces the dense envelope, and it is shown in green.

^{12}CO, ^{13}CO, and C^{18}O emission from the outflow is emitted from the same volume and different isotopic species have the same excitation temperature. ^{12}CO can easily be thermalized even at densities $\leqslant$100 cm $^{-3}$ (Wilson et al. 2009). In the dense protostellar cores with a number density of the order of 10^6–10^8 cm^{-3}, rarer CO isotopes would also be thermalized. This is a

very good approximation especially for the lower J transitions because they have smaller Einstein A coefficients that lead to a slower depopulation rate. Thus, in our case, the assumption of LTE conditions is satisfactory.

The brightness temperature ratio for ^{13}CO and C^{18}O can be expressed as

$$\frac{T_{R,13}(\nu)}{T_{R,18}(\nu)} = \frac{1 - \exp(-\tau_{\nu,13})}{1 - \exp(-\tau_{\nu,18})} = \frac{1 - \exp(-\tau_{\nu,13})}{\tau_{\nu,18}}, \quad (1)$$

$$\approx X_{13,18} \frac{1 - \exp(-\tau_{\nu,13})}{\tau_{\nu,13}}, \quad (2)$$

where T_R is the brightness temperature and the subscripts 13 and 18 represent ^{13}CO and C^{18}O respectively. $X_{13,18}$ is the abundance ratio of ^{13}CO relative to C^{18}O, which we assume to be 8.7 (Wilson & Matteucci 1992). The correction factor CF$_{13}$ for the ^{13}CO opacity is

$$\mathrm{CF}_{13} = \frac{\tau_{\nu,13}}{1 - \exp(-\tau_{\nu,13})} \approx X_{13,18} \frac{T_{R,18}(\nu)}{T_{R,13}(\nu)}. \quad (3)$$

Then, the ^{12}CO correction is determined using the same equation, but using $X_{12,13} = 62$ (Langer & Penzias 1993) instead of $X_{13,18}$, and the brightness temperature of the ^{13}CO and ^{12}CO emission in place of $T_{R,18}$ and $T_{R,13}$, respectively. To obtain the brightness temperature ratio $T_{R,18}(\nu)/T_{R,13}(\nu)$ and $T_{R,13}(\nu)/T_{R,12}(\nu)$ we fit a second-order polynomial to the redshifted and blueshifted outflow lobe of each source independently. The ratio is calculated using the average brightness temperature for each channel inside the outflow of the mask. An example of the HOPS 169 redshifted outflow lobe (Figure 3) is shown in Figure 4. The correction factor estimated from the redshifted and blueshifted outflow lobes is then used to correct for the opacity of the entire position–position–velocity (PPV) cube. We first correct for the ^{13}CO opacity using the ^{13}CO to C^{18}O ratio. Then the ratio of the ^{12}CO to the corrected ^{13}CO emission was used to correct the optically thick ^{12}CO emission.

4.1.3. Outflow Mass, Momentum, and Energy Estimation

We follow Dunham et al. (2014) to derive most of the molecular outflow properties using the ^{12}CO, ^{13}CO, and C^{18}O data. The molecular hydrogen (H$_2$) column density of the outflowing material can be calculated from the ^{12}CO emission, using

$$N_{\mathrm{H_2}} = f(J, T, X_{\mathrm{CO}})I, \quad (4)$$

$$f(J, T, X_{\mathrm{CO}}) = X_{\mathrm{CO}} \frac{3k}{8\pi^3 \nu \mu^2} \frac{(2J+1)}{(J+1)} \frac{Q(T)}{g_J} e^{\frac{E_{J+1}}{kT}}, \quad (5)$$

where I is the (opacity corrected) integrated intensity in K km s^{-1}, and J is the quantum number for total rotational angular momentum. One can replace the frequency (ν), magnetic dipole moment (μ), partition function (Q), upper-level energy (E_{J+1}), the energy statistical weight (g), and abundance ratio relative to hydrogen X with the values for ^{13}CO and C^{18}O, to obtain estimates of the H$_2$ column density using the other two CO isotopologues. We assumed abundance ratios of 10^{-4}, 1.6×10^{-6}, and 1.7×10^{-7} for CO, ^{13}CO, and C^{18}O, respectively, which are consistent with the isotopologue ratios discussed in Section 4.1.2 (Frerking et al. 1982; Langer & Penzias 1993; Hsieh et al. 2019).

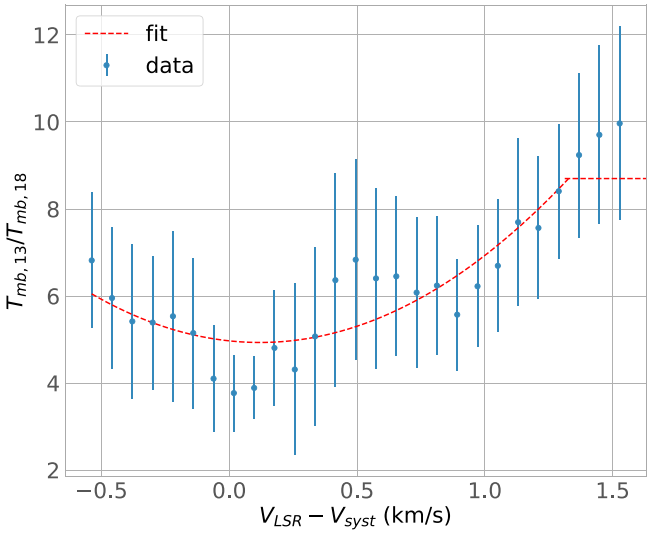

Figure 4. Average ^{13}CO(2–1)/C^{18}O(2–1) brightness temperature ratio in the redshifted outflow lobe of HOPS 169. The ratio is calculated for every velocity channel using data above 3σ within the outflow mask region. The blue points represent the data and the red line denotes the best-fit second-degree polynomial. The polynomial is truncated at the isotopic ratio of 8.7. The error bars represent the dispersion around the mean of the brightness temperature ratio across the redshifted outflow lobe.

For each channel, we computed the outflow mass using

$$M = \mu_{\mathrm{H_2}} m_{\mathrm{H}} A_{\mathrm{pixel}} N_{\mathrm{H_2}},$$

where $\mu_{\mathrm{H_2}} = 2.8$ is the mean molecular weight of H$_2$ (Kauffmann et al. 2008), m_{H} is the hydrogen atom mass, and $A_{\mathrm{pixel}} = 6.47 \times 10^{24} \times d^2$ cm^2 is the pixel area at a distance of d in parsec. We use the distance estimate derived by Tobin et al. (2020), who used Gaia data of young stars in the Orion molecular cloud to estimate the distance to each protostar (which we include in Table 1).

We computed the mass for every pixel in every velocity channel, hereafter the mass spectrum, within the outflow mask using ^{12}CO, ^{13}CO, and C^{18}O. We go through the channel maps of each tracer (starting at the highest outflow velocities) and use the ^{12}CO to derive the outflow mass for the high-velocity emission. For lower velocity outflow emission, the ^{12}CO becomes extremely optically thick and contaminated with the ambient gas emission, so we then use the ^{13}CO outflow emission to estimate the mass at lower velocities. For sources in which there is clear outflow emission traced by C^{18}O (see, e.g., Figure 3), we use it to estimate the mass of the lowest outflow velocity components, near the system velocity. For all sources, the emission at velocities close to v_{syst} becomes dominated by the large-scale core (ambient) emission. The velocity at which the emission is dominated by core emission, rather than by outflow emission, is different for each source and isotopologue. Thus, we used different velocity ranges for each source, lobe, and tracer in order to try to capture as much of the outflow emission as possible. We select the velocity range for each tracer such that the protostellar outflow shows a clear intensity contrast with the ambient emission, and avoid channels where the structure is dominated by the cloud emission. The velocity range used for each tracer and source is shown in Appendix C. An example mass spectrum for HOPS 135 using all three

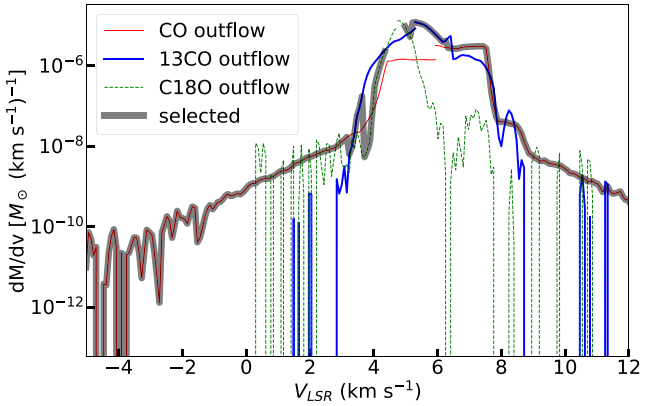

Figure 5. Molecular outflow mass spectrum for the outflow from HOPS 135, estimated using ^{12}CO, ^{13}CO, and C^{18}O. The black line marks the final selected mass spectrum used for estimating the outflow mass.

isotopologues is shown in Figure 5, where the final mass spectrum is highlighted in black. Note that to avoid contamination from large-scale cloud emission at outflow velocities we performed a cloud subtraction procedure, described in Appendix A. All sources were used for each analysis unless otherwise specified (see Table 8 for excluded sources).

4.1.4. Inclination Correction

The inclination correction plays a very important role in determining the correct value of the outflow momentum and energy, as well as the outflow mass, momentum, and energy ejection rates. On average inclination can affect the outflow mass ejection rate by a factor of 3–5, and without the correction any possible evolution trend could be rendered undetectable in the data. In this paper, we define i to be the inclination angle of the outflow axis with respect to the line of sight. That is, an outflow with $i = 0°$ has a *pole-on* orientation and one with $i = 90°$ is said to be *edge-on*.

We used the deconvolved disk major and minor axes around each of the protostars in our sample, measured by Tobin et al. (2020) from their ALMA 0.87 mm data, to derive the disk inclination angle. Assuming the disk is thin, flat, and circular, we derive the inclination angle for each disk using the ratio of the observed major-to-minor axes. We then assume the outflow axis is perpendicular to the disk, to estimate the outflow's inclination angle with respect to the line-of-sight sky (these are listed in Table 5). This method works well when the disk continuum emission is well resolved, yet free of extended envelope emission. This works reasonably well for all sources except for HOPS 177, for which the inclination angle derived using this method ($i = 81°$) is highly uncertain, as the continuum emission is basically the size of the beam (i.e., the emission appears unresolved) and the flux density S/N of this source is only about 3.7 (Tobin et al. 2020). Moreover, the CO velocity structure for HOPS 177 is not consistent with that expected of a wide-angle outflow with an approximately edge-on orientation.[15] Hence, for this source we adopt $i = 57°.3$ (the mean inclination angle from a random uniform distribution of outflow orientations on the sky, Bontemps et al. 1996).

[15] For an edge-on wide-angle outflow one would expect to see both red and blueshifted emission in both lobes.

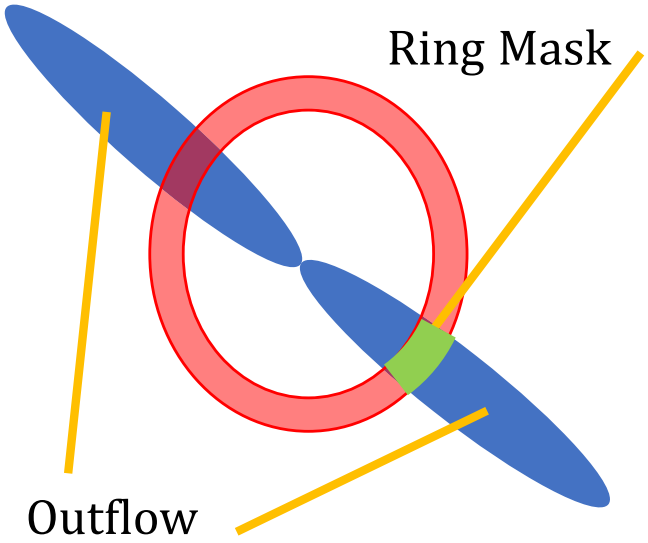

Figure 6. Cartoon diagram of the ring mask used in the RM for determining the molecular outflow mass, momentum, and energy rates.

We also estimated the inclination angle by fitting a wide-angle wind entrainment model to the ^{12}CO data. This method has been used in the past (Li & Shu 1996; Lee et al. 2000) and we wanted to assess how well it compared to the method using the disk continuum observations described above. A description of the fitting procedure and a more detailed comparison of the inclination angle estimates obtained using the two different methods are included in Appendix B.

4.1.5. Outflow Mass, Momentum, and Energy Ejection Rate Estimation

Currently, the most common way to measure the molecular mass outflow mass rate, the outflow momentum injection rate (also referred to as the outflow force, $F_{\rm out}$), or the outflow energy injection rate (also referred to as the outflow mechanical luminosity, $L_{\rm out}$) is by dividing the outflow quantity of interest by a *dynamical time* ($t_{\rm dyn}$). This $t_{\rm dyn}$ is simply obtained by dividing the outflow lobe length ($R_{\rm lobe}$) by a *characteristic* outflow velocity, which typically is chosen to be the maximum (detectable) molecular outflow velocity (e.g., van der Marel et al. 2013; Dunham et al. 2014).

However, this simple method is heavily dependent on observational parameters (see Section 5.1) and inaccurately assumes that all the gas in the molecular outflow is moving at a uniform (constant) velocity from the source position to the current position. One problem with this assumption is that the gas in a molecular outflow is mostly made of material that has been entrained by the underlying protostellar wind rather than material that was launched by the protostar-disk system (Offner & Chaban 2017; Rohde et al. 2022).

For estimating the outflow momentum injection rate, we developed a procedure based on the *annulus method* described in Bontemps et al. (1996), which here we call the ring method (RM). For this, we first created a series of *ring masks* with thickness (ΔR) around the protostars in our sample, at different distances (R) from the positions of the outflow sources. We computed the outflow mass, momentum, and energy as a function of velocity within the ring mask (see Figure 6). Then, to estimate the rate, we calculated the *crossing time* across the ring mask for each channel, which is

obtained by dividing ΔR by the outflow velocity, where both are corrected for the inclination of the system, i.e., $v_{\rm out,cor} = |(v_{\rm chan} - v_{\rm syst})/\cos(i)|$; $\Delta R_{\rm cor} = \Delta R/\sin(i)$. Then we sum up the rate estimate for each velocity channel.

Our RM does not use a constant area as in the procedure used by Bontemps et al. (1996). In their method, the momentum flux is obtained following this equation:

$$F_{\rm obs} \propto \int_{\rm wings} \frac{T_{\rm A}^{*}(v_{\rm rad})\, dv_{\rm rad}\, {\rm Area}(r,\, \Delta r)\, v_{\rm rad}}{\Delta r / v_{\rm rad}}, \quad (6)$$

where the annulus has a radius of r and width of Δr, $v_{\rm rad}$ is the radial velocity, and Area is simply $r\Delta r\Delta\theta$, where $\Delta\theta$ is the angular extent of the annulus sector. Bontemps et al. (1996) assume the outflow fills the entire annulus for every velocity channel, and $\Delta\theta$ is the telescope beam FWHM. This is usually a good assumption for CO maps made with single-dish telescopes where the outflow is not resolved. The above equation also assumes the ^{12}CO is optically thin. Although Bontemps et al. (1996) applied a correction factor to correct for the optical depth of the ^{12}CO line, their correction is the same for all sources and does not depend on outflow velocity. In our study, we use multiple CO isotopes to construct the mass spectrum to avoid saturation and to trace the outflow mass at different velocities (see Figure 5). Within the ring, the area of the outflow changes as a function of velocity. In our RM, we account for this effect, and the momentum flux can be expressed as

$$F_{\rm obs} = \int \frac{{\rm mass}(v_{\rm chan})\, v_{\rm out,corr}}{\Delta R_{\rm cor}/v_{\rm out,corr}} dv_{\rm chan}, \quad (7)$$

where outflow mass is computed for each velocity channel within the intersection region between the ring and the outflow mask (see Figure 6, green region). That is, the outflow width can be different for different outflow velocities.

This method has several advantages over previous simple methods. The main one is that it does not assume the molecular outflow moves at a uniform velocity from the launched position to the current position. In addition, the outflow rate is calculated for each velocity channel independently, rather than using one velocity for all outflow emission. Moreover, it is not dependent on the field of view (which will bias the assumed outflow length) or the assumed $v_{\rm max}$, which will depend on the sensitivity of the observations. Thus this method provides a systematic way to obtain molecular outflow mass, momentum, and energy rates (hereafter referred to as *molecular outflow rates*) with better accuracy compared to previous estimates. We can also construct the ring mask at different distances from the protostar to obtain a radial profile. An example of the molecular outflow mass rate per lobe profile for HOPS 10 is shown in Figure 7.

Among our sample, several Class 0 sources have high-velocity collimated jet components traced only by CO that are clearly different from the rest of the molecular outflow emission of each source. These are HOPS 10, HOPS 11, and HOPS 164. Unlike the low-velocity outflow component, these molecular jets could be mostly made of disk-launched material (Lee 2020). To compare the entrained material with the disk-launched material, we separate out the extremely high-velocity components, which can clearly be seen in the mass rate spectrum of a source, as shown in Figure 8. The outflow mass rate spectrum is the outflow mass spectrum (Figure 5) divided by the crossing time across the ring $({\rm mass}(v_{\rm out,cor})/(\Delta R/v_{\rm out,cor}))$.

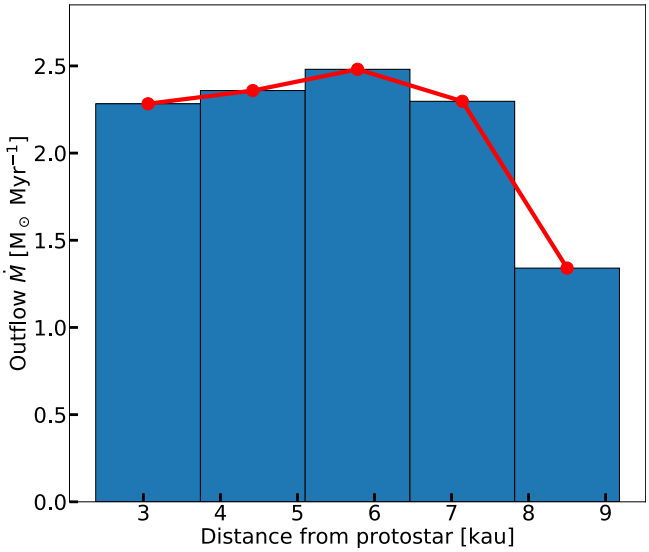

Figure 7. Molecular outflow mass rate (per lobe) for the Class 0 source HOPS 10. The profile is corrected for inclination angle.

We stress that the outflow mass rate we measure with our data is that of the entrained gas, and not of the mass that is directly ejected from the central disk-star system. Measuring the outflow mass rate for the entrained gas is crucial as it is directly linked to envelope dispersal.

To study the evolution of the molecular outflow rates we averaged all sources within each class in our sample (see Figure 9). We did not include HOPS 408 in the average for Class 0 sources, as the outflow from this source is barely resolved and the outflow rate cannot be measured using the ring mask method. HOPS 166 and HOPS 194 are not included in the average because they have significantly higher bolometric luminosity ($>10\,L_{\odot}$) and significantly higher core mass as compared to other sources in this study. In Figure 9 we plot the average molecular outflow rates per lobe for each evolutionary class. The derived values of these rates, at five different distances from each source, are listed in Appendix E (see Tables 9–11), for all sources in our sample.

From Figure 9, it is clear that Class I protostars have the highest total molecular outflow mass rate. This is opposite to the recent simulations showing the decrease in outflow mass-loss rate from Class 0 to Class I protostars (Rohde et al. 2022). The molecular outflow mass rate per lobe of Class I protostars is around 60% higher than that of Class 0 protostars and 6 times higher than flat-spectrum sources. The sharp decrease in mass outflow rate between Class I and flat-spectrum sources indicates that the majority of the mass entrainment occurs during the Class I phase.

In Figure 9, we plot the average molecular outflow rates (per outflow lobe) with and without the high-velocity jets, for the Class 0 sources. The molecular outflow mass rate profile does not change much when the high-velocity jets are added. This indicates the high-velocity jets in Class 0 do not carry much mass compared to the wider low-velocity swept-up material, and that the majority of the entrained mass lies within the low-velocity molecular outflow. However, the momentum and energy ejection rate increase by a factor of 2 and 4, respectively, for Class 0 sources, when high-velocity jets are included. Thus, the momentum in the low-velocity outflow is comparable to the high-velocity jets in Class 0, and the dominant energy ejection rate lies in the collimated high-velocity jets.

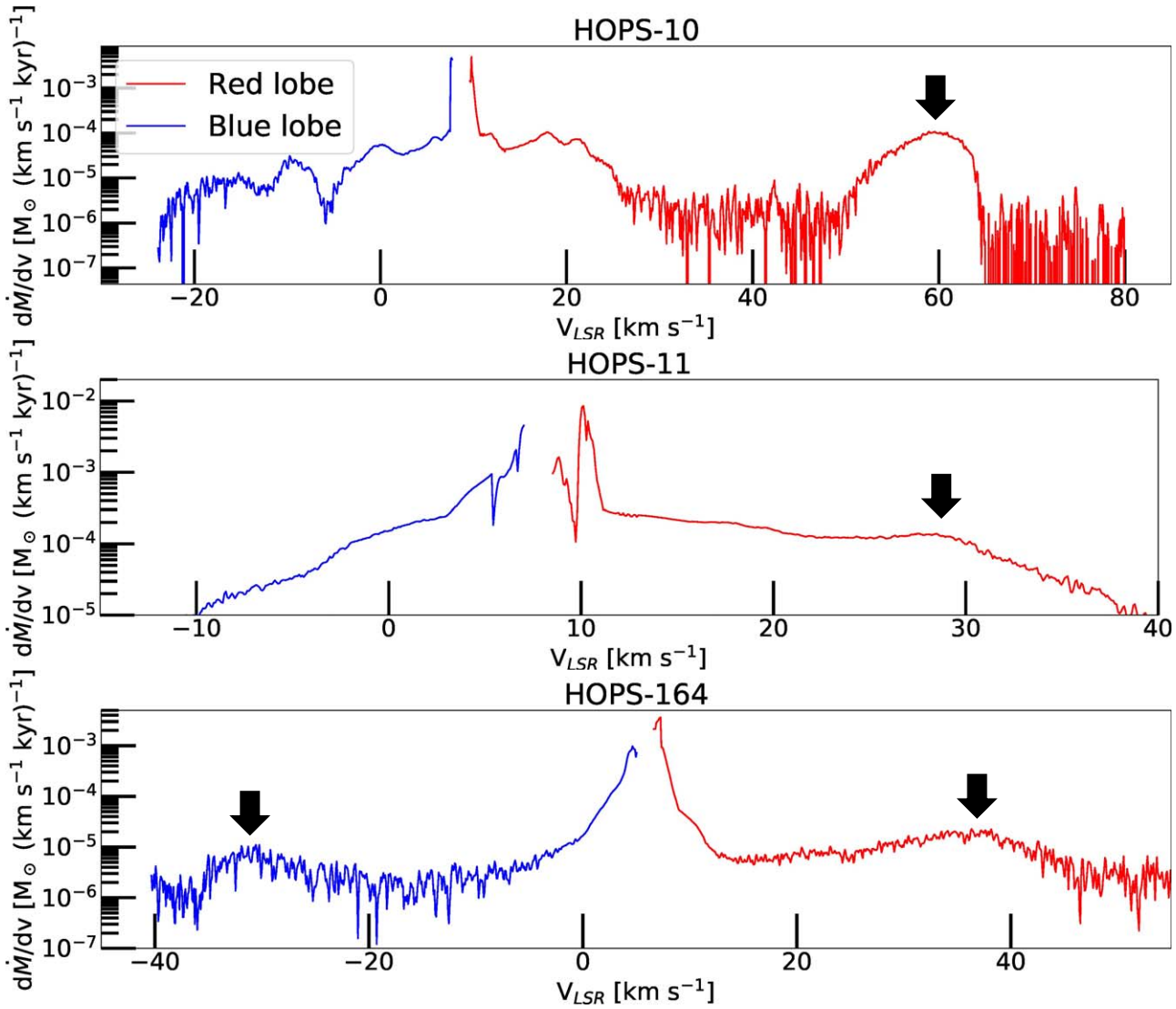

Figure 8. Example of molecular outflow mass rate spectrum for HOPS 10, HOPS 11, and HOPS 164 using the RM (see Figure 6). The mass ejection rate spectrum is the mass spectrum divided by the crossing time across the ring (mass($v_{\rm rad}$)/($\Delta r/v_{\rm rad}$)). The black arrows mark the positions of high-velocity jets.

We average all the distance bins in Figure 9, and multiply by 2 for two outflow lobes to obtain the average outflow rate for each protostellar stage. Using our estimate of the average molecular outflow mass rate during each protostellar stage, and assuming that the Class 0 phase lasts about 0.13–0.26 Myr, the Class I phase lasts approximately 0.27–0.52 Myr, and the flat-spectrum phase also lasts around 0.27–0.52 Myr (Dunham et al. 2015), we can estimate the total mass of the circumstellar material entrained by a *typical* outflow during each phase. We find that on average a protostar will entrain around 0.5–0.9 $M_\odot$ of circumstellar material during the Class 0 phase (using an average molecular outflow mass rate for this evolutionary phase of $\overline{\dot{M}}_{\rm out} = 3.5\ M_\odot$ Myr^{-1}), 1.5–2.9 $M_\odot$ of material during Class I phase (using $\overline{\dot{M}}_{\rm out} = 5.6\ M_\odot$ Myr^{-1}), and 0.2–0.4 $M_\odot$ during the flat-spectrum phase (using $\overline{\dot{M}}_{\rm out} = 0.8\ M_\odot$ Myr^{-1}). Thus, we expect that by the end of the protostellar phase, a typical outflow will entrain about 2.2–4.2 $M_\odot$ of circumstellar material (see Table 4).

Nearly all of the momentum and energy injected by the outflow to the core is concentrated during the Class 0 phase. Adopting the same timescales for each protostellar stage as above (and including the momentum and energy injection rates from the high-velocity jet component in the calculations), we expect outflows to inject a total of about 5.3–10.5 $M_\odot$ km s^{-1} of momentum and 3.5–7.0 $\times 10^{45}$ erg of energy in the Class 0 phase (using average momentum and energy injection rates for this evolutionary phase of $\overline{\dot{P}}_{\rm out} = 40.5\ M_\odot$ Myr^{-1} km s^{-1}, and $\overline{\dot{E}}_{\rm out} = 2.7 \times 10^{46}$ erg Myr^{-1}); approximately 5.1–9.9 $M_\odot$ km s^{-1} of momentum and 2.7–5.2 $\times 10^{44}$ erg of energy in the Class I phase (using, $\overline{\dot{P}}_{\rm out} = 19.06\ M_\odot$ Myr^{-1} km s^{-1}, and $\overline{\dot{E}}_{\rm out} = 9.9 \times 10^{44}$ erg Myr^{-1}); and about 0.6–1.2 $M_\odot$ km s^{-1} of momentum and 3.3–6.3 $\times 10^{43}$ erg of energy in the flat-spectrum phase (using $\overline{\dot{P}}_{\rm out} = 2.3\ M_\odot$ Myr^{-1} km s^{-1}, and $\overline{\dot{E}}_{\rm out} = 1.2 \times 10^{44}$ erg Myr^{-1}). We thus estimate that by the end of the protostellar phase, the total outflow momentum and energy will be approximately 11.0–21.6 $M_\odot$ km s^{-1} and 3.8–7.6 $\times 10^{45}$ erg, respectively. The results are summarized in Table 3.

4.2. PFT Technique and Observational Instantaneous Outflow Mass, Momentum, and Energy Ejection Rate Maps

Motivated by the RM (described above), we developed another procedure to estimate outflow mass rates, which we

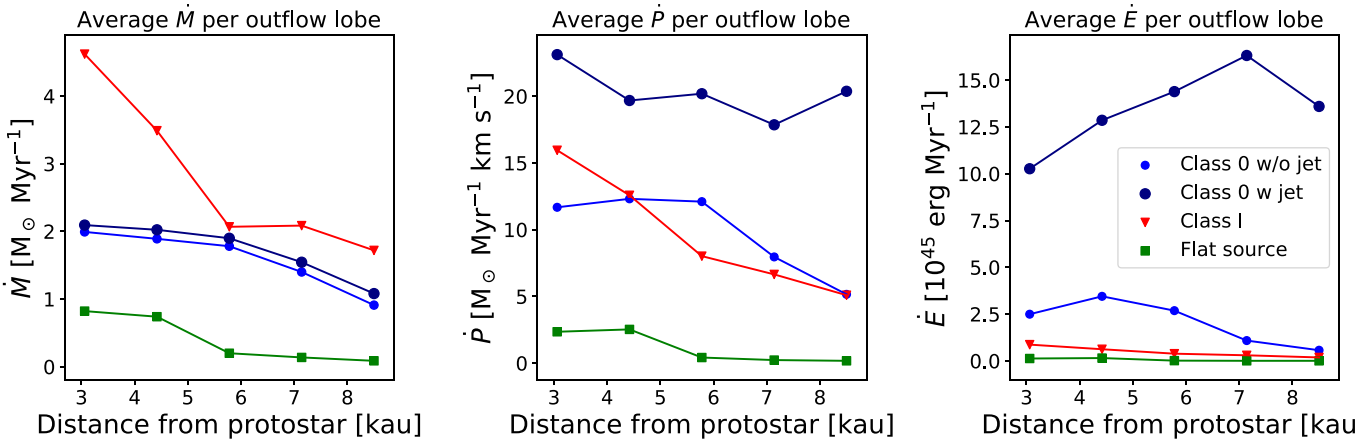

Figure 9. Profiles of the average molecular outflow mass, momentum, and energy rates per outflow lobe for different protostellar evolutionary classes (Class 0, Class I, and flat spectrum). For the Class 0 sources, we show the average rates with and without inclusion of the high-velocity jet component. All results shown are inclination corrected. In creating these plots, the Class 0 source HOPS 408 was not included because its outflow is barely resolved, and the flat-spectrum sources HOPS 166 and HOPS 194 were not included because they have significantly higher bolometric luminosity (>10 $L_\odot$) and significantly higher core masses compared to other sources in this study. The dispersion of outflow rate values for each evolutionary class is approximately a factor of 2.

Table 3
The Total Mass, Momentum, Energy Injected/displaced by the Molecular Outflow, and Corresponding Molecular Outflow Rates at Different Evolutionary Stages

Class	Duration (Myr)	$\overline{\dot{M}}_{\rm out}$ ($M_\odot$ Myr^{-1})	$\overline{\dot{P}}_{\rm out}$ ($M_\odot$ km s^{-1} Myr^{-1})	$\overline{\dot{E}}_{\rm out}$ (erg Myr^{-1})	$M_{\rm out}$ ($M_\odot$)	$P_{\rm out}$ ($M_\odot$ km s^{-1})	$E_{\rm out}$ (erg)	Core Mass[a] ($M_\odot$)
0[b]	0.13–0.26	3.5	40.5	2.7×10^{46}	0.5–0.9	5.3–10.5	$(3.5–7.0) \times 10^{45}$	(0.95, 1.04)
I	0.27–0.52	5.6	19.1	9.9×10^{44}	1.5–2.9	5.1–9.9	$(2.7–5.2) \times 10^{44}$	(0.49, 0.49)
Flat[c]	0.27–0.52	0.8	2.3	1.2×10^{44}	0.2–0.4	0.6–1.2	$(3.3–6.3) \times 10^{43}$	(0.46, 0.26)

Notes.
[a] The first value is the average core mass from our ALMA $C^{18}O$ data. The second value is the average core mass derived from the JCMT 850 μm dust continuum data (Lane et al. 2016). Both core mass estimates are measured using a similar core size of ~6000 au.
[b] HOPS 408 is excluded from these estimates as we were not able to obtain a reliable molecular outflow mass rate for this source.
[c] HOPS 194 and HOPS 166 are excluded from the average as these two sources have significantly higher core masses derived from $C^{18}O$ as compared to core masses derived from the dust continuum. They also have the highest bolometric luminosity (>10 $L_\odot$) in our sample.

call the PFT technique.[16] The basic idea of the PFT technique is to view each pixel as a thin ring and estimate the instantaneous outflow mass rate across each pixel. This is similar to the flux tracing commonly used in simulations (e.g., Mignone et al. 2012; Bryan et al. 2014). We start with calculating the mass, momentum, or energy spectrum for each pixel. Then, we compute the crossing time ($\tau_{\rm cross_{pix}}$) for each velocity channel, as in the RM, but we use the pixel width (ΔR_p) instead of the ring width. That is,

$$\tau_{\rm cross_{pix,vchan}} = \frac{\Delta R_p/\sin(i)}{|(v_{\rm chan} - v_{\rm syst})/\cos(i)|}, \quad (8)$$

where i is the inclination angle, and $(v_{\rm chan} - v_{\rm syst})/\cos(i)$ is the outflow velocity for that particular velocity channel, corrected for inclination ($v_{\rm out,corr}$). Then the outflow mass, momentum, and energy flux for a pixel located at position (x, y) can be computed as

$$F_{\rm obs}(x, y) = k \int \frac{{\rm mass}(v_{\rm chan}, x, y) v^n_{\rm out,corr}}{\tau_{\rm cross_{pix,vchan}}} dv_{\rm chan}, \quad (9)$$

where $n = 0$, 1, 2, and $k = 1.0$, 1.0, 0.5 for mass, momentum, and energy flux, respectively. To avoid cloud contamination, we developed a cloud subtraction method for the PFT technique (different from that used for the RM), which we show in Appendix A.

In Figure 10, we present the outflow instantaneous mass, momentum, and energy ejection rate maps for HOPS 355. For other sources, the maps are shown in Appendix F. It is important to point out that instead of a single rate value, as obtained by previous methods (e.g., van der Marel et al. 2013), the 2D maps from the PFT technique contain spatial information on how the rates vary within the outflow cavity. The pixel scale is 66 au (0.″17). Each map carries a different physical meaning. The instantaneous molecular outflow mass rate maps track the material entrained by the outflow. The instantaneous momentum rate maps show the force acting on the gas in each pixel. The instantaneous energy ejection rate maps, which highly weigh the high-velocity components, show the distribution of the molecular outflow mechanical luminosity and typically reveal the collimated high-velocity components which are closely linked to the accretion-driven jet launched by the protostar. We will use the instantaneous energy ejection rate maps to identify protostellar jets and explore the relationship between jet mass-loss rate and accretion rate in a future paper.

[16] The code is available on GitHub at https://github.com/chenghanhsieh/pixel-flux-tracing-technique/blob/main/README.md.

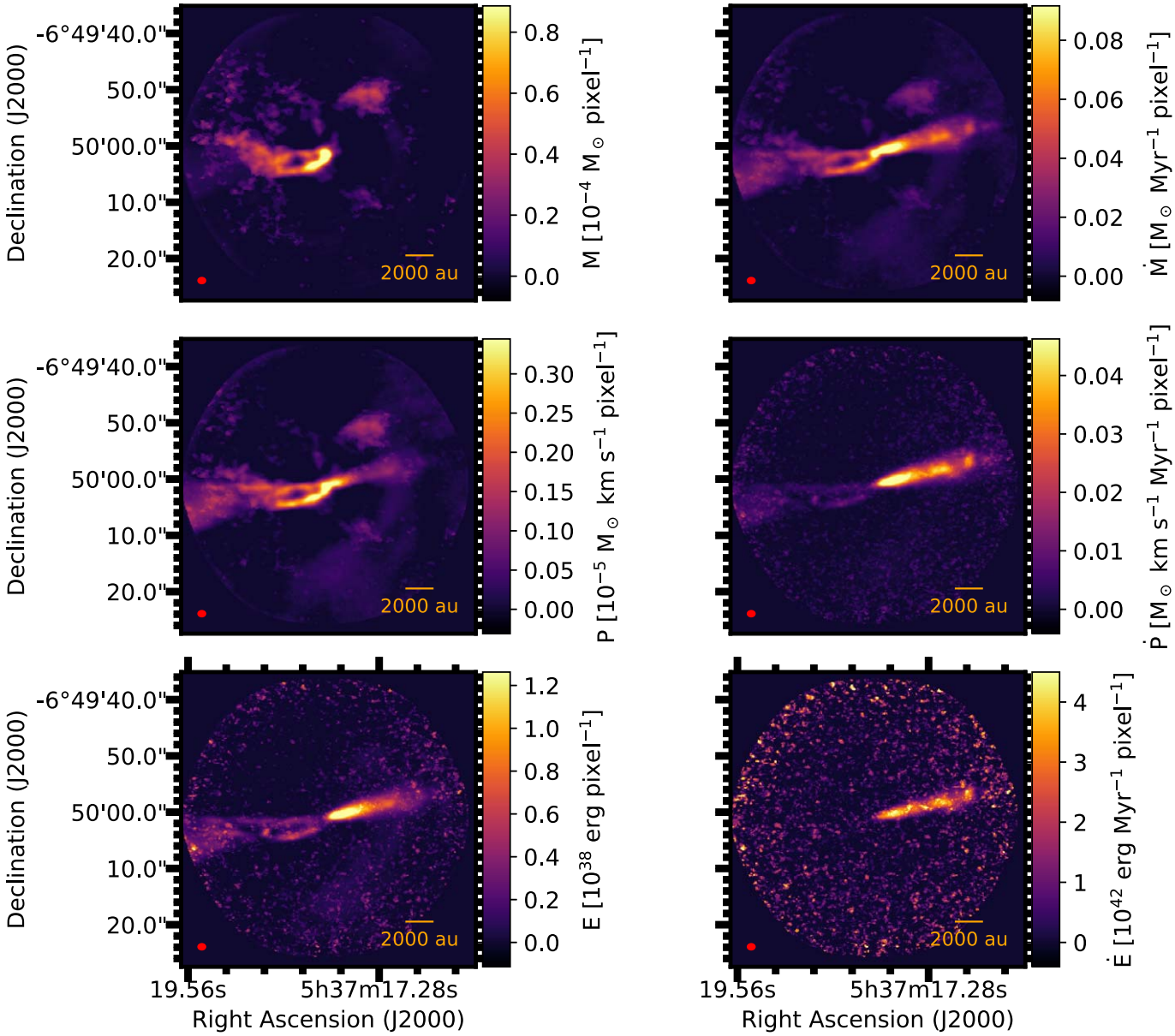

Figure 10. HOPS 355 molecular outflow mass, momentum, and energy maps (panels in the left column), and the corresponding rate maps (panels in the right column). The red ellipse in the bottom left of each panel represents the synthesized beam. Note that the pixel size is the same for all maps and is $0\farcs17 \times 0\farcs17$.

4.3. Outflow Opening Angles

To assess the importance of outflows in the removal of dense gas around the protostar, one important quantity to consider is the outflow opening angle, as it can be used to estimate the volume of gas cleared in a protostellar core by the outflow. To derive the outflow opening angle we follow a method based on that described by Offner et al. (2011), Feddersen et al. (2020), and M. Dunham et al. 2023, in preparation. We first construct an outflow mask based on the ^{12}CO integrated intensity maps with emission above 3σ, where we exclude velocity channels with cloud emission. We calculate the position angle for each pixel and then obtain the distribution of pixels at different angles within the outflow mask. We then fit this with a Gaussian to obtain the mean of the distribution (μ), from which we obtain the outflow axis position angle, and the dispersion (σ). The outflow opening angle is then defined as the full-width quarter maximum (FWQM) ($\Theta_{\rm FWQM} = 3.3302\sigma$) of the distribution. This definition is selected to match the opening angle derived by eye and to be consistent with past studies (e.g., Offner et al. 2011; M. Dunham et al. 2023, in preparation). The opening angles measured by this method are the projected outflow opening angles in the plane of the sky and an inclination correction is needed. Without correction, the outflow opening angle for systems that are close to pole-on (i.e., small values of i) would be overestimated. We adopted a simple conical outflow model to correct the opening angles for the systems' inclination, as described by M. Dunham et al. (2023, in preparation).

We were not able to obtain reliable estimates of the opening angle using this technique for the Class 0 HOPS 408, as its outflow is barely resolved by our observations, and the flat-spectrum sources HOPS 150 and HOPS 166, as their outflows are very clumpy or spotty, which resulted in very poor Gaussian fits to the pixel angle distribution. For HOPS 194, the Gaussian fits to the ^{12}CO pixel angle distribution is very poor,

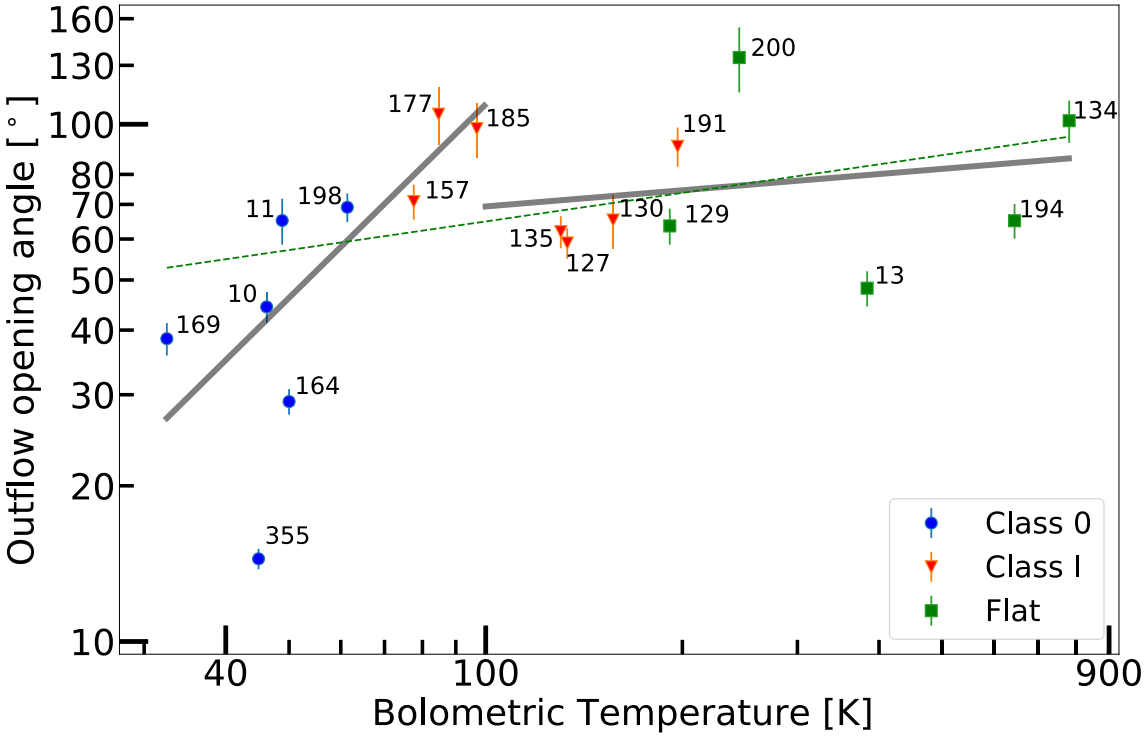

Figure 11. Outflow opening angle vs. bolometric temperature for the sources in our sample. The opening angle for two flat sources (HOPS 150 and HOPS 166) and one Class 0 source (HOPS 408) are not included in the plot as their opening angles are ill-defined (see the text for details). For HOPS 194, the Gaussian fits to the ^{12}CO pixel angle distribution is very poor, so we measured the outflow opening angle by eye using the C^{18}O integrated intensity map. The thin-dashed green line represents a power-law fit of all the data described by equation $y = 10^c x^m$, with $m = 0.18 \pm 0.10$ and $c = 1.45 \pm 0.22$. The two thick gray lines represent the broken power-law fits with a break at $T_{\rm bol} = 100$ K. For $T_{\rm bol} \leqslant 100$ K, $m = 1.24 \pm 0.30$, and $c = -0.45 \pm 0.57$; $T_{\rm bol} > 100$ K, $m = 0.10 \pm 0.19$, and $c = 1.63 \pm 0.47$. Outflow opening angles have been corrected for the outflows' inclination.

but the outflow cavity can clearly be traced by C^{18}O as shown in Figure 2. Thus, for this source, we measured the outflow opening angle by eye using its C^{18}O moment 0 map.

Figure 11 shows a plot of the opening angle as a function of bolometric temperature ($T_{\rm bol}$), which is usually considered a reasonable proxy for protostellar evolution (i.e., the more evolved protostars have higher $T_{\rm bol}$ values, see Chen et al. 1995; Ladd et al. 1998). In Figure 11 we identify the protostellar evolutionary class of each source with one of three colors. It can be seen that while there is considerable scatter among protostars of the same evolutionary class, there is a clear trend where the outflow opening angle increases with the protostellar evolutionary stage. The increasing trend in the outflow opening angle is consistent with the ^{12}CO maps shown in Figure 2, and implies that outflows may play an important role in clearing the surrounding envelope material.

4.4. Momentum and Energy Opening Angles

To further understand how the outflow interacts with the surroundings, we investigate the angular distribution of the outflow momentum and energy. We start with estimating the outflow momentum and energy opening angle from the 2D momentum and energy map of each source (as shown in Figures 10 and Figures 21–43 in the Appendices). We calculate the position angle of each pixel in the map, with respect to the source. We then determine the distribution of the average momentum/energy as a function of angle, and fit a Gaussian to estimate the momentum/energy opening angle. The opening angle is defined as the FWQM of the Gaussian fit. The measured momentum, energy opening angles are shown in Figure 12. The outflow momentum and energy opening angles widen as a protostar evolves. To quantify the rate at which the opening angle widens we fitted a power-law $y = 10^c x^m$ to all the angular profiles shown above (see Figure 12). Note that several sources are not included due to a poor Gaussian fit to their momentum/energy angle distribution.

In Figure 13, we show polar plots of the normalized average outflow momentum and energy for each evolutionary class. To construct these plots we normalized the momentum/energy profile (distribution) so that the peak value of each outflow has a value of one, and we then obtained the average profile for each protostellar evolutionary class. Note that the momentum/energy profiles include the high-velocity jets as shown in Figure 8. In Figure 13, it can clearly be seen that the average momentum and energy angular profiles change significantly between different evolutionary classes. For Class 0 sources the energy and momentum are much more collimated, compared to more evolved sources. The vast contrast in the angular profile of energy and momentum between Class 0 and Class I confirms that a significant widening of the outflow momentum and energy angular profile occurs as the protostar evolves.

The significant widening of the angular profiles shown Figure 13 suggests that the impact of protostellar outflows launched on the surrounding environment evolves rapidly at the earliest stage of star formation. In Section 4.1.5 we noted that while molecular outflows from Class 0 sources have a significantly higher momentum rate as compared to those from Class I sources, the total mass-loss rate for Class 0 molecular outflows is lower than the Class I outflows (Figure 9). These results are consistent with a picture in which the high-velocity

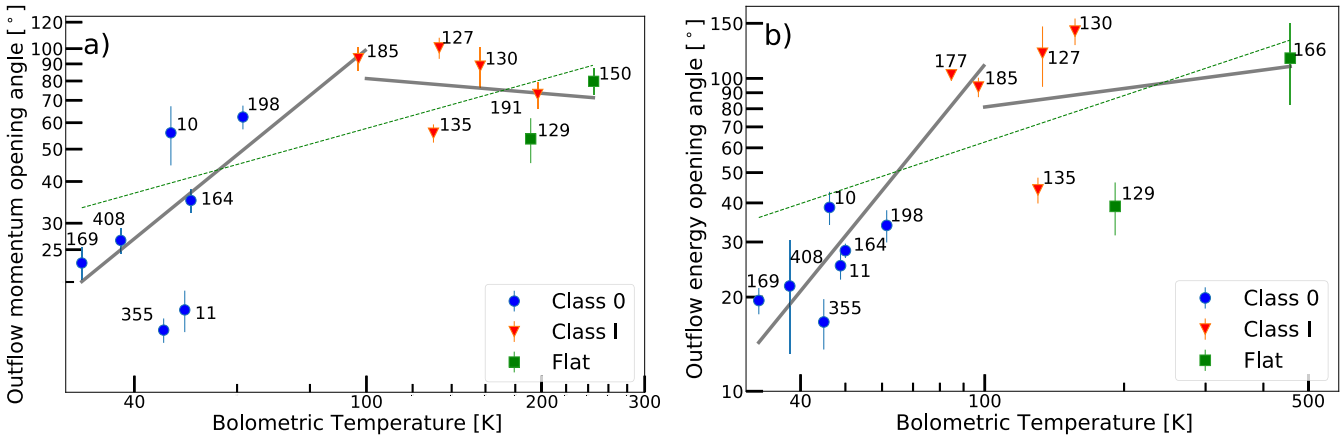

Figure 12. Outflow momentum opening angle (left) and outflow energy opening angle (right) vs. $T_{\rm bol}$ for the sources in our sample. In both panels, the green line represents a power-law fit to all the data using the equation $y = 10^c x^m$. For the momentum opening angle, the fit to all the data gives $m = 0.44 \pm 0.18$ and $c = 0.79 \pm 0.36$. Similarly, for the energy opening angle $m = 0.49 \pm 0.17$ and $c = 0.81 \pm 0.38$. In each panel, the two black lines represent broken power-law fits with a breakpoint at $T_{\rm bol} = 100$ K. For the momentum opening angle, $m = 1.42 \pm 0.32$ and $c = -0.85 \pm 0.60$ for sources with $T_{\rm bol} \leqslant 100$ K, and $m = -0.14 \pm 0.49$ and $c = 2.20 \pm 1.10$ for sources with $T_{\rm bol} > 100$ K. For the energy opening angle, $m = 1.82 \pm 0.28$ and $c = -1.59 \pm 0.52$ for sources with $T_{\rm bol} \leqslant 100$ K, and $m = 0.20 \pm 0.51$ and $c = 1.52 \pm 1.18$ for $T_{\rm bol} > 100$ K. Note that HOPS 150 is taken out for the energy opening angle because it is contaminated by a high-velocity jet from a nearby source outside the field of view. The contamination is much weaker for the momentum map as compared to the energy map. Sources with ill-defined opening angles are not included in the plots. Opening angles have been corrected for the outflows' inclination.

collimated Class 0 jets quickly punch a hole in the protostellar core. Later, in the Class I phase the entrained molecular outflow slows down and is spread out to a much larger volume. We thus expect that the majority of the gas clearing occurs during the Class I stage.

5. Discussion

5.1. On Selection Effects: RM versus R/v$_{max}$ Method

Different methods used in measuring protostellar outflow rates have resulted in values varying by a factor of 5–6 (van der Marel et al. 2013). It is thus important to benchmark the different techniques, identifying all the assumptions and caveats. As described above, we used two methods to determine outflow rates in our sample: the RM and the PFT technique. We first compare our methods with the commonly used dynamical time approach, hereafter the $R_{\rm lobe}/v_{\rm max}$ method, in which dynamical time is estimated by using the simple equation $t_{\rm dyn} = R_{\rm lobe}/v_{\rm max}$, where $R_{\rm lobe}$ is the length of the outflow and $v_{\rm max}$ is the maximum outflow velocity. Outflow mass-loss rate, momentum, and energy injection rate are estimated by dividing the total mass, momentum, and energy by $t_{\rm dyn}$. This method thus (incorrectly) assumes that the molecular gas inside the outflows moves from the source to the current position at a single velocity. In addition, as discussed below, this method highly depends on the sensitivity and extent of the observations.

Using the $R_{\rm lobe}/v_{\rm max}$ method to estimate the mass, momentum, and energy ejection rate of the 21 sources in our survey, we find estimates that are, on average, 80, 350, and 8 times higher than our RM results, respectively. The results highlight the problem of using a single dynamic time to estimate rates. The choice of a characteristic velocity ($v_{\rm max}$), which typically is the maximum velocity relative to the system velocity where ^{12}CO is detected at 3σ, is dependent on the sensitivity of the observations. Previous ALMA observations have revealed molecular outflow emission at much higher velocities than typical single-dish observations (e.g., Arce et al. 2013; Hull et al. 2016). Thus, it is not surprising that with our ALMA data we detect high values of $v_{\rm max}$, which result in extremely large rate estimates when using the $R_{\rm lobe}/v_{\rm max}$ method. This clearly results in an overestimation of the outflow rates as only a small fraction of the outflow mass moves at the highest velocities. For example, for HOPS 10 the $v_{\rm max}$ is close to 100 km s^{-1}. Yet, only 0.9% of the total molecular outflow mass is moving at this high speed.

The $R_{\rm lobe}/v_{\rm max}$ method also suffers from the fact that it depends on the measured outflow lobe length, which depends on the extent of the area observed around the outflow source and the sensitivity of the observations. In our case, all our observations are restricted to 25″ (10,000 au) from the source, which in most cases is significantly smaller than the full extent of the outflow lobe. Hence, our observations would vastly underestimate $R_{\rm lobe}$. We thus stress that this method should not be used to estimate dynamical times and rates as both $R_{\rm lobe}$ and $v_{\rm max}$ highly depend on the observations' parameters. In fact, two different (single-dish) studies with overlapping sources estimate the dynamical timescales of ^{12}CO outflows that differ by a factor of 5 for the same sources (Takahashi et al. 2008; Kang et al. 2021).

The unreliability of selecting outflow length and outflow characteristic velocity for the dynamical timescale estimates may have resulted in conflicting results regarding outflow rates, even in large outflow surveys. Feddersen et al. (2020) studied 45 protostellar outflows in the Orion A molecular cloud using a medium-resolution (8″) CO map. They applied the optical depth correction outlined by Dunham et al. (2014) for the CO maps and they found that the molecular outflow rates are independent of evolutionary stage. This is in conflict with the Atacama Pathfinder Experiment (APEX) ^{12}CO $J = 3-2$ study of 49 sources by Mottram et al. (2017) which found the outflow mass and momentum ejection rates decrease between Class 0 and Class I. Similar trends were also found by Yıldız et al. (2015).

van der Marel et al. (2013) compared seven different methods for obtaining outflow force (i.e., momentum rate). They found that estimates from these different methods can differ by as much as a factor of 6 for an individual source. Most

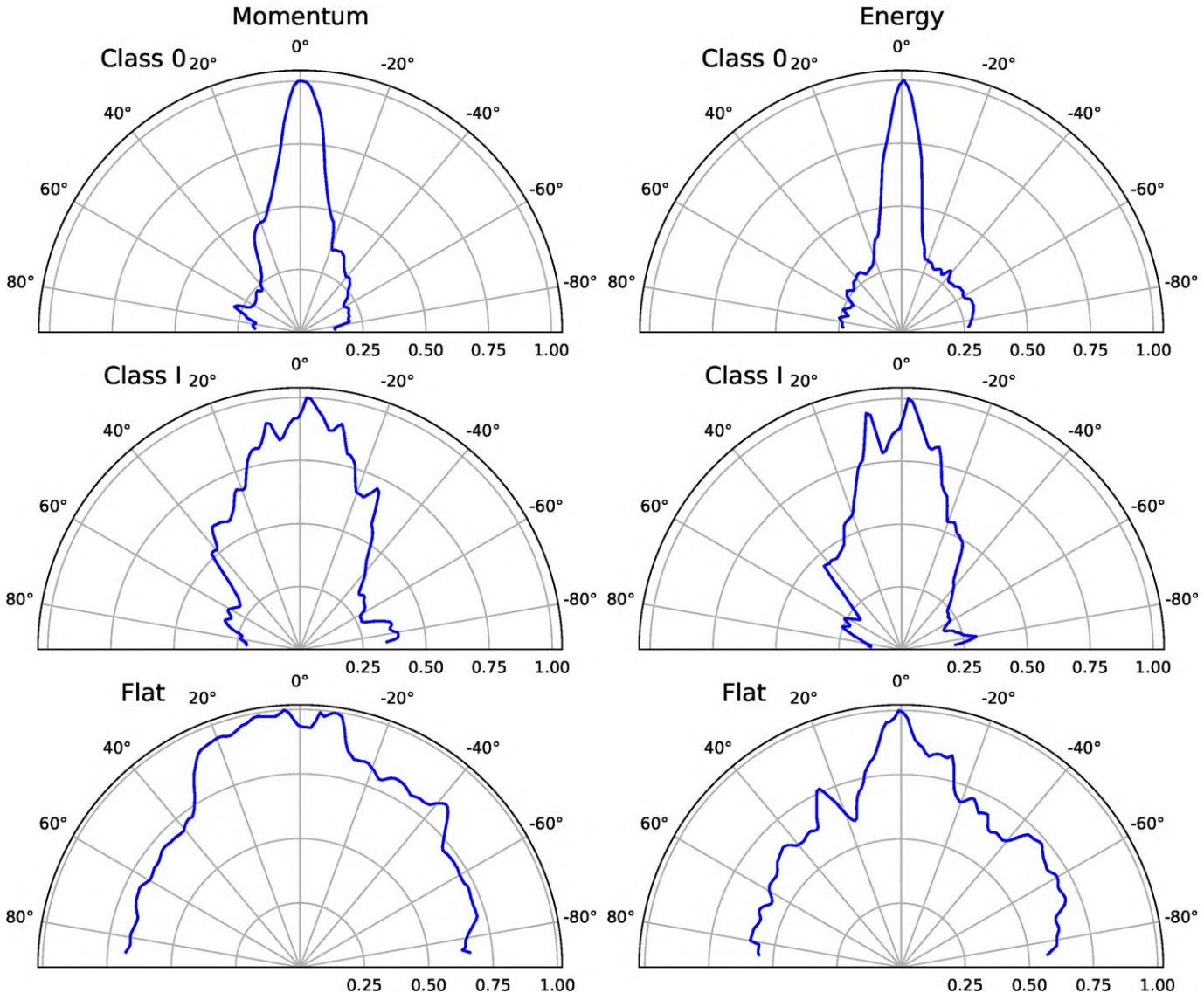

Figure 13. Average normalized momentum (left panels) and energy (right panels) angular profile for protostars at different evolutionary stages: Class 0 (top), Class I (middle), and flat spectrum (bottom). The 0° marks the direction of the outflow axis. All profiles are measured within the region of our maps where the sensitivity falls down to 40% of the peak sensitivity at the center of the map (i.e., 25.″0 radius, or about 10,000 au from the center). Emission perpendicular to the outflow direction (i.e., $\leqslant -85°$ and $\geqslant 85°$) is not used to estimate the average momentum and energy in order to avoid possible contamination from the circumstellar disk/inner envelope material. All angular profiles have been corrected for the outflows' inclination.

of these methods rely on measuring the size of the outflow lobe or maximum outflow velocity. As discussed above these two parameters strongly depend on the strategy and sensitivity of the observation. Of all the methods compared in that study, the annulus method developed by Bontemps et al. (1996) on which we base our RM, seems to be the one that depends the least on observing parameters (e.g., field of view or area covered by observations) and thus we prefer and recommend its use over the other methods discussed in van der Marel et al. (2013).

5.2. Outflow Rates and Bolometric Luminosity

To put our results in context with those of recent studies, we compare our results to those of Nagy et al. (2020, hereafter Nagy20), Kang et al. (2021, hereafter Kang21), and Feddersen et al. (2020, hereafter Fed20)—outflow studies of protostellar outflows from sources in the Orion molecular clouds. To ensure a fair comparison between our results and those of the other studies (and remove any possible bias due to a differing percentage of sources at different evolutionary stages for the different studies), we reestimate the average outflow rates for our sample by multiplying the average rate per evolutionary class we determined (Section 4.1.5) by the percentage of sources in that evolutionary class in the sample of the particular study. For example, in the Fed20 sample, 51% are Class 0 sources, 28% are Class I, and 21% are flat-spectrum sources. We then estimate the expected total molecular outflow mass rate we would derive if our sample had the same composition as that of the Fed20 sample to be $51\% \times 3.5 + 28\% \times 5.6 + 21\% \times 0.8 = 3.5\, M_{\odot}$ Myr^{-1}, where 3.5, 5.6, and 0.8 $M_{\odot}$ Myr^{-1} are the average mass-loss rates we derive from our sample for the Class 0, Class I and flat-spectrum sources, respectively. In Figure 14, we plot the average outflow rates for outflows driven by HOPS sources as determined by Nagy20, Kang21, and Fed20, and we compare them to the average values of our study, corrected for the

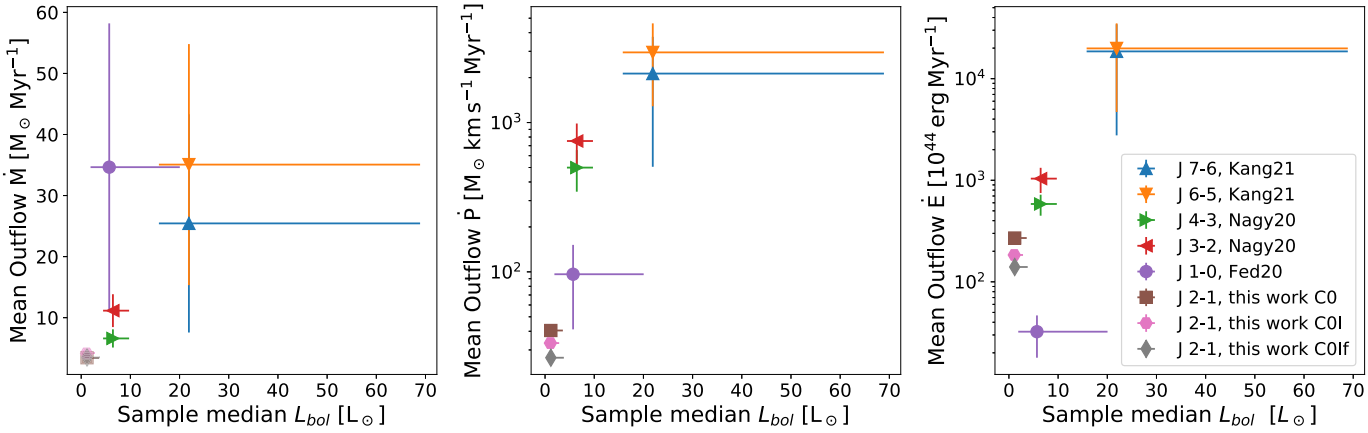

Figure 14. Comparison of molecular outflow rates in Orion A. The left, middle, and right panels show the mean molecular outflow mass rate, momentum rate, and energy rate of various samples against the median bolometric luminosity of the samples, respectively. Different colors represent different samples and CO rotational transitions used to measure the molecular outflow rates. The sample by Nagy20 includes 16 very young Class 0 protostars observed with APEX (Nagy20). The sample by Kang21 is composed of six Class 0 and 3 Class I observed with APEX (Kang21). The Fed20 study includes 45 protostars observed as part of the NRO-CARMA Orion survey (Fed20). C0, C0I, and C0If are the outflow rates from this study, corrected for the sample composition of Nagy20, Kang21, and Fed20, respectively, as described in the text. The numbers in the legend next to the letter J represent the CO transition used in the survey.

sample demographics of these other studies. In the *x*-axis, we plot the median bolometric luminosity for the sample in each study, with error bars showing the range between the first and third quartiles of the $L_{\rm bol}$ values in the sample. In the vertical axis, we plot the sample average rates with error bars representing the standard deviations of the sample sources for Nagy20, Kang21, and our study. For Fed20, the vertical error bars represent the range of values obtained when including and excluding the low-velocity outflow components to estimate the rates.

The most dominant factor that affects the outflow rate measurements is the selection of the source bolometric luminosity range. We see a very clear trend in Figure 14, namely, studies with higher bolometric luminosity samples have significantly higher estimates of molecular outflow rates. The rate estimates can vary by a factor of 100 depending on the sample bolometric luminosity range. Molecular outflow rates obtained from different ^{12}CO transitions only varied by a factor of 2 for studies with the same sources (e.g., Kang21 use the ^{12}CO transitions 7–6 and 6–5). The strong dependence on bolometric luminosity shows that the protostellar outflow feedback varies significantly depending on protostellar mass or accretion rate.

These increasing trends of the molecular outflow rates with bolometric luminosity are consistent with the results shown by Maud et al. (2015) for outflows from massive YSOs, with $L_{\rm bol} > 10^3 L_{\odot}$. Previous studies have shown a clear correlation of the ^{12}CO outflow force (i.e., outflow momentum rate) with the source's bolometric luminosity for a wide range of $L_{\rm bol}$ values, from $\sim 10^{-2}$ to $\sim 10^5 L_{\odot}$ (e.g., Cabrit & Bertout 1992; van Kempen et al. 2016; Maud et al. 2015). From the left and right panels of Figure 14, it appears that the increasing trend with $L_{\rm bol}$ is also present in the outflow mass rate and the outflow energy rate for $L_{\rm bol} < 10^2 L_{\odot}$, and not just for sources with the high values of $L_{\rm bol}$ reported in Maud et al. (2015). It is clear that in order to study (and detect) any possible evolutionary trends in the outflow rates one needs to rigorously control the range in the bolometric luminosity of the sample.

5.3. Outflow Mass Loss as Evidence of Core Growth

Our survey of 21 protostars has found that by the end of the protostellar phase, a typical outflow can displace around 2.2–4.2 $M_{\odot}$ of the core material. However, this estimate includes all the gas that we identified as outflowing gas, and some of it, although perturbed and entrained by the protostellar wind, might still be gravitationally bound to the core. The bounded outflowing gas may eventually fall back toward the protostellar core forming a protostellar version of a *Galactic fountain* (Spitoni et al. 2008). To determine how much core gas could be removed by an outflow, we need to estimate the core's escape velocity. For a 5 $M_{\odot}$ protostellar core, the corresponding escape velocity ($v_{\rm esc}$) at a radius of 10,000 au is $\sim$1 km s^{-1}. Alternatively, for a 2 $M_{\odot}$ protostellar envelope, the corresponding escape velocity ($v_{\rm esc}$) at a radius of 1000 au is about $\sim$2 km s^{-1}. Each protostar has a different escape velocity depending on the mass of the system (protostellar + envelope). Unfortunately, we do not know the mass of each protostar in our sample. Hence, for simplicity, we adopted escape velocities of 1 and 2 km s^{-1} for the whole sample.

We use the RM to calculate the outflow mass-loss rate (as in Section 4.1.5) for gas with a velocity greater than the escape velocity of 1 and 2 km s^{-1}. Note that we assume the outflow gas moves mostly along the direction of the outflow axis, and we use the outflow inclination angle to obtain the gas velocities that we compared with the escape velocity. Some gas is expected to move perpendicular to the outflow direction due to, for example, the thermal expansion of the gas in the post-shock zone behind the working surface (Ostriker et al. 2001; Downes & Cabrit 2007). However, this is expected to be much less massive than the gas that moves along the outflow direction. Hence, for simplicity, we do not include gas moving perpendicular to the outflow direction.

Adopting the protostellar ages for each phase from Dunham et al. (2015), see Table 4, we found that for an escape velocity of 1 km s^{-1}, the outflow will remove 0.4–0.8 $M_{\odot}$ (using an average molecular outflow mass rate of $\overline{M}_{\rm out} = 3.2\ M_{\odot}$ Myr^{-1}) of core material during the Class 0 phase, 1.5–2.8 $M_{\odot}$ (using

Table 4
Total Mass Removed by the Molecular Outflow and Its Corresponding Molecular Outflow Mass-loss Rates at Different Evolutionary Stages for Different Escape Velocities

Class	Duration (Myr)	$\dot{\overline{M}}_{\rm out}$ for All Gas ($M_\odot$ Myr^{-1})	$\dot{\overline{M}}_{\rm out}$ for $v_{\rm esc} \geqslant 1$ km s^{-1} ($M_\odot$ Myr^{-1})	$\dot{\overline{M}}_{\rm out}$ for $v_{\rm esc} \geqslant 2$ km s^{-1} ($M_\odot$ Myr^{-1})	$M_{\rm out}$ for All Gas ($M_\odot$)	$M_{\rm out}$ for $v_{\rm esc} \geqslant 1$ km s^{-1} ($M_\odot$)	$M_{\rm out}$ for $v_{\rm esc} \geqslant 2$ km s^{-1} ($M_\odot$)	Core Mass[a] ($M_\odot$)
0[b]	0.13–0.26	3.5	3.2	2.6	0.5–0.9	0.4–0.8	0.3–0.7	(0.95, 1.04)
I	0.27–0.52	5.6	5.4	4.4	1.5–2.9	1.5–2.8	1.2–2.3	(0.49, 0.49)
Flat[c]	0.27–0.52	0.8	0.7	0.5	0.2–0.4	0.2–0.4	0.1–0.2	(0.46, 0.26)

Notes.
[a] The first value is the average core mass from our ALMA C^{18}O data. The second value is the average core mass derived from the JCMT 850 μm dust continuum data (Lane et al. 2016). Both core mass estimates are measured using a similar core size of ∼6000 au.
[b] HOPS 408 is excluded from these estimates as we were not able to obtain a reliable molecular outflow mass rate for this source.
[c] HOPS 194 and HOPS 166 are excluded from the average as these two sources have significantly higher core mass derived from C^{18}O as compared to the core masses derived from dust continuum. They also have the highest bolometric luminosity (>10 $L_\odot$) in our sample.

$\dot{\overline{M}}_{\rm out} = 5.4\,M_\odot$ Myr^{-1}) during the Class 1 phase, and 0.2–0.4 $M_\odot$ (using $\dot{\overline{M}}_{\rm out} = 0.7\,M_\odot$ Myr^{-1}) in the flat-spectrum phase.

Similarly, for cores with a higher escape velocity of 2 km s^{-1}, the outflow will remove about 0.3–0.7 $M_\odot$ of core material during the Class 0 phase, with an average mass-loss rate of $\dot{\overline{M}}_{\rm out} = 2.6\,M_\odot$ Myr^{-1}, approximately 1.2–2.3 $M_\odot$ of core material during the Class I phase, with an average mass-loss rate of $\dot{\overline{M}}_{\rm out} = 4.4\,M_\odot$ Myr^{-1}, and roughly 0.1–0.2 $M_\odot$ of core material during the flat-spectrum phase with an average of $\dot{\overline{M}}_{\rm out} = 0.5\,M_\odot$ Myr^{-1}. By the end of the protostellar phase, an outflow could remove a total of 2.1–4.0 $M_\odot$ or 1.7–3.2 $M_\odot$ of material from the protostellar core, assuming a core escape velocity of 1 and 2 km s^{-1} respectively. The results are summarized in Table 4. The derived values of the molecular outflow at five different distances from the source for velocity greater than the escape velocity of 1 and 2 km s^{-1}, for all sources in our sample are listed in the Appendices (see Tables 12–17).

The averaged mass of the entrained outflow gas derived from our sample is comparable to or larger than the median of the protostellar core mass in the Orion A cloud (Takemura et al. 2021) and the median of the core mass in the Dragon infrared dark cloud (Kong et al. 2021). We also use our ALMA Cycle 6 C^{18}O data, as well as the James Clerk Maxwell Telescope (JCMT) 850 μm dust continuum core catalog identified by Lane et al. (2016), to drive the mass of the cores harboring the protostars in our samples (see Tables 1 and 4). Both mass estimates were measured using a similar core size of ∼6000 au. Note that HOPS 408, HOPS 166, and HOPS 194 are excluded in the averaged outflow rate, mass estimates, and the averaged core mass in Table 4.

From Table 4, for an escape velocity of 1 km s^{-1} we found that around 40%–80% of the average core mass would be removed by the protostellar outflow by the end of Class 0. For Class I, the mass removed by the protostellar outflow is 3–6 times the average mass of a core in this stage. For flat-spectrum sources, we estimate that the outflow will remove around 43%–87% or 77%–154% of the core mass, depending on whether we assume an average core mass derived from C^{18}O and dust continuum, respectively. Protostellar cores generally do not live in isolated environments, but instead are embedded in larger filaments and clouds (André et al. 2014; Hsieh et al. 2021). The high percentage of total core mass removed by outflows at each protostellar phase implies that the mass budget of the protostellar core must be continuously replenished by material from larger scales.

The biggest uncertainty in quantifying the mass loss by protostellar outflows at each evolutionary stage is the time a protostellar system stays in each evolutionary class. The lifetime estimates we used here, reported by Dunham et al. (2015), are one of the most commonly used. Kristensen & Dunham (2018) use a different technique, a nuclear decay half-life model, to derive the duration of each evolutionary class. Converting the derived half-life to the average lifetime for each stage, the derived lifetimes for Class 0, Class I, and flat-spectrum sources are 68 ± 6, 130 ± 10, and 126 ± 12 kyr, respectively. They are a factor of 2 and 4 lower than the lower and upper bound of the lifetimes estimated by Dunham et al. (2015). Dunham et al. (2014) and Megeath et al. (2022) obtained protostellar lifetimes longer than the lifetimes from Kristensen & Dunham (2018), but shorter than the values in Dunham et al. (2015). Even if we were to adopt the duration of the protostellar evolutionary classes from Kristensen & Dunham (2018) this would only lower the total core mass removed by protostellar outflows by a factor of 2, which is still a significant fraction of the total average core mass.

Recent studies have found a clear mass difference between the protostellar and starless core in the Dragon infrared dark cloud (a.k.a., G28.37+0.07 or G28.37+0.06) (Kong et al. 2021). Adopting a typical temperature of 20 K from the Herschel dust temperature map, the authors found that the medium value for protostellar core masses is 2.1 $M_\odot$, and for starless cores, it is 0.37 $M_\odot$. Protostellar cores are found to have similar densities but larger sizes as compared to starless cores. The mass difference can be attributed to the continuous mass accretion onto the protostellar cores from filaments, as predicted by simulations (Li & Klein 2019). The high protostellar outflow mass loss from our ALMA survey poses serious challenges to the current concept of *static* cores, as a well-defined reservoir of mass, and the simplified core-to-star conversion ideas. Together with evidence of core growth predicted by simulations (e.g., Li & Klein 2019) and results from other observational studies (e.g., Kong et al. 2021), our results point to a more dynamic star formation at core scales.

5.4. Evolution of Conventional Outflow Opening Angle

Protostellar outflows play an important role in core dispersal and setting the stellar mass (Myers 2008; Guszejnov et al. 2022). The Spitzer Cores to Disks (c2d) legacy survey of 265

and 353 sources in Ophiuchus and Perseus has shown that all Class 0 protostars have associated cores observed by the SCUBA instrument on JCMT. The number declines to around 50% for Class I and less than 3% for more evolved Class II and Class III sources (Jørgensen et al. 2008). A study of the spectral energy densities of 330 YSOs in HOPS has shown that the envelope volume density drops by a factor of 50 between Class 0 and flat-spectrum sources (Furlan et al. 2016). Many simulations suggest that outflows are responsible for the dispersion of the protostellar core (Machida & Hosokawa 2013; Offner & Arce 2014; Offner & Chaban 2017). Outflows from Class 0 sources are very collimated and therefore only impact a very limited volume, so if outflows are responsible for core dispersal, they need to become wider as they evolve. The widening of the outflow cavity found in multiple observations has suggested the impacted volume for outflow–core interactions increases over time (Arce & Sargent 2006; Velusamy et al. 2014; Hsieh et al. 2017).

The recent STARFORGE simulations have shown that the widening of the outflow cavity allows protostellar outflows to disturb the accretion flows around the protostars, causing the gas to fragment into more low-mass stars, setting the mass scale of stars and circumstellar disks (Guszejnov et al. 2022). These numerical simulations also indicate that the peak of the IMF is sensitive to the momentum loading factor of the protostellar jets (Guszejnov et al. 2022). Outflows are believed to be the main explanation for the low core-to-star efficiency of 30% (Alves et al. 2007). Understanding how outflows interact with the protostellar core is one of the major questions in star formation, and the *outflow opening angle* is one of the key parameters for understanding the outflow–core interaction.

We investigate the evolution of the outflow opening angles using our sample of 21 sources, which includes seven sources of each of the protostellar classes (Class 0, Class I, and flat spectrum). Performing a least-squares fit to our data, as shown in Figure 11, we find a correlation between the outflow opening angle ($\Theta_{\rm FWQM}$) and the bolometric temperature ($T_{\rm bol}$) as

$$\log\left(\frac{\Theta_{\rm FWQM}}{\rm deg}\right) = (1.5 \pm 0.2) + (0.18 \pm 0.09)\log\left(\frac{T_{\rm bol}}{\rm K}\right). \quad (10)$$

This is much shallower than the relationship derived from Arce & Sargent (2006) based on the lower resolution 5.″0 (interferometer) maps of the ^{12}CO outflows of 17 sources (combining results from their own survey and the literature):

$$\log\left(\frac{\Theta_{\rm FWQM}}{\rm deg}\right) = (1.7 \pm 1.7) + (0.38 \pm 0.96)\log\left(\frac{T_{\rm bol}}{\rm K}\right). \quad (11)$$

The difference in slope might be caused by the fact that the Arce & Sargent (2006) study did not correct the outflow opening angle for the outflow inclination. We conduct the same fit with our ALMA data using the opening angles without inclination correction in Appendix G and find the slope to be 0.38 ± 0.06, which is consistent with the results obtained by Arce & Sargent (2006).

A study of the outflow opening angle based on the Spitzer IRAC image of 31 YSOs by Velusamy et al. (2014) showed a clear increase in opening angle with age, with a break at 8000 yr (which corresponds to a $T_{\rm bol}$ of about 82 K), where the relationship then becomes approximately flat:

$$\log\left(\frac{\Theta_{\rm FWQM}}{\rm deg}\right) = \begin{cases} 2.05 + 0.76\log\left(\frac{T_{\rm bol}}{\rm K}\right), & T_{\rm bol} < 82{\rm K} \\ 2.03 + 0.05\log\left(\frac{T_{\rm bol}}{\rm K}\right), & T_{\rm bol} > 82\ {\rm K}. \end{cases} \quad (12)$$

The power-law index of 0.76 derived by Velusamy et al. (2014) for younger YSOs is consistent with our high-resolution CO study with the power-law index of 1.24 for sources with $T_{\rm bol} \leqslant 100$ K. For more evolved sources, the small power-law index of 0.05 in Velusamy et al. (2014) suggests little or no widening of the outflow cavity after Class 0 ($T_{\rm bol} \geqslant 70$ K). Our ALMA data also shows the widening of opening angles slows down for sources with $T_{\rm bol} \geqslant 100$ K. Velusamy et al. (2014)'s result is consistent with the power-law index derived from our fit (0.10 ± 0.19).

Our results indicate that the widening of the outflow cavity slows down in Class I and flat-spectrum sources as shown in Figure 11. For Class I and flat-spectrum sources, it is unclear whether or not the opening angle continues to (slightly) increase due to the large uncertainty in the fit. We conducted a Spearman rank-order test and a Pearson correlation test for the entire sample. We found that the correlation coefficients are 0.49 and 0.44 with p-values of 0.04 and 0.07, respectively. As for the more evolved sources ($T_{\rm bol} \geqslant 100$ K), we found a weak correlation with correlation coefficients of 0.40 and 0.20 and p-values of 0.29 and 0.60 for both tests. For the younger sources ($T_{\rm bol} \leqslant 100$ K), there is a strong positive relationship with correlation coefficients of 0.84 and 0.86 and p-values of 0.004 and 0.003, respectively. The statistical tests show a strong correlation between outflow opening angles and bolometric luminosity for the younger sources. The large p-values for the evolved sources are mostly due to the large scatter in the measurements. A larger sample is needed to determine whether the flattening in the opening angle–$T_{\rm bol}$ relation for evolved sources ($T_{\rm bol} \geqslant 100$ K) is real or due to a lack of fully mapped outflows at these later stages of protostellar evolution.

The flattening of slope for the outflow opening angles found by Velusamy et al. (2014) is consistent with a recent study using Hubble Space Telescope (HST) NIR scattered light images of 30 protostars, which shows no widening of the outflow cavities in protostars (Habel et al. 2021). They also find evolved protostars with narrow cavities. The results from this HST study may partially be attributed to the infrared scattered light tracing a potentially narrower range of protostar ages with similar envelope optical depth (the sample is strongly dominated by Class I sources). High optical depths in the envelopes of younger more embedded sources (i.e., Class 0 sources) reduce the number of infrared photons illuminating the outflow cavity. Similarly, if the density of the outflow cavity is too low (e.g., flat-spectrum sources), it would also make it more difficult to scatter infrared photons. This could introduce a bias in the sample of the IR studies, which results in the flattening or lack of trend found in the evolution of outflow opening angles.

The flattening of the outflow opening angle as protostars evolve might be partially attributed to the method used in inclination angle correction. The slope of the outflow opening angle versus bolometric temperature is shallower when an inclination angle correction is applied. Our inclination correction for the outflow opening angle is based on a simple conical

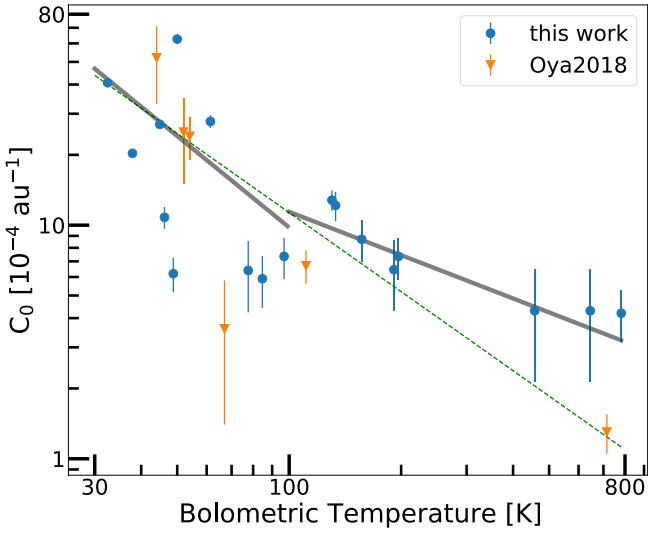

Figure 15. Evolution of the outflow curvature (C_0) from the wide-angle wind model. The orange points denote literature values from Oya et al. (2018), which are also included in the fit. The thin-dashed green line represents a power-law fit of all the data described by equation $y = 10^c x^m$, with $m = -1.12 \pm 0.38$ and $c = 3.30 \pm 0.64$. The two thick gray lines represent the broken power-law fits with a break at $T_{\rm bol} = 100$ K. For $T_{\rm bol} \leqslant 100$ K, $m = -1.30 \pm 0.72$, and $c = 3.59 \pm 1.20$; $T_{\rm bol} > 100$ K, $m = -0.62 \pm 0.20$, and $c = 2.29 \pm 0.44$. Outflow curvature is an alternative way to quantify the outflow width. It is not affected by the source inclination angle and no inclination correction is needed.

outflow projection model. To test whether or not the flattening of the outflow opening angle is due to our inclination correction prescription, we measured the outflow curvature, an alternative way to quantify the outflow width, by fitting the wide-angle wind model to the outflows in our sample. Opening angles derived by using the curvature of the parabolic outflow shell from the wide-angle wind model are not affected by inclination angle, and no inclination correction is needed (Oya et al. 2018). We modeled the position–velocity (PV) diagrams perpendicular and parallel to each protostellar outflow and compare them with wide-angle wind models. The detailed modeling is described in Appendix B, and an example is shown in Figure 19. The parameters of the best wide-angle wind models for each source are summarized in Table 6.

In Figure 15, we plot the evolution of outflow curvature (outflow curvature versus outflow source bolometric temperature). The green line represents the best power-law fit through all the data points, including the literature values from Oya et al. (2018). The two thick gray lines represent the broken power-law fits with a break at $T_{\rm bol} = 100$ K. For $T_{\rm bol} \leqslant 100$ K, $m = -1.30 \pm 0.72$, and $c = 3.59 \pm 1.20$; for $T_{\rm bol} > 100$ K, $m = -0.62 \pm 0.20$, and $c = 2.29 \pm 0.44$. We see a clear flattening of outflow curvature for more evolved sources, as shown in Figure 11. The agreement of outflow curvature from the wide-angle wind modeling, which is not affected by the inclination angle, and the outflow opening angle derived from integrated intensity maps suggests that the flattening trend is not an artifact introduced by our inclination correction.

In addition, different methods of measuring the protostellar outflow cavity can result in different opening angles. For example, Habel et al. (2021) used an edge detection technique combined with power-law fits to determine the opening angle and cavity volume. The cavity half-opening angle is defined at an envelope radius of 8000 au. Adopting a different radius would change the values of the opening angles. While the absolute values of opening angles are dependent on the methods, samples using the same method should result in the same trend. Studies comparing different methods in determining the outflow cavity opening angles, similar to the study by van der Marel et al. (2013), which compared outflow momentum rates using different techniques, are needed to establish the scaling relationships between each method.

In Section 5.2 we showed that outflow rates depend on the bolometric luminosity of the source, and thus it is preferable that sources in a sample have a narrow range of $L_{\rm bol}$ to detect evolutionary trends. Bolometric luminosity is a commonly used proxy for protostellar mass (e.g., Scandariato et al. 2012). It is still an open question whether the opening angle evolves differently for low-mass and high-mass stars or sources with vastly different values of $L_{\rm bol}$. However, Habel et al. (2021) did not find any clear trend of outflow opening angles versus bolometric luminosity ($L_{\rm bol}$) over a sample range of 4 orders of magnitude in $L_{\rm bol}$.

To investigate how the evolution of the outflow opening angle might depend on the protostellar mass, one place to look is by comparing our results to those obtained for low-luminosity objects (LLOs). The Canada–France–Hawaii Telescope *K*-band study of the opening angle using 12 LLOs, with luminosity ranges of $0.1L_\odot \leqslant L_{\rm int} \leqslant 0.2L_\odot$, shows a steeper power-law slope than our study (Hsieh et al. 2017):

$$\log\left(\frac{\Theta}{\rm deg}\right) = (-1.42 \pm 0.39) + (1.64 \pm 0.21)\log\left(\frac{T_{\rm bol}}{\rm K}\right). \quad (13)$$

The bolometric luminosity is composed of both internal and external luminosity ($L_{\rm bol} = L_{\rm int} + L_{\rm ext}$), where the external luminosity ($L_{\rm ext}$) is due to the heating of the envelope by the external, interstellar radiation field and is on the order of few tenths of $L_\odot$ (Dunham et al. 2008). For our study, the ranges of $L_{\rm bol}$ within the first and third quartiles are $0.58L_\odot \leqslant L_{\rm bol} \leqslant 3.82L_\odot$.

LLOs can be low-mass protostars, extremely young protostars, or protostars in a quiescent phase of episodic accretion (Schwarz et al. 2012; Dunham et al. 2014; Jørgensen et al. 2015; Kim et al. 2016). Recent observations have shown *two wind components*, a collimated jet, and a wide-angle disk wind, coexist in protostellar outflows (e.g., Lee et al. 2021). At an early stage, due to the high column density of the dense envelope, only the collimated jet component can break out, forming the jet-like outflows seen in Class 0 sources. As the envelope dissipates and accretes toward the central star-disk system over time, the wide-angle wind component starts to break out causing the outflow cavity to widen (e.g., Arce & Sargent 2006). LLOs tend to drive much weaker outflows, and low luminosity can generally be attributed to a low accretion rate (Hsieh et al. 2017). The envelope mass strongly correlates with bolometric luminosity $M_{\rm env} \propto L_{\rm bol}^{0.6}$ (Duarte-Cabral et al. 2013). Thus, the selection of LLOs systematically favors systems with less envelope mass. In systems with significantly lower envelope mass, the wide-angle wind component could break out more easily, causing the outflow cavity to widen at a much earlier phase resulting in a much faster widening rate of the outflow cavity compared to higher luminosity sources. The larger power-law index found by Hsieh et al. (2017) in their low-luminosity sample compared to the index found in our study (see Figure 11) may be caused by the rapid widening of the outflow cavity in LLOs.

Alternatively, it is possible that in these systems, the rapid widening of outflow cavities accelerates the removal of core gas resulting in a much lower envelope density, lower accretion rate, and eventually lower bolometric luminosity. If that is the case, the rapid widening of outflow cavities in LLOs would be the cause rather than the result of gas dispersal in LLOs.

5.5. Evolution of Outflow Momentum and Energy Opening Angles

The study of outflow cavity walls (as discussed above) has usually been conducted by measuring the outflow opening angle based on (integrated) intensity maps of CO or IR emission, which we henceforth refer to it as the conventional outflow opening angle. The conventional outflow opening angle has been widely used as an indicator of how much material is impacted or cleared by the outflow and to determine whether or not the outflow–core interaction is responsible for the low-star formation efficiency (e.g., Arce & Sargent 2006; Velusamy et al. 2014; Hsieh et al. 2017; Habel et al. 2021). While intensity maps likely trace the distribution of matter and the size of the outflow cavity, the velocity information, which is crucial for the outflow–core interaction, is missing from this picture. To capture the dynamics of outflow–core interaction and fold in the velocity information, we investigate two new quantities: the outflow momentum ($P_{\rm out}$) opening angle, and the outflow kinetic energy ($E_{\rm out}$) opening angle. Comparing these quantities for sources at different evolutionary stages allows us to quantitatively study how the angular distribution of outflow momentum and energy evolves.

The least-squares fits[17] to the momentum and energy opening angle as a function of $T_{\rm bol}$ are

$$\log\left(\frac{\Theta_{\rm P}}{\rm deg}\right) = (0.79 \pm 0.35) + (0.49 \pm 0.16)\log\left(\frac{T_{\rm bol}}{\rm K}\right), \quad (14)$$

$$\log\left(\frac{\Theta_{\rm E}}{\rm deg}\right) = (0.81 \pm 0.38) + (0.49 \pm 0.17)\log\left(\frac{T_{\rm bol}}{\rm K}\right). \quad (15)$$

Similar to the conventional opening angle, we find a clear trend in which the momentum and energy opening angles increase as protostars evolve. The trend appears to flatten for more evolved sources as shown in black lines in Figure 12. However, if we take out HOPS 166, the source with the highest bolometric luminosity and the highest $C^{18}O$ core mass, both the momentum and energy opening angles would not show signs of flattening. More later-stage Class I and flat-spectrum sources are needed to determine whether the $P_{\rm out}$ and $E_{\rm out}$ opening angles continue to increase or flatten at later protostellar evolutionary stages.

Comparing the momentum and energy opening angles with the conventional outflow opening angles shows that typically the outflow momentum and energy opening angles are around 10°–20° smaller than the conventional opening angle, especially in Class 0 sources (see Appendix G). The much narrower momentum and energy outflow opening angles in Class 0 sources show that $P_{\rm out}$ and $E_{\rm out}$ are concentrated in collimated jets at these early stages. As sources evolve, the outflow momentum and energy are transferred to the surrounding medium at a wider range of angles, resulting in a much steeper slope (Figure 12) as compared to the conventional outflow opening angle measured from integrated intensity maps.

The most important consequence of narrower momentum and energy opening angles in Class 0 is that this indicates that the amount of gas entrainment is less in Class 0 sources as compared to Class I sources. The extremely collimated nature of outflows from Class 0 sources suggests these young outflows only impact a limited volume inside a protostellar core. Our results from Section 4.1.5 indicate that outflows from Class I show, on average, higher mass outflow rates than those from Class 0 sources (see Figure 9). This supports the idea that Class I outflows entrain more mass from the surrounding environment than younger sources. This is consistent with Figure 13, which shows that the angular width of momentum and energy profile with respect to the outflow axis increases for more evolved sources.

Studying the evolution of outflow opening angle or cavity size identified using integrated intensity maps in ^{12}CO (e.g., Arce & Sargent 2006), or infrared scattered light (e.g., Tobin et al. 2007; Seale & Looney 2008; Habel et al. 2021) has been one of the main techniques used to understand the feedback of outflows in halting accretion, dispersing the core and reducing the star formation rate in the past two decades. The outflow opening angle has been used to estimate the volume and mass affected by the outflow. To study the outflow–core interactions and determine feedback from outflows on core-to-star efficiency, one should also study the momentum or energy opening angles, which incorporate the velocity information. The evolution of the angular distribution of $P_{\rm out}$ and $E_{\rm out}$ is an important complement to the conventional outflow opening angles in determining how much core material is impacted by protostellar winds.

5.6. Theoretical Angular Distribution of Momentum

The momentum angular distribution of winds launched by protostar-disk systems has been studied theoretically, but observational studies on this topic have been scarce. Matzner & McKee (1999) indicate that for any hydromagnetic protostellar wind the normalized angular distribution of the wind momentum can be described with the following equation:

$$\zeta(\theta, \theta_0) = \left[\ln\left(\frac{2}{\theta_0}\right)(\sin^2\theta + \theta_0^2)\right]^{-1}, \quad (16)$$

where θ is the polar angle measured from the protostar's rotation axis, and θ_0 is the parameter that quantifies the angular width of the momentum profile. This equation describes the momentum angular distribution of the protostellar wind directly ejected from the central star-disk system. However, in the observation we measure the momentum of the molecular outflow, which is the entrained gas. The outflow entrainment mechanism (i.e., the wind–cloud interaction that produces the observed molecular outflow) is expected to be a momentum-conserving interaction, and therefore if the launched wind's axis does not change with time, then we would expect the molecular outflow momentum

[17] These are not weighted fits. The error bars in Figure 12 show the uncertainty of the Gaussian fits to the angular profile of the outflows' momentum and energy, used to quantify the width of these quantities. The uncertainties represent the range of possible values for the opening angles and arise from the deviation of the measured angular profile from a Gaussian function. They are not due to random errors. Therefore, we do not use them as weights for our power-law fits.

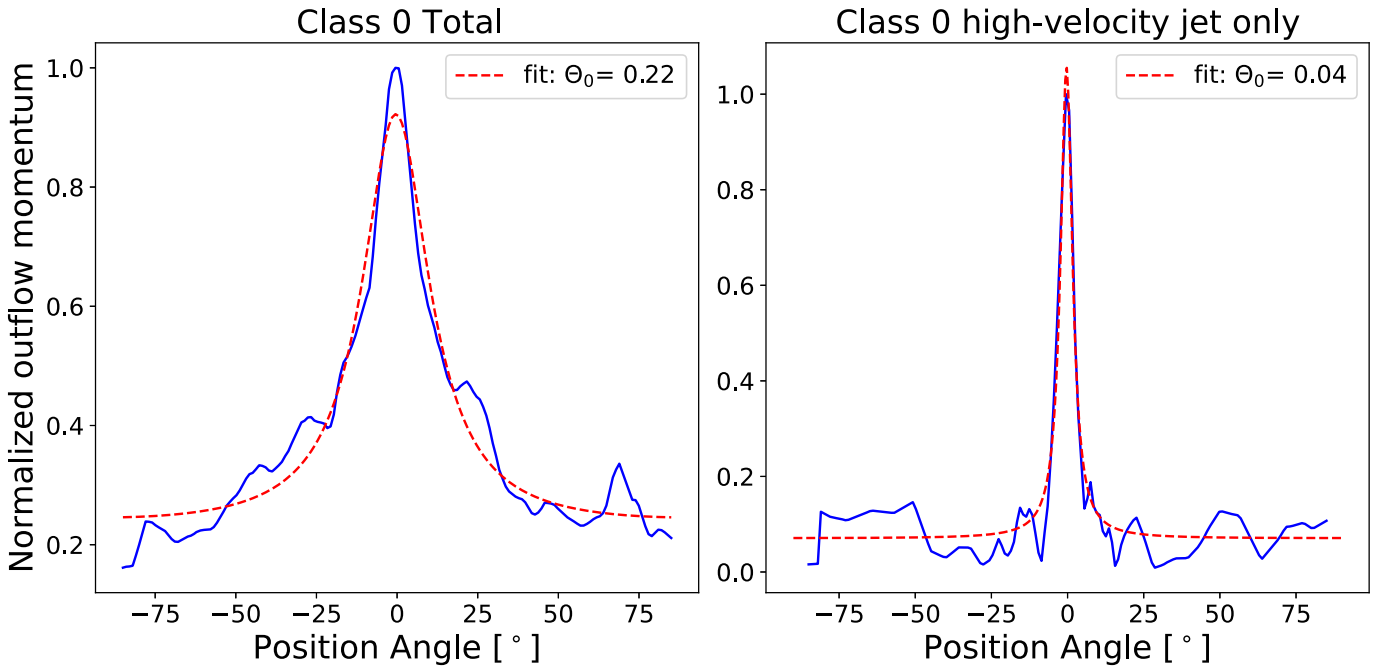

Figure 16. Normalized average outflow momentum angular profile for Class 0 protostars with no sign of outflow precession. The left figure shows the total (average) momentum profile (includes molecular outflow emission at all outflow velocities), and the right figure shows the average momentum profile for the high-velocity jets (HOPS 10 and HOPS 164) identified in Figure 8. The red-dashed line shows the best fit using the theoretical model from Equation (16). All angular profiles have been corrected for the outflows' inclination.

profile to be similar to that of the protostellar wind. For highly embedded, young protostars (i.e., Class 0 sources) there is still enough material throughout the envelope that the entrained material should trace well the wind momentum. Thus, the momentum angular profile of molecular outflows from Class 0 sources with no clear axis wandering (i.e., no change in outflow axis direction), should trace reasonably well the momentum angular distribution of the underlying protostellar wind.

In Figure 16 we compare the observed molecular outflow momentum angular distribution with the distribution predicted by Matzner & McKee (1999). In the left panel of Figure 16, we show a fit to the average angular distribution of molecular outflow momentum from Class 0 outflows with the generalized radial hydromagnetic wind profile (Equation (16)). When constructing this plot we exclude the outflows from HOPS 11 and HOPS 169 as they show signs of precession, and the outflow from HOPS 408 because it is barely resolved. In the right panel of Figure 16, we show only the average outflow momentum profile for the high-velocity jet component from HOPS 10 and HOPS 164 (the two non-precessing Class 0 outflows with clear jets, see Figure 8). The average angular momentum profile is clearly more collimated in the jet component (with a $\theta_0 = 0.04$) compared to the profile obtained when considering all molecular outflow emissions at all velocities ($\theta_0 \sim 0.2$).

Matzner & McKee (1999) proposed that the momentum distribution in protostellar winds should be strongly collimated with a $\theta_0 \leqslant 0.05$ resulting in an extremely peaked profile with the majority of the momentum concentrated along the outflow axis. This is consistent with our Class 0 high-velocity molecular jet momentum profile. However, when including the low-velocity molecular component, the momentum profile is significantly wider.

We may interpret these results in various ways. One possible interpretation is that (non-precessing) jet-like prostellar winds can produce a much wider molecular outflow, even if the original wind has a very narrow momentum angular distribution and without the aid of another (much wider) wind component. This could be produced, for example, by the sideways ejection of material by a series of internal working surfaces (Raga et al. 1993), turbulent mixing of the jet and a turbulent envelope (Offner & Chaban 2017), or the expanding shell driven by a pulsed jet in a stratified core (Rabenanahary et al. 2022).

Another possible interpretation is that if we assume that molecular outflows are solely produced by the direct (momentum-conversing) interaction between the underlying jet and surrounding envelope (and no other mechanism like those described above can produce a wider outflow), then the momentum angular distribution of the underlying jet should be significantly wider (i.e., $\theta_0 \sim 0.2$) than what was proposed by Matzner & McKee (1999) and what is usually used in simulations (e.g., Cunningham et al. 2011; Offner & Chaban 2017). However, Offner & Arce (2014) ran various simulations of the protostellar outflow evolution and gas entrainment in a core using different values of θ_0 and found that even highly collimated outflows can entrain a significant amount of core gas and produce relatively wide molecular outflows. Yet, in that study, the wide outflow cavities are likely partially caused by the change in the outflow axis seen in the simulations. In making the plots shown in Figure 16 we only used outflows that exhibit a constant outflow axis direction, in order to exclude any possible molecular outflow widening due to a wandering jet (as seen in the models by, e.g., Masson & Chernin 1993; Rosen & Smith 2004). Thus, comparing our results with those of simulation with jets with a time-varying axis direction is not a fair comparison.

Yet another possible interpretation of our results is that there exist two wind components; a very collimated jet-like wind (e.g., Shu et al. 2000) and a wider (likely disk-driven) wind (e.g., Konigl & Pudritz 2000). In such a scenario, the (slower) wide-angle parts of the molecular outflow are driven by a disk wind, while the more collimated (high-velocity) component is driven by a jet-like wind. A thorough comparison of our sample of

protostellar molecular outflows with different wind and entrainment models is needed in order to determine which of the scenarios described above is the most consistent with our data.

6. Conclusions

This paper has presented ALMA multiline observations of the protostellar environment around 21 protostars at different evolutionary stages. In short, the results can be summarized as follows:

1. We argue that the widely used method of estimating outflow rates using a single dynamical time, obtained by dividing a characteristic length by a characteristic velocity, is unreliable. To better estimate outflow properties and their impact on their surrounding, we devised the PFT technique and modified the *annulus method* developed by Bontemps et al. (1996) to measure outflow mass, momentum, and energy ejection rates. The PFT technique allows us to compute two-dimensional molecular outflow instantaneous rate maps for the first time. Instead of a single rate value obtained by previous methods, these maps contain spatial information on how the molecular outflow mass, momentum, and energy rates vary within the outflow cavity.
2. On average, molecular outflows from Class 0 sources have significantly higher momentum and energy ejection rates than those of more evolved protostars. However, molecular outflows from Class I sources have, on average, a 60% higher outflow mass rate compared to their Class 0 counterpart. This higher molecular outflow rate is partly due to the larger molecular outflow volume. Our results suggest that the dissipation of protostellar cores starts when a Class 0 protostar quickly opens up a hole with a high-velocity collimated jet. Then, in the Class I phase the molecular outflow cavity widens and a larger volume of core gas is impacted by the outflow.
3. We find that by the end of the protostellar phase, a typical low-mass protostar will displace approximately 2–4 $M_{\odot}$ of mass from the surrounding envelope. Similarly, we expect molecular outflows to inject a total momentum and energy of about 11–22 $M_{\odot}$ km s^{-1} and about 4–8 $\times$ 10^{45} erg into their natal cores by the end of the protostellar phase. Adopting the lifetimes for the different protostellar evolutionary phase from Dunham et al. (2015), our results indicate that the mass removed by outflows from Class 0, Class I, and flat-spectrum sources are 40%–80%, 300%–600%, and 40%–150% of the (current) average estimated core mass, respectively. Thus, the total mass removed by outflows throughout the protostellar stage is comparable to or larger than the current protostellar core mass. This strongly suggests that the mass budget of protostellar cores is continuously replenished by accretion from cloud gas at larger scales. The high-mass loss from protostellar outflows poses serious challenges to the current concept of *cores as the primary reservoir of stellar mass*, and thus has strong implications for the origin of the IMF, and the simplified core-to-star conversion scenario.
4. The results from our study of 21 protostellar outflows at different evolutionary stages show that consistent with previous studies, the molecular outflow opening angle increases with the protostellar evolutionary phase, as traced by the bolometric temperature ($T_{\rm bol}$). The rate at which the opening angle widens the decline significantly for more evolved sources ($T_{\rm bol} \geqslant 100$ K), compared to younger (Class 0) sources. Yet, more outflows from more evolved protostars are needed to confirm the observed trend for Class I and flat-spectrum protostars.
5. To study the effect of outflow–core interactions, we introduced two new quantities, the outflow momentum opening angle and the outflow energy opening angle, which quantify the angular profile of outflow momentum and energy. Our results show steeper slopes in the momentum and energy opening angles versus $T_{\rm bol}$ plots compared to that of the traditional opening angle. This indicates that the outflow momentum and energy are considerably more collimated (i.e., concentrated toward the outflow axis) in the Class 0 phase than at later evolutionary stages. The evolution of the angular distribution of the outflow momentum and energy is an important complement to the traditional opening angles in determining the volume fraction of the surrounding envelope impacted by molecular outflows.
6. Comparing the results of recent molecular outflow surveys in Orion with our results indicates that molecular outflow rates significantly depend on the protostellar bolometric luminosity. The strong dependence on bolometric luminosity suggests that protostellar outflow feedback varies significantly depending on protostellar mass or accretion rate.
7. We find that in Class 0 molecular outflows, the collimated high-velocity component has a narrow momentum angular distribution consistent with that expected for hydromagnetic winds. However, the average molecular outflow momentum angular distribution is significantly wider when including the molecular outflow emission at all velocities. We argue that this could be interpreted in various ways. One possibility is that highly collimated winds may be able to produce molecular outflows that are much wider than the driving jet. On the other hand, it may be that the original (driving) wind is wider than the collimated jets generally assumed in simulations. Yet another possibility is that two coexisting wind components (one jet-like and the other a wide-angle wind) entrain the surrounding core gas to produce the observed molecular outflow. Further comparison between molecular outflow observations and wind entrainment models is needed to determine which of these scenarios describes best the data.

C.H.H. acknowledges support from the National Radio Astronomy Observatory (NRAO) Student Observing Support (SOS). H.G.A. and C.H.H. acknowledge support from NSF award AST-1714710. Z.Y.L. is supported in part by NASA 80NSSC 20K0533 and NSF AST-1910106. A.S. gratefully acknowledges support by the Fondecyt Regular (project code 1220610), and ANID BASAL projects ACE210002 and FB210003. S.T.M. received funding from NSF AST grant 210827 and NASA ADAP grants 80NSSC19K0591 and 80NSSC18K1564. SSRO acknowledges funding support from NSF Career 1748571. This paper makes use of the following ALMA data: ADS/JAO.ALMA #2018.1.00744.S ALMA is a partnership of ESO (representing its member states), NSF (USA) and NINS (Japan), together with NRC (Canada) and NSC and ASIAA (Taiwan) and KASI (Republic of Korea), in cooperation with the Republic of Chile. The Joint ALMA Observatory is operated by ESO, AUI/NRAO and NAOJ. The National Radio Astronomy Observatory is a facility of the National Science Foundation operated under cooperative agreement by Associated Universities, Inc.

Appendix A
Cloud Subtraction

TP array data is sensitive to large-scale emission and is crucial to recover the outflow mass. However, while it recovers the large-scale outflow emission it also picks up the cloud emission. Even though we tried to avoid including cloud emission by not including velocity channels in the outflow maps that were close to the cloud velocity, there were several sources in which emission from the parent cloud (or extended *contaminating* CO emission at different velocities) could not be avoided even at velocities more than 1 km s^{-1} away from the parent cloud velocity. Therefore, we developed cloud subtraction routines for the RM and the PTF technique as shown in Figures 17 and 18, respectively.

The upper left panel of Figure 17 shows the ^{12}CO integrated intensity map of the redshifted lobe of the HOPS 135 outflow, which clearly shows large-scale cloud emission. To avoid contamination from cloud emission in the estimation of outflow parameters using the RM, we first estimate the averaged background per pixel inside the ring mask, but outside the outflow mask (as shown in the upper right panel of Figure 17). For tracers with cloud contamination, we subtracted the background cloud spectrum from the outflow spectrum, as shown in the lower panels of Figure 17. We then use the background-subtracted data to construct the mass spectrum inside the rings to estimate the molecular outflow rates.

As for the PFT technique, the mass spectrum is calculated for each individual pixel (instead of using rings). Hence, we adopted a slightly different method for the background subtraction as shown in Figure 18. We first obtained the averaged profile for the quantity of interest as a function of distance from the central protostar perpendicular to the outflow direction. To avoid subtracting outflow emission near the protostar, we set the background value in the inner region ($\leqslant$1050 au) to a constant as shown in Figure 18, the upper plot. We rotate the radial profile to create a 2D background map (see the lower middle panel of Figure 18). Then we subtracted out the background to get rid of the large-scale cloud emission (see the lower right panel of Figure 18).

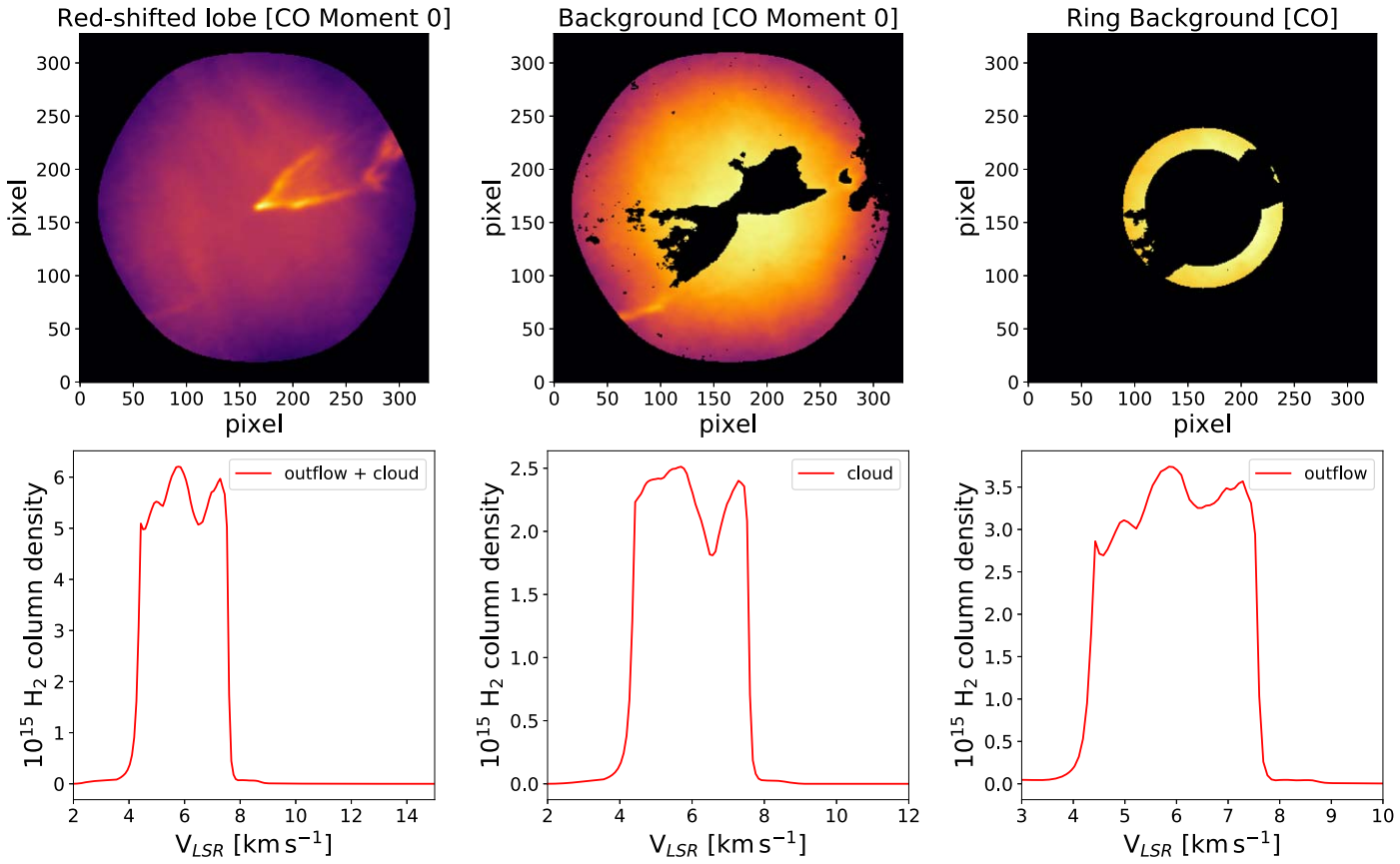

Figure 17. Subtraction of cloud emission using the RM for HOPS 135. The redshifted outflow lobe sits on top of the cloud shown in ^{12}CO momentum 0 (upper left panel). We measure the background emission in a ring outside the outflow mask as shown in the upper right panel. For each of the rings at different distances from the source, we measured its corresponding background. For tracers with cloud contamination, we subtracted the background cloud spectrum from the spectrum obtained over the area covered by the outflow (lobe) mask, as shown in the bottom three panels. In the bottom right panel, the "outflow" label represents the background-subtracted column density spectrum.

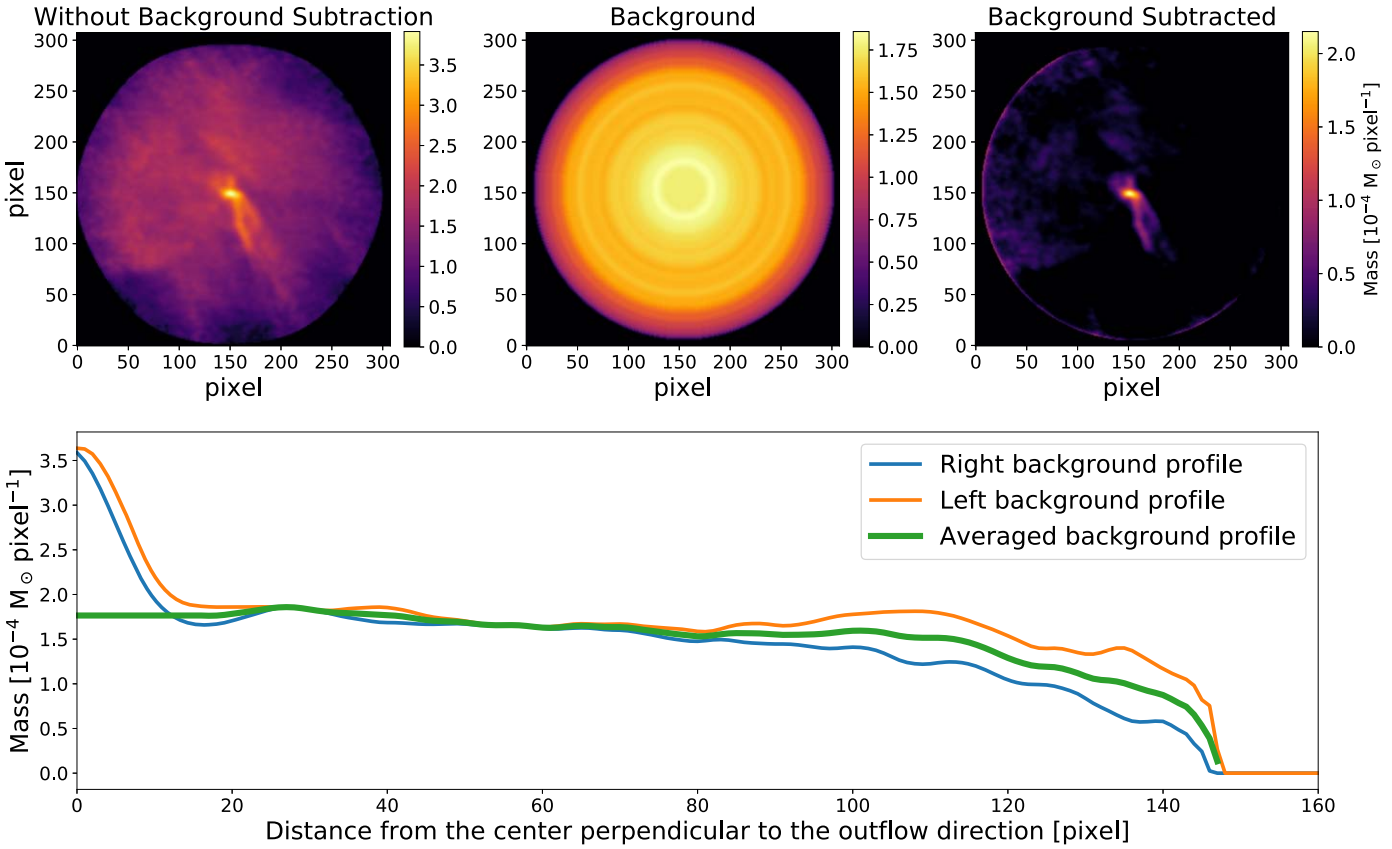

Figure 18. Cloud subtraction method for the PFT technique. In this example, we show (in the upper left panel) the uncorrected outflow mass map for HOPS 10, This clearly shows background cloud emission not associated with the outflow. We measure the background emission as a function of distance from the central protostar (perpendicular to the outflow direction), as shown in the upper panel. The orange and blue lines represent the left side and the right side of the background emission profile from the protostar. We set the central region ($\leqslant$1050 au) of the profile to constant to avoid subtracting outflow emission near the protostar. We used the radial profile to generate a two-dimensional background map (upper middle panel). We then subtract the background map to remove the cloud contamination, resulting in the background-subtracted map (upper right panel).

Appendix B
Outflow Inclination Properties and Wide-angle Wind Modeling

In this section, we compared the inclination angle derived from the wide-angle wind modeling to the inclination angle derived from the disk major-to-minor axis ratio. The inclination angles derived from both methods are shown in Table 5.

We obtain the outflow inclination angle by fitting a wide-angle wind model (Li & Shu 1996; Lee et al. 2000). The wide-angle wind model has been used by others to estimate the inclination angle (and other properties) of observed molecular outflows (e.g., Hirano et al. 2010; Arce et al. 2013; Yen et al. 2017). In this model, the entrained material can be described by a parabolic shell with an expansion velocity analogous to the Hubble law. Many of the outflows from Class I sources (and some from flat-spectrum sources) show parabolic-like cavities similar to those expected from the wide-angle wind model. On the other hand, this wide-angle wind model may not be appropriate for modeling molecular outflows from Class 0 sources, as they are typically very collimated, and show a jet-like morphology (especially at high velocities). However, some of these Class 0 outflows also exhibit wider outflow cavities at low velocities (e.g., HOPS 10, HOPS 198). Hence, modeling these outflow cavity walls with a wide-angle wind model can provide an estimate of the outflow inclination angle.

The wide-angle wind model of Lee et al. (2000) can be described by three independent parameters: c_0, v_0, and i. Considering z is the outflow direction, and R is the radial distance from the outflow center, then a cylindrical symmetric parabolic shell surface can be described by

$$z = c_0 R^2, \tag{B1}$$

and the corresponding velocity follows

$$v_z = v_0 z, \tag{B2}$$
$$v_r = v_0 r, \tag{B3}$$
$$v_\phi = 0. \tag{B4}$$

Figure 19 outlines the basic steps for fitting the wide-angle wind model to constrain the outflow inclination. We start with creating an outflow mask from the ^{12}CO integrated intensity (moment 0) map. The outflow mask is used to isolate the outflow from the surroundings

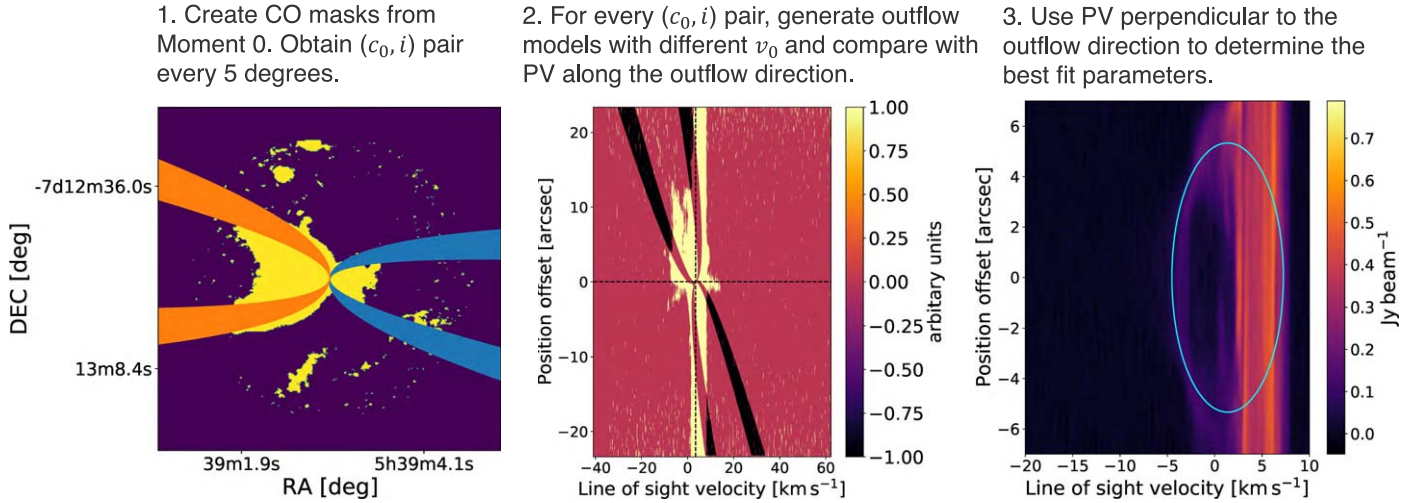

Figure 19. Method for constraining the outflow inclination angle by fitting a wide-angle wind model. The example shown here uses the outflow from HOPS 130.

Table 5
Outflow Inclination Angles

Source	Outflow Inclination from Wide-angle Wind Model Fit (deg)	Disk Major Axis (arcseconds)[a]	Disk Minor Axis (arcseconds)[a]	Disk Minor-to-Major Axis Ratio	Outflow Inclination Derived from Disk (deg)
HOPS 10	40	0.″14	0.″07	0.50	60
HOPS 11	45	0.″13	0.″12	0.92	23
HOPS 13	50	0.″19	0.″09	0.47	62
HOPS 127	25	0.″05	0.″03	0.60	53
HOPS 129	20	0.″10	0.″06	0.60	53
HOPS 130	25	0.″46	0.″15	0.33	71
HOPS 134	45	0.″06	0.″05	0.83	34
HOPS 135	35	0.″11	0.″06	0.55	57
HOPS 150B	25	0.″03	0.″07	0.78	39
HOPS 157	20	0.″53	0.″46	0.87	30
HOPS 164	55 (blue)/25 (red)	0.″22	0.″14	0.64	50
HOPS 166	20	0.″16	0.″15	0.94	20
HOPS 169	70	0.″17	0.″13	0.77	40
HOPS 177	30	0.″19	0.″03	0.16	81[c]
HOPS 185	30[b]	0.″27	0.″10	0.37	68
HOPS 191	30	0.″05	0.″02	0.41	66
HOPS 194	20	0.″19	0.″17	0.89	27
HOPS 198	25[b]	0.″41	0.″07	0.17	80
HOPS 200	NA	0.″46	0.″16	0.35	70
HOPS 355	45	0.″08	0.″07	0.88	29
HOPS 408	70	0.″28	0.″24	0.88	59

Notes.
[a] Deconvolved sizes from ALMA 0.87 mm continuum data published by Tobin et al. (2020).
[b] Suspicious results. The derived inclination angle is very different compared to the expected value from the molecular outflow morphology (Figure 2).
[c] As described in 4.1.4, we believe this estimate of the inclination angle is wrong because the continuum image for this source has a poor S/N. We instead use the mean inclination angle from a random uniform distribution of outflow orientations on the sky (57.°3) for this source.

and fit the outflow lobe morphology to the model. Then we applied the wide-angle wind model to constrain the pair solutions for c_0 and i for each lobe (redshifted and blueshifted lobes). The parabola should fit the edge of the outflow mask. For every 5° of inclination angle, from 0° to 180°, we search for the best solutions for c_0. In total, we obtained 36 pairs of solutions (for parameters c_0 and i).

Then for each pair of c_0 and i solution, we run different wide-angle wind models with a different characteristic velocity (v_0) using 0.3, 0.5, 1.0, 1.5, 2.0, 2.5, 3.0, 3.5, 4.0, 4.5, 5.0, 5.5, and 6.0 km s^{-1}. In total, we produced 468 models to compare with the ^{12}CO PV diagram along the outflow axis. The central panel in Figure 19 shows the residual plot with red (value of 1) representing the data, and blue (value of −1) representing the wide-angle wind model. We eliminate solutions with large residuals in the PV diagram. After reducing the number of solutions, we used the remaining solutions (with parameters c_0, i, and v_0) to compare with the PV perpendicular to the outflow. For the wide-angle wind model, the PV diagram perpendicular to the outflow axis is an ellipse. By matching the ellipse with the observational data, we can constrain the inclination angle of the outflow axis (with respect to the line of

Table 6
Parameters for the Best Outflow Wide-angle Wind Model for Each Source

Source	i (deg)	c_0[a] (10^{-4} au^{-1})	v_0[b] (10^{-4} km s^{-1})
HOPS 10	40	40.3 (blue)/ 10.8 (red)	37.5
HOPS 11	45	6.2	12.5
HOPS 13	50	25.0[c]	7.5
HOPS 127	25	13.9 (blue)/ 10.4 (red)	25.0
HOPS 129	20	4.3 (blue)/ 8.6 (red)	12.5 (blue)/ 7.5 (red)
HOPS 130	25	7.0 (blue)/ 10.4 (red)	12.5
HOPS 134	45	4.2	12.5
HOPS 135	35	12.8	12.5
HOPS 150B	25	52.2[c]	7.5
HOPS 157	20	64.5	37.5
HOPS 164	55 (blue)/ 25 (red)	45.2 (blue)/ 80.0 (red)	25.0 (blue)/ 7.5 (red)
HOPS 166	20	4.3	7.5
HOPS 169	70	40.7	12.5
HOPS 177	30	5.9	7.5
HOPS 185	30[d]	5.9 (blue)/ 8.8 (red)	25.0
HOPS 191	30	8.8 (blue)/ 5.9 (red)	12.5
HOPS 194	20	4.3	12.5 (blue)/ 7.5 (red)
HOPS 198	25[d]	10.4 (blue)/ 45.2 (red)	25.0
HOPS 200	NA	NA	NA
HOPS 355	45	27.0	12.5
HOPS 408	70	20.3	25.0

Notes.
[a] The uncertainty for c_0 is $0.74/\sin(i) \times 10^{-4}$ au^{-1}.
[b] The values are either 7.5, 12.5, 25.0, or 37.5 10^{-4} km s^{-1} because these are the values for the grid parameter search. The uncertainty for v_0 is half the interval between the values evaluated by the model. For 7.5×0^{-4} km s^{-1}, the uncertainty is $\pm 3.8 \times 10^{-4}$ km s^{-1}, for all other values the uncertainty is $\pm 6.3 \times 10^{-4}$ km s^{-1}.
[c] Unreliable results, poorly constrained.
[d] Suspicious results. The derived inclination angle is very different compared to the expected value from the molecular outflow morphology (Figure 2).

sight) as shown for HOPS 130 in Figure 19. The resulting estimated inclinations are shown in Table 5 with 0° being pole-on and 90° being an edge-on system. The parameters for the best wide-angle wind model for each source are shown in Table 6. Note that we divide the c_0 and v_0 by the source distance of 400 pc to convert the values in the unit of au instead of arcseconds.

In Figure 20 we plot the distribution of the difference in inclination values derived using two different methods: the outflow wide-angle wind fitting method and the disk continuum method. For the disk continuum method, the inclination angle can be derived by using the disk major-to-minor axis ratio and assuming the protostellar outflows are perpendicular to the disk plane. While there is a large dispersion in Figure 20, the distribution peaks at $10 \sim 20°$ and shows that in general both methods are consistent with each other. For the vast majority of sources, the estimated i from the two methods are different within 35°, and only three sources (i.e., 14% of the sample) show differences in the estimate of i of 45° or more. The small difference between the two methods might be partially explained by the assumption of a thin disk for the disk minor-to-major axis ratio method. Due to the disk thickness, the method cannot fully recover edge-on disk systems (small outflow inclination angles). Even so, the inclination angle derived from the high-resolution disk continuum is a likely more accurate estimate than that derived using the wide-angle wind model because it involves significantly fewer assumptions. Moreover, it is likely that not all molecular outflows are entrained by a wide-angle wind (the main assumptions when using the wide-angle wind model). In particular, many of our Class 0 outflows are jet-like and deviate from the parabolic shell structure expected in outflows driven by the wide-angle winds.

We also compare our results to the disk inclination angle derived through the modeling of the SED of protostars by Furlan et al. (2016). We find that the distribution of the derived inclination angle difference is completely random. This strongly suggests that the disk inclination angle from SED modeling is not reliable, and should not be used in determining disk and outflow inclination angles. Alternatively, machine-learning approaches may be used to predict both the plane-of-sky orientation and line-of-sight outflow inclination from CO spectral data (Xu et al. 2022b).

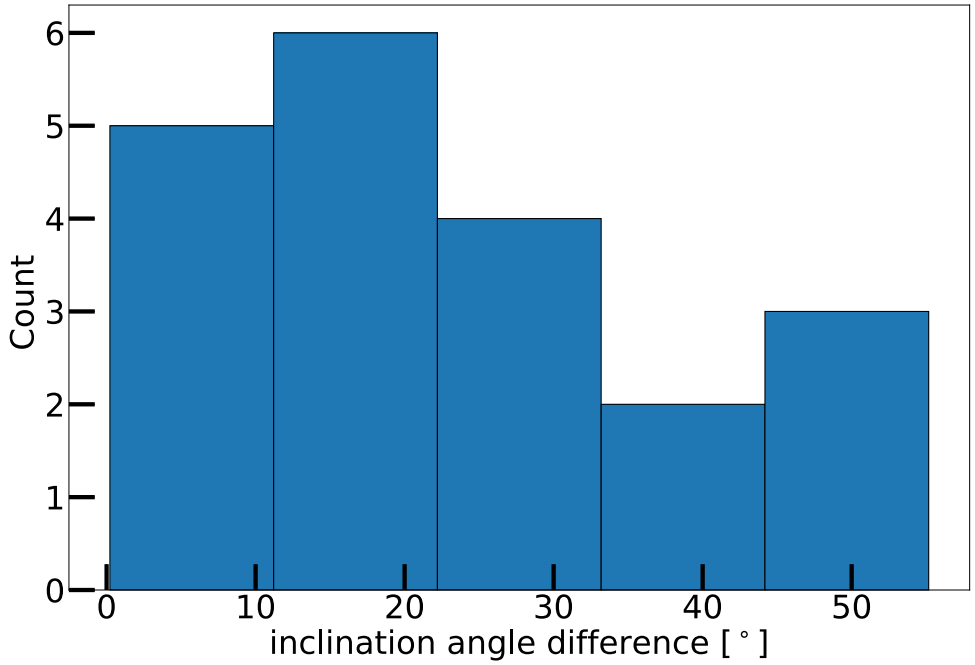

Figure 20. Histogram of inclination angle differences between those derived from the wide-angle wind model fit to the inclinations derived from the disk minor-to-major axis ratio.

Appendix C
Molecular Outflow Mass, Momentum, and Energy Velocity Range Information

In this section, we show the velocity range used for constructing the molecular outflow mass, momentum, and energy spectrum. An example of an outflow mass spectrum constructed from CO, ^{13}CO, and C^{18}O is shown in Figure 5. The velocity range used for constructing the molecular outmass, momentum, and energy spectrum are shown in Table 7.

Table 7
Velocity Ranges for Constructing Outflow Mass, Momentum, and Energy Spectra

Source	Blueshifted			Redshifted		
	^{12}CO (km s^{-1})	^{13}CO (km s^{-1})	C^{18}O (km s^{-1})	C^{18}O (km s^{-1})	^{13}CO (km s^{-1})	^{12}CO (km s^{-1})
HOPS 10	$v \leqslant 7.52$	$7.52 \leqslant v \leqslant 7.76$	NA	NA	$9.58 \leqslant v \leqslant 9.74$	$9.74 \leqslant v$
HOPS 11	$v \leqslant 5.88$	$5.88 \leqslant v \leqslant 6.68$	$6.68 \leqslant v \leqslant 7.10$	$8.50 \leqslant v \leqslant 10.33$	$10.33 \leqslant v \leqslant 11.12$	$11.12 \leqslant v$
HOPS 13	$v \leqslant 5.02$	$5.02 \leqslant v \leqslant 5.58$	$5.58 \leqslant v \leqslant 5.66$	NA	NA	NA
HOPS 127	$v \leqslant 3.27$	$3.27 \leqslant v \leqslant 3.75$	NA	$5.02 \leqslant v \leqslant 5.65$	$5.65 \leqslant v \leqslant 6.84$	$6.84 \leqslant v$
HOPS 129	$v \leqslant 2.52$ $2.92 \leqslant v \leqslant 3.07$	$2.52 \leqslant v \leqslant 2.84$	$2.84 \leqslant v \leqslant 2.92$	NA	NA	NA
HOPS 130	$v \leqslant 2.45$	NA	NA	NA	NA	NA
HOPS 134	NA	NA	NA	NA	$6.93 \leqslant v \leqslant 7.80$	$7.80 \leqslant v$
HOPS 135	$v \leqslant 3.20$	$3.20 \leqslant v \leqslant 3.68$	$3.68 \leqslant v \leqslant 4.39$	$4.95 \leqslant v \leqslant 5.20$	$5.20 \leqslant v \leqslant 6.30$	$6.30 \leqslant v$
HOPS 150	$v \leqslant 3.28$	$3.28 \leqslant v \leqslant 3.62$	$3.62 \leqslant v \leqslant 3.68$	NA	NA	NA
HOPS 157	$v \leqslant 3.64$	$4.64 \leqslant v \leqslant 4.75$	NA	NA	$6.64 \leqslant v \leqslant 9.28$	$9.28 \leqslant v$
HOPS 164	$v \leqslant 4.61$	$4.61 \leqslant v \leqslant 4.92$	$4.92 \leqslant v \leqslant 5.09$	NA	$6.58 \leqslant v \leqslant 6.83$	$6.83 \leqslant v$
HOPS 166	$v \leqslant 5.85$	NA	NA	NA	$10.05 \leqslant v \leqslant 12.05$	$12.05 \leqslant v$
HOPS 169	$v \leqslant 2.95$	$2.95 \leqslant v \leqslant 5.96$	$5.96 \leqslant v \leqslant 6.67$	$7.47 \leqslant v \leqslant 8.42$	$9.58 \leqslant v \leqslant 9.62$	$9.62 \leqslant v$
HOPS 177	$v \leqslant 6.78$	$6.78 \leqslant v \leqslant 8.37$	NA	NA	$9, 40 \leqslant v \leqslant 9.96$	$9.96 \leqslant v$
HOPS 185	$v \leqslant 6.38$	$6.38 \leqslant v \leqslant 6.61$	$6.61 \leqslant v \leqslant 6.94$	NA	NA	$9.87 \leqslant v$
HOPS 191	$v \leqslant 7.64$	NA	NA	NA	NA	$10.5 \leqslant v$
HOPS 194	NA	NA	NA	NA	NA	$9.85 \leqslant v$
HOPS 198	$v \leqslant 4.72$	$4.72 \leqslant v \leqslant 4.79$	$4.79 \leqslant v \leqslant 4.88$	NA	NA	$5.99 \leqslant v \leqslant 6.54$ $10.51 \leqslant v$
HOPS 200	$v \leqslant 6.59$	$6.59 \leqslant v \leqslant 6.66$	$6.66 \leqslant v \leqslant 7.75$	NA	NA	NA
HOPS 355	$v \leqslant 4.89$	$6.05 \leqslant v \leqslant 6.14$	$6.14 \leqslant v \leqslant 6.40$	NA	NA	$10.05 \leqslant v$
HOPS 408	$v \leqslant 2.38$	$2.38 \leqslant v \leqslant 2.83$	NA	$4.21 \leqslant v \leqslant 6.15$	$6.15 \leqslant v \leqslant 6.90$	$6.90 \leqslant v$

Appendix D
Summary of the Sources Excluded for Each Analysis

In this section, we summarize the sources excluded for each analysis and give explanations. The results are summarized in Table 8.

Table 8
Sources Excluded in Each Analysis

Main Analysis	Item Analyzed	Table/ Figure	Sources Excluded	Reason
Mass, momentum, energy rates	Radial profile	Figure 9	HOPS 408	Outflow is barely resolved.
			HOPS 166, HOPS 194	Significantly higher bolometric luminosity and core mass compared to other sources.
	Class average	Figure 14, Tables 3, 4	HOPS 408	Outflow is barely resolved.
			HOPS 166, HOPS 194	Significantly higher bolometric luminosity and core mass compared to other sources.
Angular profile	Outflow momentum angular profile	Figure 13	HOPS 11 blueshifted lobe	Outflow lobe is strongly asymmetric.
			HOPS 13, HOPS 200	Very messy outflow.
			HOPS 134 blueshifted lobe	No detection.
			HOPS 135 blueshifted lobe	Low S/N.
			HOPS 177 redshifted lobe	Low S/N.
	Outflow energy angular profile	Figure 13	HOPS 11 blueshifted lobe	Outflow lobe is strongly asymmetric.
			HOPS 13, HOPS 200	Very messy outflow.
			HOPS 130 redshifted lobe	Compact emission, hard to separate out.
			HOPS 134 blueshifted lobe	No detection.
			HOPS 135 blueshifted lobe	Low S/N.
			HOPS 150	Contaminated by nearby source.
			HOPS 157 redshifted lobe	Compact emission, hard to separate out.
			HOPS 177 redshifted lobe	Low S/N.
			HOPS 191 redshifted lobe	Low S/N.
			HOPS 194	Low S/N.
Opening angle	Conventional opening angle	Figure 11	HOPS 408	Outflow is barely resolved.
			HOPS 150, HOPS 166	Opening angle is ill-defined.
			HOPS 194	Poor Gaussian fits to the ^{12}CO data. Outflow opening angle measured from C^{18}O moment 0 map by eye.
	Momentum opening angle	Figure 12	HOPS 13, HOPS 134, HOPS 157, HOPS 166, HOPS 177, HOPS 194, HOPS 200	Poor Gaussian fits to the momentum maps.
	Energy opening angle	Figure 12	HOPS 13, HOPS 134, HOPS 157, HOPS 191, HOPS 194, HOPS 200	Poor Gaussian fits to the energy maps.
			HOPS 150	Contaminated by nearby source.
	Outflow curvature	Figure 15	HOPS 13, HOPS 150, HOPS 200	Poorly constrained.

Appendix E
Molecular Outflow Rates

In this section, we report all the measurements of outflow mass ($\dot{M}$), momentum ($\dot{P}$), and energy ($\dot{E}$) ejection rate for both the redshifted (R) and blueshifted (B) lobes at different radii. We present the outflow rate using all outflow gas in Tables 9–11. For gas with escape velocity $v_{\rm out} > 1$ km s^{-1}, the outflow rates are reported in Tables 12–14. Similarly, for gas with escape velocity $v_{\rm out} > 2$ km s^{-1}, the outflow rates are reported in Tables 15–17.

Table 9
Molecular Outflow Rates Using All Outflow Gas, within 2380∼3740 au and 3749∼5100 au Away from the Source

	2380∼3740 au						3740∼5100 au					
Source	$\dot{M}_B$ [a]	$\dot{M}_R$ [a]	$\dot{P}_R$ [b]	$\dot{P}_B$ [b]	$\dot{E}_R$ [c]	$\dot{E}_B$ [c]	$\dot{M}_B$ [a]	$\dot{M}_R$ [a]	$\dot{P}_R$ [b]	$\dot{P}_B$ [b]	$\dot{E}_R$ [c]	$\dot{E}_B$ [c]
HOPS 10	1.46	3.11	5.14	71.73	5.78E+41	4.75E+43	1.79	2.93	10.54	68.68	1.79E+42	4.94E+43
HOPS 10 no jet	1.46	2.67	5.14	30.38	5.78E+41	8.30E+42	1.79	2.48	10.54	25.07	1.79E+42	6.49E+42
HOPS 11	1.70	4.30	7.66	26.69	8.19E+41	4.08E+42	2.29	5.43	11.06	39.39	1.24E+42	7.64E+42
HOPS 11 no jet	1.62	3.94	5.73	17.14	3.58E+41	1.51E+42	2.04	4.99	6.51	24.93	3.52E+41	2.74E+42
HOPS 164	1.76	2.95	10.23	20.82	2.61E+42	1.00E+43	1.34	3.17	9.01	28.17	2.78E+42	1.44E+43
HOPS 164 no jet	1.63	2.75	5.01	8.18	2.22E+41	6.44E+41	1.22	2.81	3.90	7.49	1.87E+41	4.58E+41
HOPS 169	3.79	2.30	24.99	15.18	3.09E+42	2.02E+42	3.11	2.13	17.75	18.24	1.82E+42	2.44E+42
HOPS 198	0.46	3.01	5.31	22.22	8.27E+41	4.62E+42	0.31	1.56	3.85	28.58	6.08E+41	1.25E+43
HOPS 355	0.22	0.05	0.50	0.36	2.13E+40	2.76E+40	0.17	0.06	0.43	0.46	2.16E+40	3.87E+40
HOPS 408	NA	NA	NA	NA	NA	NA	NA	NA	NA	NA	NA	NA
HOPS 127	0.34	2.37	2.39	6.59	2.81E+41	2.62E+41	0.23	2.42	1.47	6.82	1.55E+41	3.25E+41
HOPS 130	0.71	NA	10.02	NA	1.76E+42	NA	0.48	NA	6.70	NA	1.21E+42	NA
HOP 135	0.19	13.37	0.39	43.09	1.99E+40	1.67E+42	0.19	11.52	0.28	36.11	1.14E+40	1.38E+42
HOPS 157	0.93	NA	2.76	NA	1.93E+41	NA	1.27	NA	4.02	NA	3.38E+41	NA
HOPS 177	7.12	0.74	20.14	1.05	6.43E+41	1.92E+40	5.77	0.79	16.98	1.28	5.68E+41	3.01E+40
HOPS 185	8.28	0.12	30.95	0.85	2.05E+42	6.29E+40	4.62	0.16	16.25	1.14	6.85E+41	8.25E+40
HOPS 191	0.61	0.06	2.55	0.60	1.47E+41	7.33E+40	0.83	0.02	3.93	0.21	2.62E+41	2.02E+40
HOPS 129	0.90	0.04	1.08	0.02	1.58E+40	1.63E+38	0.70	0.04	0.97	0.03	1.80E+40	1.87E+38
HOPS 134	NA	0.39	NA	1.71	NA	1.32E+41	NA	0.29	NA	0.94	NA	6.31E+40
HOPS 13	1.69	NA	6.34	NA	3.58E+41	NA	1.81	NA	7.98	NA	5.20E+41	NA
HOPS 150	0.31	NA	0.28	NA	6.68E+39	NA	0.15	NA	0.23	NA	6.97E+39	NA
HOPS 166	0.24	2.51	1.36	8.02	9.98E+40	3.93E+41	0.36	1.74	1.78	6.63	9.81E+40	3.90E+41
HOPS 194	NA	0.16	NA	0.50	NA	1.94E+40	NA	0.17	NA	0.50	NA	1.68E+40
HOPS 200	NA	NA	NA	NA	NA	NA	NA	NA	NA	NA	NA	NA

Notes.
[a] In units of $M_\odot$ Myr^{-1}.
[b] In units of $M_\odot$ km s^{-1} Myr^{-1}.
[c] In units of erg Myr^{-1}.

Table 10
Molecular Outflow Rates Using All Outflow Gas, within 5100∼6460 au and 6460∼7820 au Away from the Source

	5100∼6460 au						6460∼7820 au					
Source	$\dot{M}_B$ [a]	$\dot{M}_R$ [a]	$\dot{P}_R$ [b]	$\dot{P}_B$ [b]	$\dot{E}_R$ [c]	$\dot{E}_B$ [c]	$\dot{M}_B$ [a]	$\dot{M}_R$ [a]	$\dot{P}_R$ [b]	$\dot{P}_B$ [b]	$\dot{E}_R$ [c]	$\dot{E}_B$ [c]
HOPS 10	1.96	3.00	14.87	78.66	3.34E+42	6.40E+43	1.77	2.82	13.43	95.12	3.63E+42	7.86E+43
HOPS 10 no jet	1.96	2.41	14.87	19.39	3.34E+42	3.86E+42	1.77	2.08	13.43	20.96	3.63E+42	4.12E+42
HOPS 11	2.24	4.95	10.04	36.55	1.01E+42	6.73E+42	2.05	3.73	7.74	28.12	5.51E+41	4.85E+42
HOPS 11 no jet	2.05	4.76	6.63	29.34	3.59E+41	3.86E+42	2.05	3.22	7.74	15.31	5.51E+41	1.27E+42
HOPS 164	0.50	3.22	5.61	29.14	2.58E+42	1.72E+43	NA	2.28	0.02	20.79	4.92E+39	1.29E+43
HOPS 164 no jet	0.40	2.85	1.07	6.55	3.46E+40	1.93E+41	NA	2.03	0.01	4.88	2.28E+38	1.57E+41
HOPS 169	2.54	1.71	16.10	16.66	1.73E+42	2.28E+42	1.48	1.52	10.20	14.62	1.02E+42	1.74E+42
HOPS 198	0.15	1.24	1.50	16.93	1.87E+41	6.50E+42	0.09	0.33	0.74	2.05	7.41E+40	2.85E+41
HOPS 355	0.14	0.05	0.36	0.41	1.54E+40	3.67E+40	0.15	0.04	0.42	0.31	1.65E+40	2.64E+40
HOPS 408	NA	NA	NA	NA	NA	NA	NA	NA	NA	NA	NA	NA
HOPS 127	0.10	2.35	0.42	6.76	2.91E+40	4.17E+41	0.05	2.23	0.19	5.55	1.01E+40	1.97E+41
HOPS 130	0.21	NA	2.35	NA	3.59E+41	NA	0.10	NA	0.76	NA	8.06E+40	NA
HOP 135	0.11	2.35	0.12	7.21	2.86E+39	2.73E+41	NA	NA	NA	NA	NA	NA
HOPS 157	0.31	NA	0.45	NA	9.73E+39	NA	NA	NA	NA	NA	NA	NA
HOPS 177	5.31	1.03	16.03	1.67	5.65E+41	4.12E+40	3.88	1.25	11.95	1.96	4.45E+41	4.99E+40
HOPS 185	5.30	0.18	19.20	1.25	8.30E+41	8.84E+40	5.18	0.06	18.55	0.42	7.12E+41	3.36E+40

Table 10
(Continued)

Source	5100∼6460 au						6460∼7820 au					
	$\dot{M}_B$ [a]	$\dot{M}_R$ [a]	$\dot{P}_R$ [b]	$\dot{P}_B$ [b]	$\dot{E}_R$ [c]	$\dot{E}_B$ [c]	$\dot{M}_B$ [a]	$\dot{M}_R$ [a]	$\dot{P}_R$ [b]	$\dot{P}_B$ [b]	$\dot{E}_R$ [c]	$\dot{E}_B$ [c]
HOPS 191	0.80	0.01	4.45	0.13	3.53E+41	1.17E+40	0.36	0.01	1.50	0.05	9.17E+40	4.47E+39
HOPS 129	0.37	0.04	0.55	0.03	1.14E+40	1.88E+38	0.25	0.02	0.40	0.01	9.21E+39	8.83E+37
HOPS 134	NA	0.19	NA	0.37	NA	7.63E+39	NA	0.10	NA	0.22	NA	5.16E+39
HOPS 13	0.18	NA	0.74	NA	3.95E+40	NA	NA	NA	NA	NA	NA	NA
HOPS 150	0.05	NA	0.03	NA	2.70E+38	NA	0.06	NA	0.07	NA	1.66E+39	NA
HOPS 166	0.33	1.46	1.62	5.62	8.71E+40	3.35E+41	0.32	0.76	1.64	2.89	8.96E+40	1.61E+41
HOPS 194	NA	0.13	NA	0.37	NA	1.13E+40	NA	0.10	NA	0.28	NA	8.95E+39
HOPS 200	NA	NA	NA	NA	NA	NA	NA	NA	NA	NA	NA	NA

Notes.
[a] In units of $M_\odot$ Myr^{-1}.
[b] In units of $M_\odot$ km s^{-1} Myr^{-1}.
[c] In units of erg Myr^{-1}.

Table 11
Molecular Outflow Rates Using All Outflow Gas, within 7820∼9180 au Away from the Source

Source	7820∼9180 au					
	$\dot{M}_B$ [a]	$\dot{M}_R$ [a]	$\dot{P}_R$ [b]	$\dot{P}_B$ [b]	$\dot{E}_R$ [c]	$\dot{E}_B$ [c]
HOPS 10	0.79	1.90	4.05	76.61	5.59E+41	6.43E+43
HOPS 10 no jet	0.79	1.29	4.05	15.65	5.59E+41	3.03E+42
HOPS 11	1.63	2.30	6.90	21.40	4.60E+41	3.63E+42
HOPS 11 no jet	1.63	1.32	6.90	4.48	4.60E+41	1.88E+41
HOPS 164	NA	1.77	NA	19.95	NA	1.41E+43
HOPS 164 no jet	NA	1.55	NA	3.89	NA	1.46E+41
HOPS 169	1.09	1.38	8.87	11.86	8.80E+41	1.22E+42
HOPS 198	0.10	NA	0.88	NA	9.77E+40	NA
HOPS 355	0.13	0.03	0.34	0.19	1.31E+40	1.22E+40
HOPS 408	NA	NA	NA	NA	NA	NA
HOPS 127	0.10	2.00	0.33	5.47	1.73E+40	2.04E+41
HOPS 130	NA	NA	NA	NA	NA	NA
HOP 135	NA	NA	NA	NA	NA	NA
HOPS 157	NA	NA	NA	NA	NA	NA
HOPS 177	1.31	1.14	4.13	1.76	1.61E+41	4.43E+40
HOPS 185	NA	NA	NA	NA	NA	NA
HOPS 191	NA	NA	NA	NA	NA	NA
HOPS 129	0.13	NA	0.28	NA	8.94E+39	4.91E+35
HOPS 134	NA	0.08	NA	0.16	NA	4.10E+39
HOPS 13	NA	NA	NA	NA	NA	NA
HOPS 150	0.06	NA	0.08	NA	1.88E+39	NA
HOPS 166	0.14	0.49	0.66	2.35	3.31E+40	1.58E+41
HOPS 194	NA	0.05	NA	0.13	NA	4.10E+39
HOPS 200	NA	NA	NA	NA	NA	NA

Notes.
[a] In units of $M_\odot$ Myr^{-1}.
[b] In units of $M_\odot$ km s^{-1} Myr^{-1}.
[c] In units of erg Myr^{-1}.

Table 12
Molecular Outflow Rates for Gas with $v_{out} > 1$ km s^{-1}, within 2380–3740 au and 3749–5100 au Away from the Source

Source	2380∼3740 au						3740∼5100 au					
	$\dot{M}_B$ [a]	$\dot{M}_R$ [a]	$\dot{P}_R$ [b]	$\dot{P}_B$ [b]	$\dot{E}_R$ [c]	$\dot{E}_B$ [c]	$\dot{M}_B$ [a]	$\dot{M}_R$ [a]	$\dot{P}_R$ [b]	$\dot{P}_B$ [b]	$\dot{E}_R$ [c]	$\dot{E}_B$ [c]
HOPS 10	1.13	3.11	4.93	72.53	6.46e+41	4.86E+43	1.43E+00	2.93	10.44	69.29	1.95E+42	5.02E+43
HOPS 10 no jet	1.13	3.11	4.93	72.53	6.46e+41	4.86E+43	1.43E+00	2.93	10.44	69.29	1.95E+42	5.02E+43
HOPS 11	1.49	4.03	7.51	26.96	8.32e+41	4.42E+42	2.02E+00	5.19	10.93	39.85	1.29E+42	8.11E+42
HOPS 11 no jet	1.49	4.03	7.51	26.96	8.32e+41	4.42E+42	2.02E+00	5.19	10.93	39.85	1.29E+42	8.11E+42
HOPS 164	1.76	2.95	10.23	20.82	2.61e+42	1.00E+43	1.34E+00	3.17	9.01	28.17	2.78E+42	1.44E+43

Table 12
(Continued)

Source	2380∼3740 au						3740∼5100 au					
	$\dot{M}_B$ [a]	$\dot{M}_R$ [a]	$\dot{P}_R$ [b]	$\dot{P}_B$ [b]	$\dot{E}_R$ [c]	$\dot{E}_B$ [c]	$\dot{M}_B$ [a]	$\dot{M}_R$ [a]	$\dot{P}_R$ [b]	$\dot{P}_B$ [b]	$\dot{E}_R$ [c]	$\dot{E}_B$ [c]
HOPS 164 no jet	1.76	2.95	10.23	20.82	2.61e+42	1.00E+43	1.34E+00	3.17	9.01	28.17	2.78E+42	1.44E+43
HOPS 169	3.35	1.83	24.73	14.95	3.11e+42	2.07E+42	2.59E+00	1.67	17.43	18.02	1.84E+42	2.49E+42
HOPS 198	0.50	3.04	8.71	30.68	5.6e+42	2.53E+43	3.88E-01	1.59	9.90	33.63	7.09E+42	2.28E+43
HOPS 355	0.13	0.05	0.49	0.41	3.15e+40	4.95E+40	1.03E-01	0.06	0.42	0.55	2.82E+40	8.30E+40
HOPS 408	NA	NA	NA	NA	0	NA	NA	NA	NA	NA	NA	NA
HOPS 127	0.35	2.05	2.50	6.53	3.31e+41	3.49E+41	2.29E-01	2.14	1.62	6.78	2.21E+41	4.12E+41
HOPS 130	0.71	NA	10.76	NA	2.42e+42	NA	4.90E-01	NA	7.45	NA	1.83E+42	NA
HOP 135	0.09	12.89	0.44	43.14	8.42e+40	1.99E+42	6.40E-02	10.97	0.28	35.97	5.82E+40	1.57E+42
HOPS 157	0.59	NA	2.54	NA	2.12e+41	NA	8.42E-01	NA	3.74	NA	3.62E+41	NA
HOPS 177	7.13	0.55	20.51	1.42	8.64e+41	4.20E+41	5.78E+00	0.60	17.38	1.67	8.22E+41	4.34E+41
HOPS 185	8.28	0.13	31.43	2.27	2.48e+42	1.61E+42	4.62E+00	0.18	16.68	3.21	1.08E+42	2.33E+42
HOPS 191	0.63	0.07	3.61	1.47	9.73e+41	9.09E+41	8.54E-01	0.03	5.34	0.48	1.37E+42	2.75E+41
HOPS 129	0.55	NA	0.93	NA	7.78e+40	NA	4.82E-01	NA	0.97	NA	9.78E+40	NA
HOPS 134	NA	0.40	NA	2.22	0	3.53E+41	NA	0.30	NA	1.43	NA	2.92E+41
HOPS 13	1.68	NA	6.33	NA	3.58e+41	NA	1.82E+00	NA	8.13	NA	5.59E+41	NA
HOPS 150	0.08	NA	0.51	NA	1.44e+41	NA	7.36E-02	NA	0.51	NA	1.39E+41	NA
HOPS 166	0.25	2.52	1.46	8.17	1.33e+41	4.23E+41	3.64E-01	1.75	1.92	6.76	1.47E+41	4.16E+41
HOPS 194	NA	0.21	NA	1.82	0	4.41E+41	NA	0.22	NA	1.94	NA	4.73E+41
HOPS 200	NA	NA	NA	NA	0	NA	NA	NA	NA	NA	NA	NA

Notes.
[a] In units of $M_\odot$ Myr^{-1}.
[b] In units of $M_\odot$ km s^{-1} Myr^{-1}.
[c] In units of erg Myr^{-1}.

Table 13
Molecular Outflow Rates for Gas with $v_{out} > 1$ km s^{-1}, within 5100∼6460 au and 6460–7820 au Away from the Source

Source	5100∼6460 au						6460∼7820 au					
	$\dot{M}_B$ [a]	$\dot{M}_R$ [a]	$\dot{P}_R$ [b]	$\dot{P}_B$ [b]	$\dot{E}_R$ [c]	$\dot{E}_B$ [c]	$\dot{M}_B$ [a]	$\dot{M}_R$ [a]	$\dot{P}_R$ [b]	$\dot{P}_B$ [b]	$\dot{E}_R$ [c]	$\dot{E}_B$ [c]
HOPS 10	1.60	3.01	14.76	79.83	3.52E+42	6.55E+43	1.43	2.83	13.44	96.41	3.88E+42	8.03E+43
HOPS 10 no jet	1.60	3.01	14.76	79.83	3.52E+42	6.55E+43	1.43	2.83	13.44	96.41	3.88E+42	8.03E+43
HOPS 11	1.95	4.79	9.92	37.04	1.07E+42	7.18E+42	1.66	3.62	7.73	28.53	6.77E+41	5.21E+42
HOPS 11 no jet	1.95	4.79	9.92	37.04	1.07E+42	7.18E+42	1.66	3.62	7.73	28.53	6.77E+41	5.21E+42
HOPS 164	0.50	3.22	5.61	29.14	2.58E+42	1.72E+43	NA	2.28	0.02	20.79	4.92E+39	1.29E+43
HOPS 164 no jet	0.50	3.22	5.61	29.14	2.58E+42	1.72E+43	NA	2.28	0.02	20.79	4.92E+39	1.29E+43
HOPS 169	2.25	1.49	15.94	16.63	1.75E+42	2.35E+42	1.40	1.47	10.22	14.80	1.05E+42	1.86E+42
HOPS 198	0.16	1.28	3.38	21.88	3.17E+42	1.64E+43	0.09	0.34	1.82	3.32	1.97E+42	3.40E+42
HOPS 355	0.10	0.05	0.38	0.48	2.95E+40	6.94E+40	0.13	0.04	0.47	0.41	3.99E+40	6.89E+40
HOPS 408	NA	NA	NA	NA	NA	NA	NA	NA	NA	NA	NA	NA
HOPS 127	0.10	1.94	0.52	6.62	6.98E+40	5.03E+41	0.05	1.82	0.26	5.44	4.02E+40	2.90E+41
HOPS 130	0.22	NA	3.14	NA	1.04E+42	NA	0.11	NA	1.81	NA	9.79E+41	NA
HOP 135	0.03	2.22	0.09	7.23	1.61E+40	3.61E+41	NA	NA	NA	NA	NA	NA
HOPS 157	0.20	NA	0.39	NA	1.99E+40	NA	NA	NA	NA	NA	NA	NA
HOPS 177	5.31	0.78	16.46	2.00	8.29E+41	4.27E+41	3.89	0.94	12.30	2.51	6.50E+41	6.58E+41
HOPS 185	5.31	0.21	19.63	4.35	1.19E+42	3.43E+42	5.18	0.09	18.87	3.09	1.00E+42	2.95E+42
HOPS 191	0.82	0.02	5.53	0.49	1.19E+42	3.93E+41	0.37	0.01	2.27	0.16	6.96E+41	1.01E+41
HOPS 129	0.25	NA	0.57	NA	6.62E+40	NA	0.18	NA	0.54	NA	1.03E+41	NA
HOPS 134	NA	0.21	NA	0.84	NA	2.20E+41	NA	0.11	NA	0.55	NA	1.65E+41
HOPS 13	0.18	NA	0.74	NA	3.95E+40	NA	NA	NA	NA	NA	NA	NA
HOPS 150	0.04	NA	1.04	NA	4.03E+41	NA	0.02	NA	0.17	NA	5.09E+40	NA
HOPS 166	0.34	1.47	1.87	5.83	1.46E+41	3.75E+41	0.32	0.76	1.74	2.92	1.24E+41	1.68E+41
HOPS 194	NA	0.19	NA	1.92	NA	5.09E+41	NA	0.14	NA	1.59	NA	4.33E+41
HOPS 200	NA	NA	NA	NA	NA	NA	NA	NA	NA	NA	NA	NA

Notes.
[a] In units of $M_\odot$ Myr^{-1}.
[b] In units of $M_\odot$ km s^{-1} Myr^{-1}.
[c] In units of erg Myr^{-1}.

Table 14
Molecular Outflow Rates for Gas with $v_{out} > 1$ km s^{-1}, within 7820∼9180 au Away from the Source

	7820∼9180 au					
Source	$\dot{M}_B$ [a]	$\dot{M}_R$ [a]	$\dot{P}_R$ [b]	$\dot{P}_B$ [b]	$\dot{E}_R$ [c]	$\dot{E}_B$ [c]
HOPS 10	0.66	1.91	5.65	78.07	1.55E+42	6.62E+43
HOPS 10 no jet	0.66	1.91	5.65	78.07	1.55E+42	6.62E+43
HOPS 11	1.45	2.28	7.00	22.14	5.64E+41	4.13E+42
HOPS 11 no jet	1.45	2.28	7.00	22.14	5.64E+41	4.13E+42
HOPS 164	NA	1.77	NA	19.95	NA	1.41E+43
HOPS 164 no jet	NA	1.77	NA	19.95	NA	1.41E+43
HOPS 169	1.08	1.37	9.01	12.16	9.49E+41	1.40E+42
HOPS 198	0.11	NA	3.18	NA	4.21E+42	NA
HOPS 355	0.11	0.04	0.39	0.36	3.50E+40	9.02E+40
HOPS 408	NA	NA	NA	NA	NA	NA
HOPS 127	0.10	1.71	0.46	5.56	7.15E+40	3.61E+41
HOPS 130	NA	NA	NA	NA	NA	NA
HOP 135	NA	NA	NA	NA	NA	NA
HOPS 157	NA	NA	NA	NA	NA	NA
HOPS 177	1.31	0.86	4.35	2.48	2.93E+41	7.40E+41
HOPS 185	NA	NA	NA	NA	NA	NA
HOPS 191	NA	NA	NA	NA	NA	NA
HOPS 129	0.12	NA	0.36	NA	5.06E+40	NA
HOPS 134	NA	0.08	NA	0.54	NA	1.89E+41
HOPS 13	NA	NA	NA	NA	NA	NA
HOPS 150	0.03	NA	0.22	NA	6.30E+40	NA
HOPS 166	0.14	0.49	0.73	2.40	5.67E+40	1.68E+41
HOPS 194	NA	0.08	NA	1.08	NA	3.10E+41
HOPS 200	NA	NA	NA	NA	NA	NA

Notes.
[a] In units of $M_\odot$ Myr^{-1}.
[b] In units of $M_\odot$ km s^{-1} Myr^{-1}.
[c] In units of erg Myr^{-1}.

Table 15
Molecular Outflow Rates for Gas with $v_{out} > 2$ km s^{-1}, within 2380∼3740 au and 3749∼5100 au Away from the Source

	2380∼3740 au						3740∼5100 au					
Source	$\dot{M}_B$ [a]	$\dot{M}_R$ [a]	$\dot{P}_R$ [b]	$\dot{P}_B$ [b]	$\dot{E}_R$ [c]	$\dot{E}_B$ [c]	$\dot{M}_B$ [a]	$\dot{M}_R$ [a]	$\dot{P}_R$ [b]	$\dot{P}_B$ [b]	$\dot{E}_R$ [c]	$\dot{E}_B$ [c]
HOPS 10	0.39	3.11	4.02	72.53	6.35E+41	4.86E+43	0.67	2.93	9.52	69.29	1.94E+42	5.02E+43
HOPS 10 no jet	0.39	3.11	4.02	72.53	6.35E+41	4.86E+43	0.67	2.93	9.52	69.29	1.94E+42	5.02E+43
HOPS 11	1.00	3.18	6.78	25.76	8.21E+41	4.40E+42	1.35	4.25	9.94	38.55	1.27E+42	8.09E+42
HOPS 11 no jet	1.00	3.18	6.78	25.76	8.21E+41	4.40E+42	1.35	4.25	9.94	38.55	1.27E+42	8.09E+42
HOPS 164	1.13	1.56	9.26	18.50	2.59E+42	1.00E+43	0.95	1.70	8.39	25.75	2.77E+42	1.43E+43
HOPS 164 no jet	1.13	1.56	9.26	18.50	2.59E+42	1.00E+43	0.95	1.70	8.39	25.75	2.77E+42	1.43E+43
HOPS 169	2.77	1.25	23.87	14.08	3.09E+42	2.05E+42	2.26	1.58	16.94	17.86	1.83E+42	2.48E+42
HOPS 198	0.50	3.04	8.71	30.68	5.60E+42	2.53E+43	0.39	1.59	9.90	33.63	7.09E+42	2.28E+43
HOPS 355	0.13	0.05	0.49	0.41	3.15E+40	4.95E+40	0.10	0.06	0.42	0.55	2.82E+40	8.30E+40
HOPS 408	NA	NA	NA	NA	NA	NA	NA	NA	NA	NA	NA	NA
HOPS 127	0.26	1.42	2.36	5.59	3.29E+41	3.35E+41	0.17	1.33	1.52	5.58	2.20E+41	3.94E+41
HOPS 130	0.71	NA	10.76	NA	2.42E+42	NA	0.49	NA	7.45	NA	1.83E+42	NA
HOP 135	0.06	9.81	0.39	38.52	8.35E+40	1.92E+42	0.03	8.11	0.24	31.68	5.77E+40	1.51E+42
HOPS 157	0.33	NA	2.21	NA	2.08E+41	NA	0.39	NA	3.16	NA	3.54E+41	NA
HOPS 177	5.46	0.11	17.88	0.85	8.22E+41	4.13E+41	4.49	0.16	15.37	1.10	7.90E+41	4.26E+41
HOPS 185	7.79	0.13	30.51	2.27	2.47E+42	1.61E+42	4.45	0.18	16.35	3.21	1.07E+42	2.33E+42
HOPS 191	0.45	0.07	3.34	1.47	9.69E+41	9.09E+41	0.65	0.03	5.02	0.48	1.36E+42	2.75E+41
HOPS 129	0.08	NA	0.34	NA	7.03E+40	NA	0.12	NA	0.51	NA	9.19E+40	NA
HOPS 134	NA	0.22	NA	1.98	NA	3.50E+41	NA	0.12	NA	1.16	NA	2.88E+41
HOPS 13	1.56	NA	6.17	NA	3.55E+41	NA	1.76	NA	8.04	NA	5.58E+41	NA
HOPS 150	0.05	NA	0.46	NA	1.43E+41	NA	0.06	NA	0.48	NA	1.38E+41	NA
HOPS 166	0.25	1.73	1.46	6.85	1.33E+41	4.01E+41	0.36	1.20	1.92	5.86	1.47E+41	4.01E+41
HOPS 194	NA	0.16	NA	1.74	NA	4.39E+41	NA	0.18	NA	1.86	NA	4.72E+41
HOPS 200	NA	NA	NA	NA	NA	NA	NA	NA	NA	NA	NA	NA

Notes.
[a] In units of $M_\odot$ Myr^{-1}.
[b] In units of $M_\odot$ km s^{-1} Myr^{-1}.
[c] In units of erg Myr^{-1}.

Table 16
Molecular Outflow Rates for Gas with $v_{out} > 1$ km s^{-1}, within 5100∼6460 au and 6460–7820 au Away from the Source

	5100∼6460 au						6460∼7820 au					
Source	$\dot{M}_B$ [a]	$\dot{M}_R$ [a]	$\dot{P}_R$ [b]	$\dot{P}_B$ [b]	$\dot{E}_R$ [c]	$\dot{E}_B$ [c]	$\dot{M}_B$ [a]	$\dot{M}_R$ [a]	$\dot{P}_R$ [b]	$\dot{P}_B$ [b]	$\dot{E}_R$ [c]	$\dot{E}_B$ [c]
HOPS 10	0.81	3.01	13.79	79.83	3.51E+42	6.55E+43	0.67	2.83	12.50	96.41	3.87E+42	8.03E+43
HOPS 10 no jet	0.81	3.01	13.79	79.83	3.51E+42	6.55E+43	0.67	2.83	12.50	96.41	3.87E+42	8.03E+43
HOPS 11	1.31	4.21	8.98	36.26	1.05E+42	7.17E+42	1.18	3.32	7.03	28.11	6.67E+41	5.20E+42
HOPS 11 no jet	1.31	4.21	8.98	36.26	1.05E+42	7.17E+42	1.18	3.32	7.03	28.11	6.67E+41	5.20E+42
HOPS 164	0.38	1.73	5.43	26.69	2.58E+42	1.72E+43	NA	1.27	0.02	19.13	4.90E+39	1.28E+43
HOPS 164 no jet	0.38	1.73	5.43	26.69	2.58E+42	1.72E+43	NA	1.27	0.02	19.13	4.90E+39	1.28E+43
HOPS 169	1.94	1.48	15.51	16.61	1.75E+42	2.35E+42	1.24	1.46	9.97	14.78	1.04E+42	1.86E+42
HOPS 198	0.16	1.28	3.38	21.88	3.17E+42	1.64E+43	0.09	0.34	1.82	3.32	1.97E+42	3.40E+42
HOPS 355	0.10	0.05	0.38	0.48	2.95E+40	6.94E+40	0.13	0.04	0.47	0.41	3.99E+40	6.89E+40
HOPS 408	NA	NA	NA	NA	NA	NA	NA	NA	NA	NA	NA	NA
HOPS 127	0.06	1.21	0.46	5.57	6.89E+40	4.87E+41	0.03	1.21	0.21	4.55	3.95E+40	2.76E+41
HOPS 130	0.22	NA	3.14	NA	1.04E+42	NA	0.11	NA	1.81	NA	9.79E+41	NA
HOP 135	0.01	1.60	0.06	6.29	1.59E+40	3.46E+41	NA	NA	NA	NA	NA	NA
HOPS 157	0.04	NA	0.18	NA	1.70E+40	NA	NA	NA	NA	NA	NA	NA
HOPS 177	4.13	0.19	14.62	1.24	7.99E+41	4.17E+41	3.00	0.20	10.94	1.59	6.29E+41	6.46E+41
HOPS 185	5.18	0.21	19.39	4.35	1.18E+42	3.43E+42	5.05	0.09	18.63	3.09	9.98E+41	2.95E+42
HOPS 191	0.65	0.02	5.27	0.49	1.19E+42	3.93E+41	0.26	0.01	2.12	0.16	6.94E+41	1.01E+41
HOPS 129	0.08	NA	0.36	NA	6.34E+40	NA	0.07	NA	0.39	NA	1.01E+41	NA
HOPS 134	NA	0.08	NA	0.63	NA	2.17E+41	NA	0.06	NA	0.47	NA	1.64E+41
HOPS 13	0.18	NA	0.74	NA	3.95E+40	NA	NA	NA	NA	NA	NA	NA
HOPS 150	0.04	NA	1.03	NA	4.03E+41	NA	0.01	NA	0.16	NA	5.06E+40	NA
HOPS 166	0.34	1.00	1.87	5.06	1.46E+41	3.63E+41	0.32	0.51	1.74	2.49	1.24E+41	1.61E+41
HOPS 194	NA	0.15	NA	1.85	NA	5.08E+41	NA	0.12	NA	1.55	NA	4.32E+41
HOPS 200	NA	NA	NA	NA	NA	NA	NA	NA	NA	NA	NA	NA

Notes.
[a] In units of $M_\odot$ Myr^{-1}.
[b] In units of $M_\odot$ km s^{-1} Myr^{-1}.
[c] In units of erg Myr^{-1}.

Table 17
Molecular Outflow Rates for Gas with $v_{out} > 1$ km s^{-1}, within 7820∼9180 au Away from the Source

	7820∼9180 au					
Source	$\dot{M}_B$ [a]	$\dot{M}_R$ [a]	$\dot{P}_R$ [b]	$\dot{P}_B$ [b]	$\dot{E}_R$ [c]	$\dot{E}_B$ [c]
HOPS 10	0.32	1.91	5.23	78.07	1.54E+42	6.62E+43
HOPS 10 no jet	0.32	1.91	5.23	78.07	1.54E+42	6.62E+43
HOPS 11	1.18	2.18	6.59	22.01	5.58E+41	4.13E+42
HOPS 11 no jet	1.18	2.18	6.59	22.01	5.58E+41	4.13E+42
HOPS 164	NA	1.00	NA	18.66	NA	1.40E+43
HOPS 164 no jet	NA	1.00	NA	18.66	NA	1.40E+43
HOPS 169	1.02	1.37	8.91	12.15	9.47E+41	1.40E+42
HOPS 198	0.11	NA	3.18	NA	4.21E+42	NA
HOPS 355	0.11	0.04	0.39	0.36	3.50E+40	9.02E+40
HOPS 408	NA	NA	NA	NA	NA	NA
HOPS 127	0.07	1.29	0.40	4.91	7.05E+40	3.50E+41
HOPS 130	NA	NA	NA	NA	NA	NA
HOP 135	NA	NA	NA	NA	NA	NA
HOPS 157	NA	NA	NA	NA	NA	NA
HOPS 177	0.96	0.17	3.81	1.64	2.84E+41	7.29E+41
HOPS 185	NA	NA	NA	NA	NA	NA
HOPS 191	NA	NA	NA	NA	NA	NA
HOPS 129	0.05	NA	0.28	NA	4.96E+40	NA
HOPS 134	NA	0.05	NA	0.49	NA	1.88E+41
HOPS 13	NA	NA	NA	NA	NA	NA
HOPS 150	0.02	NA	0.20	NA	6.27E+40	NA
HOPS 166	0.14	0.39	0.73	2.23	5.67E+40	1.65E+41
HOPS 194	NA	0.07	NA	1.06	NA	3.10E+41
HOPS 200	NA	NA	NA	NA	NA	NA

Notes.
[a] In units of $M_\odot$ Myr^{-1}.
[b] In units of $M_\odot$ km s^{-1} Myr^{-1}.
[c] In units of erg Myr^{-1}.

Appendix F
Two-dimensional Mass, Momentum, Energy, Mass rate, Momentum Rate (Force), and Energy Rate (Mechanical Luminosity) Maps for All Outflows

In this section, we present the two-dimensional mass, momentum, energy, mass rate, momentum rate (force), and energy rate (mechanical luminosity) maps for all outflows (see Figures 21–43). All the rate maps are computed from our PFT technique. Instead of a single rate value obtained by previous methods, the PFT technique allows us to compute two-dimensional molecular outflow instantaneous rate maps for the first time.

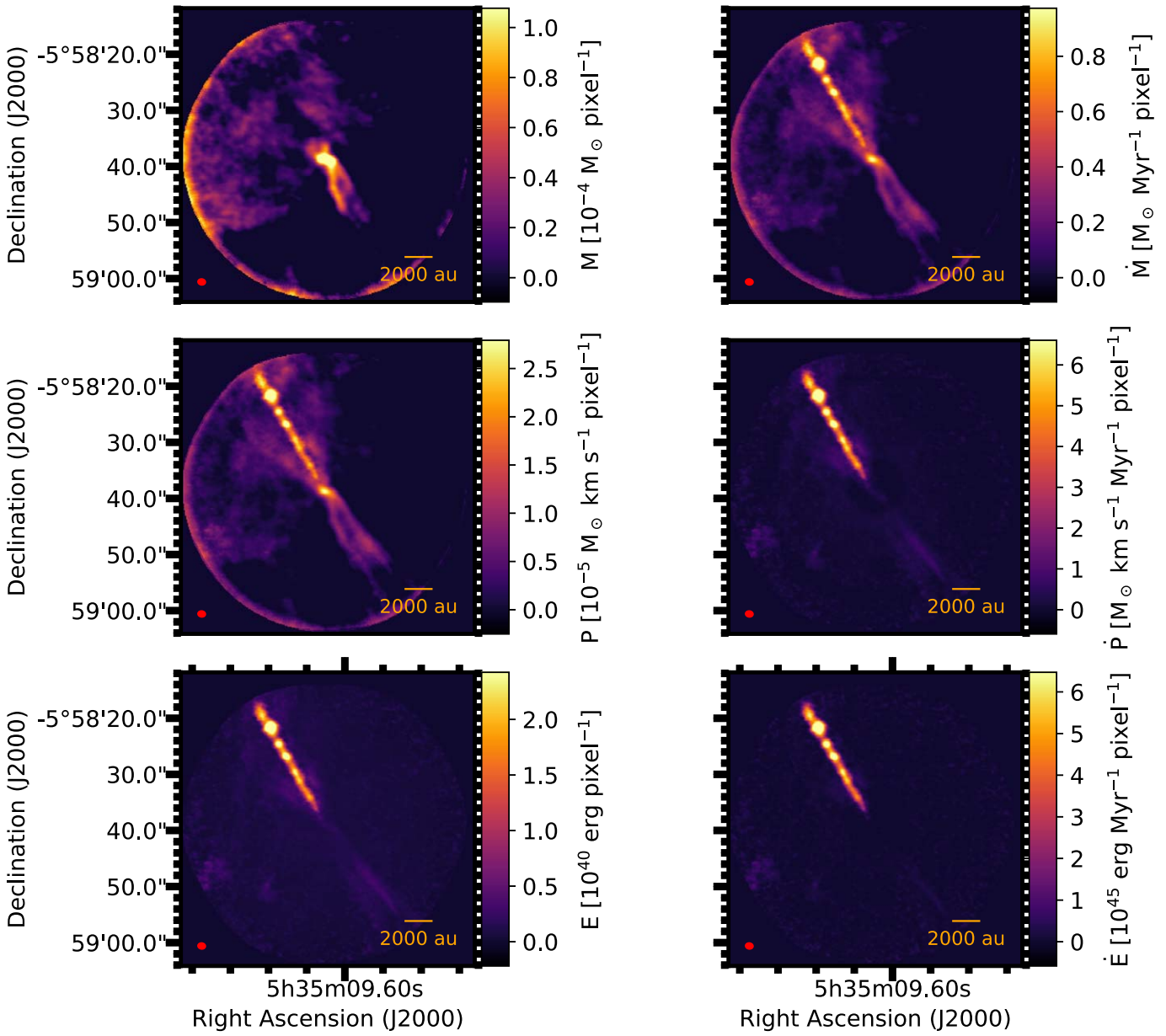

Figure 21. HOPS 10 molecular outflow mass, momentum, and energy maps (panels in the left column), and the corresponding rate maps (panels in the right column). The red ellipse in the bottom left of each panel represents the synthesized beam. Note that the pixel size is the same for all maps and is $0\farcs17 \times 0\farcs17$.

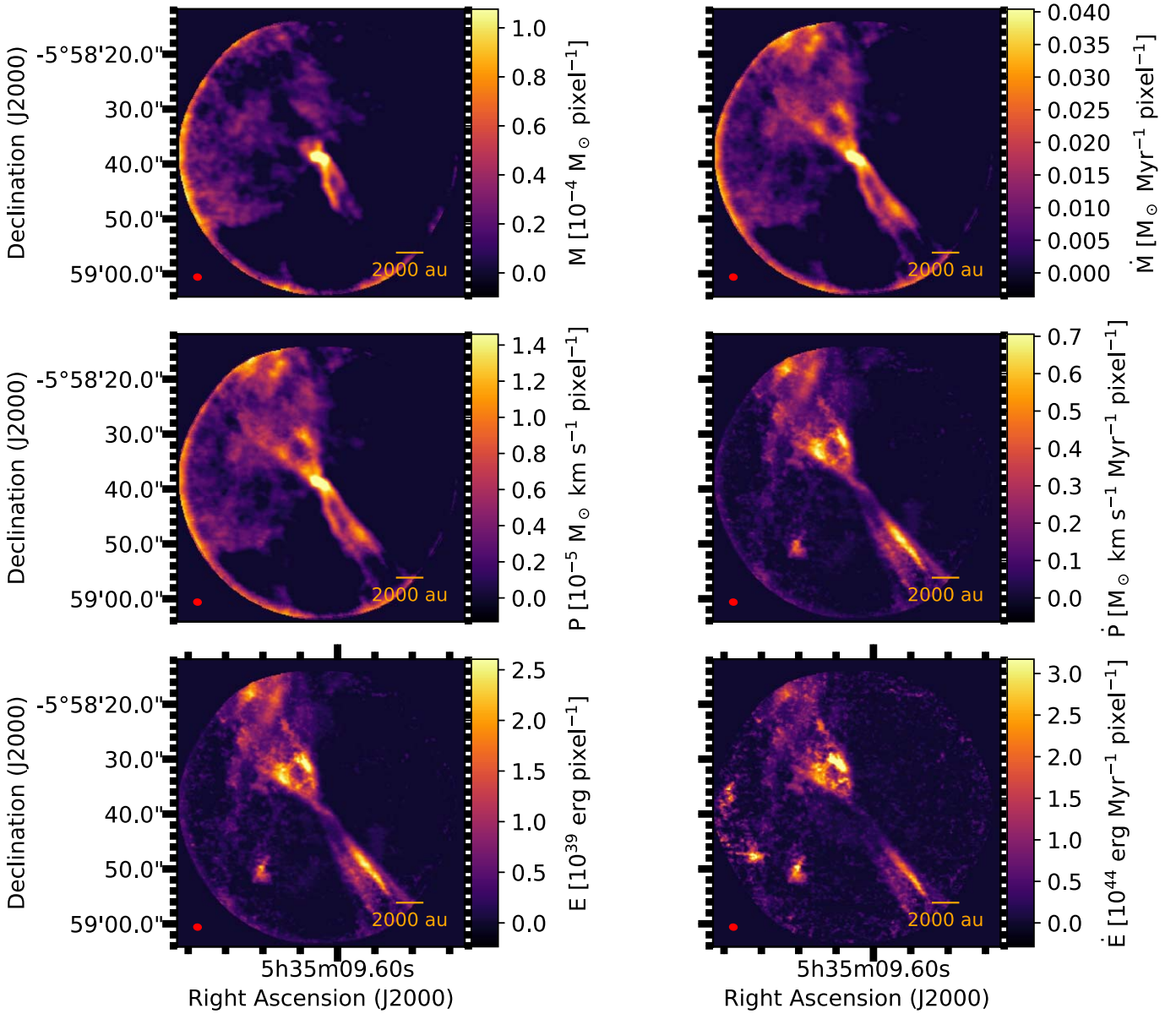

Figure 22. HOPS 10 outflow mass, momentum, energy maps, and the corresponding instantaneous rate maps. Note, we exclude the high-velocity jet components. The pixel size is $0\farcs17 \times 0\farcs17$. The red ellipses in the bottom left of the plots represent the synthesized beam.

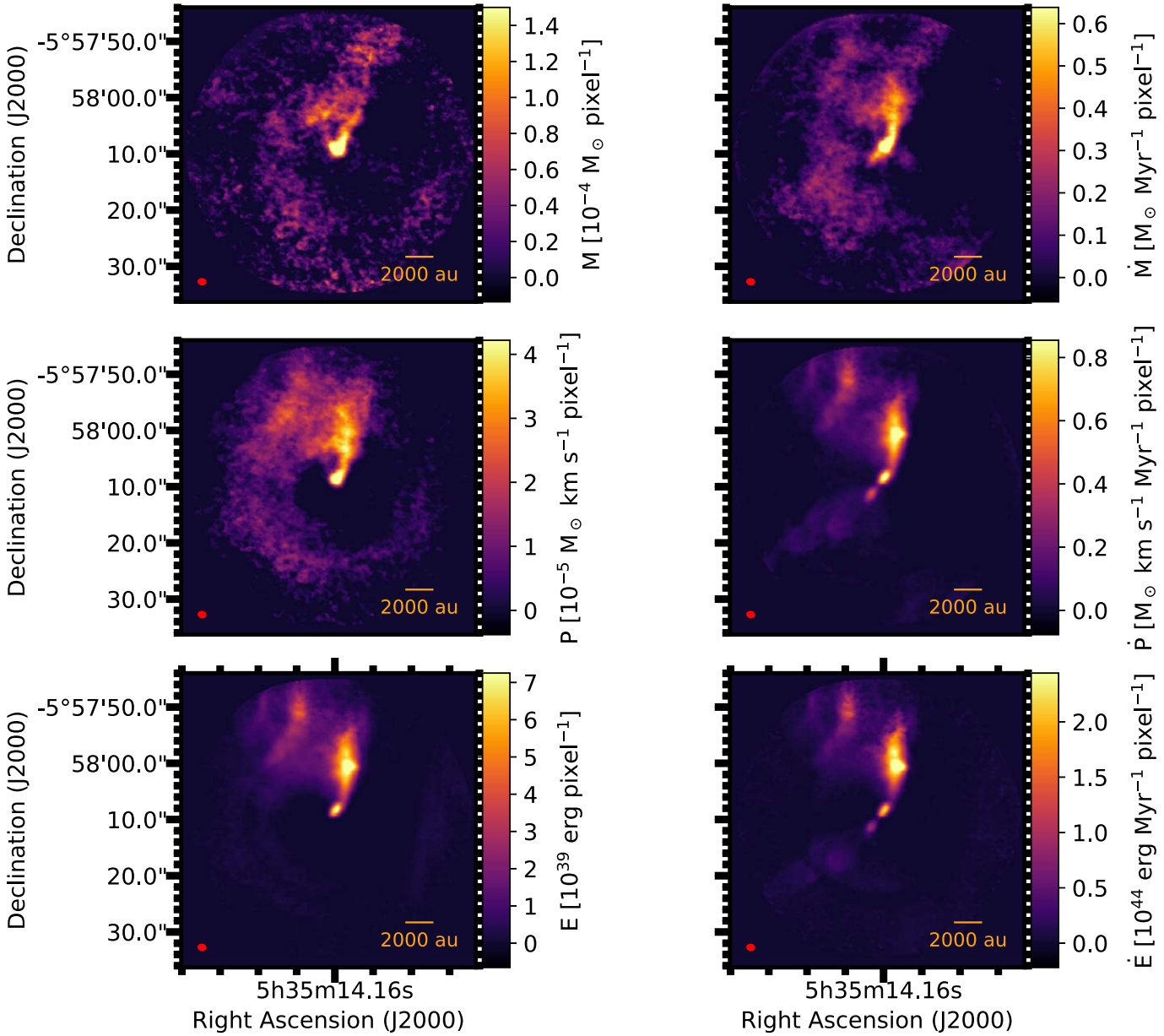

Figure 23. HOPS 11 outflow mass, momentum, energy maps, and the corresponding instantaneous rate maps. Note that the pixel size is $0\farcs17 \times 0\farcs17$. The red ellipses in the bottom left of the plots represent the synthesized beam.

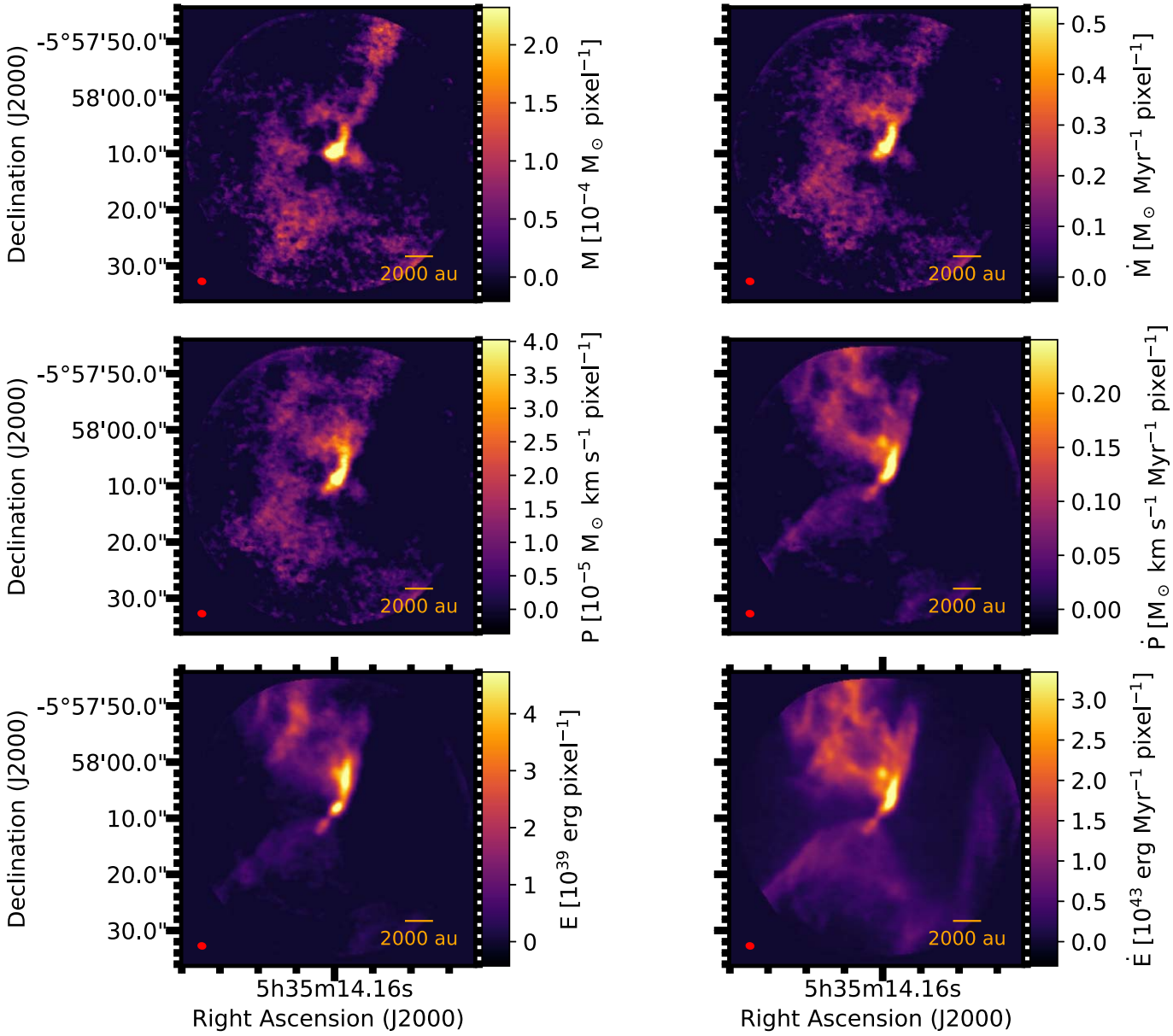

Figure 24. HOPS 11 outflow mass, momentum, energy maps, and the corresponding instantaneous rate maps. Note, we exclude the high-velocity jet components. Note that the pixel size is $0\farcs17 \times 0\farcs17$. The red ellipses in the bottom left of the plots represent the synthesized beam.

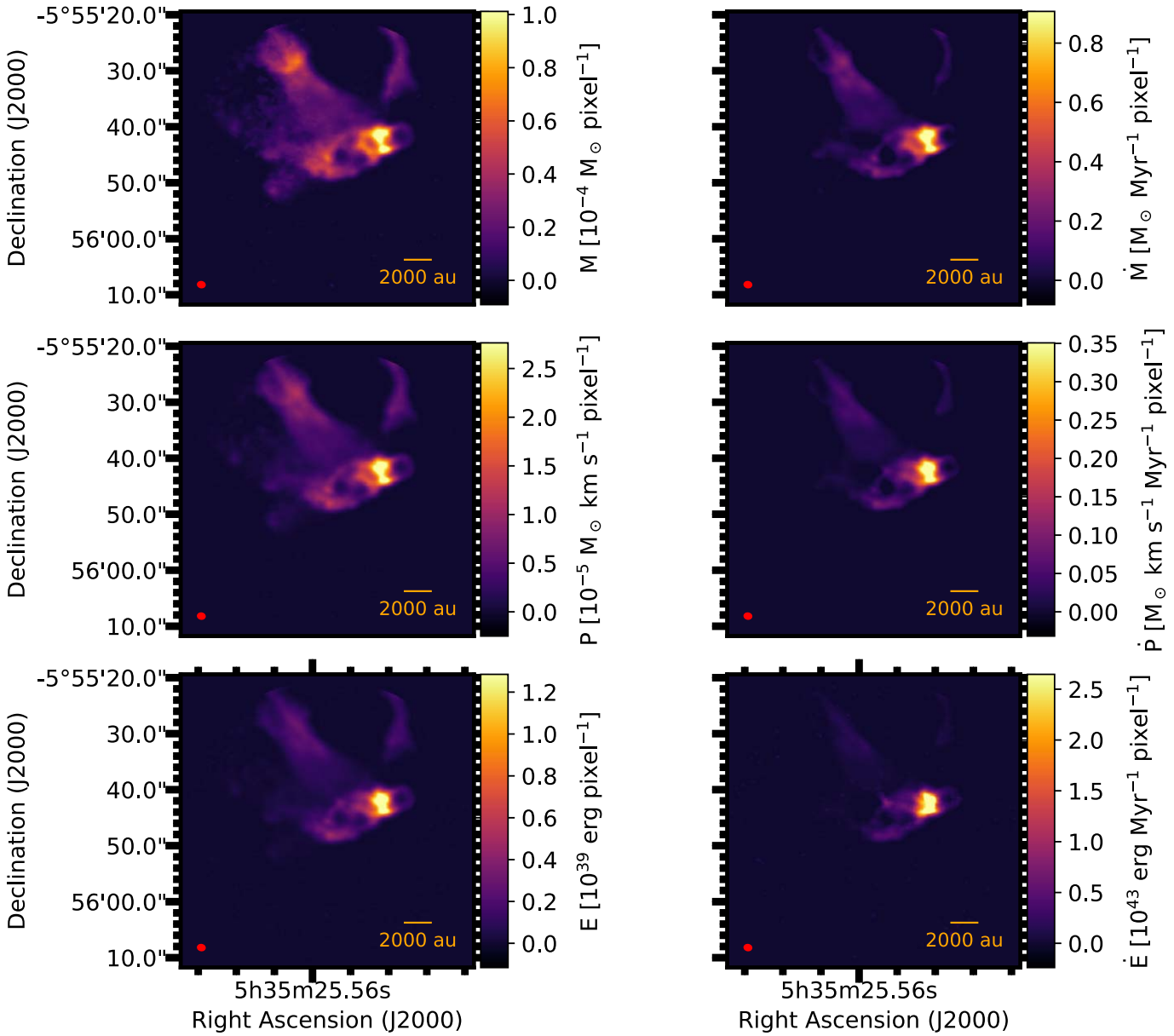

Figure 25. HOPS 13 outflow mass, momentum, energy maps, and the corresponding instantaneous rate maps. Note that the pixel size is $0\farcs17 \times 0\farcs17$. The red ellipses in the bottom left of the plots represent the synthesized beam.

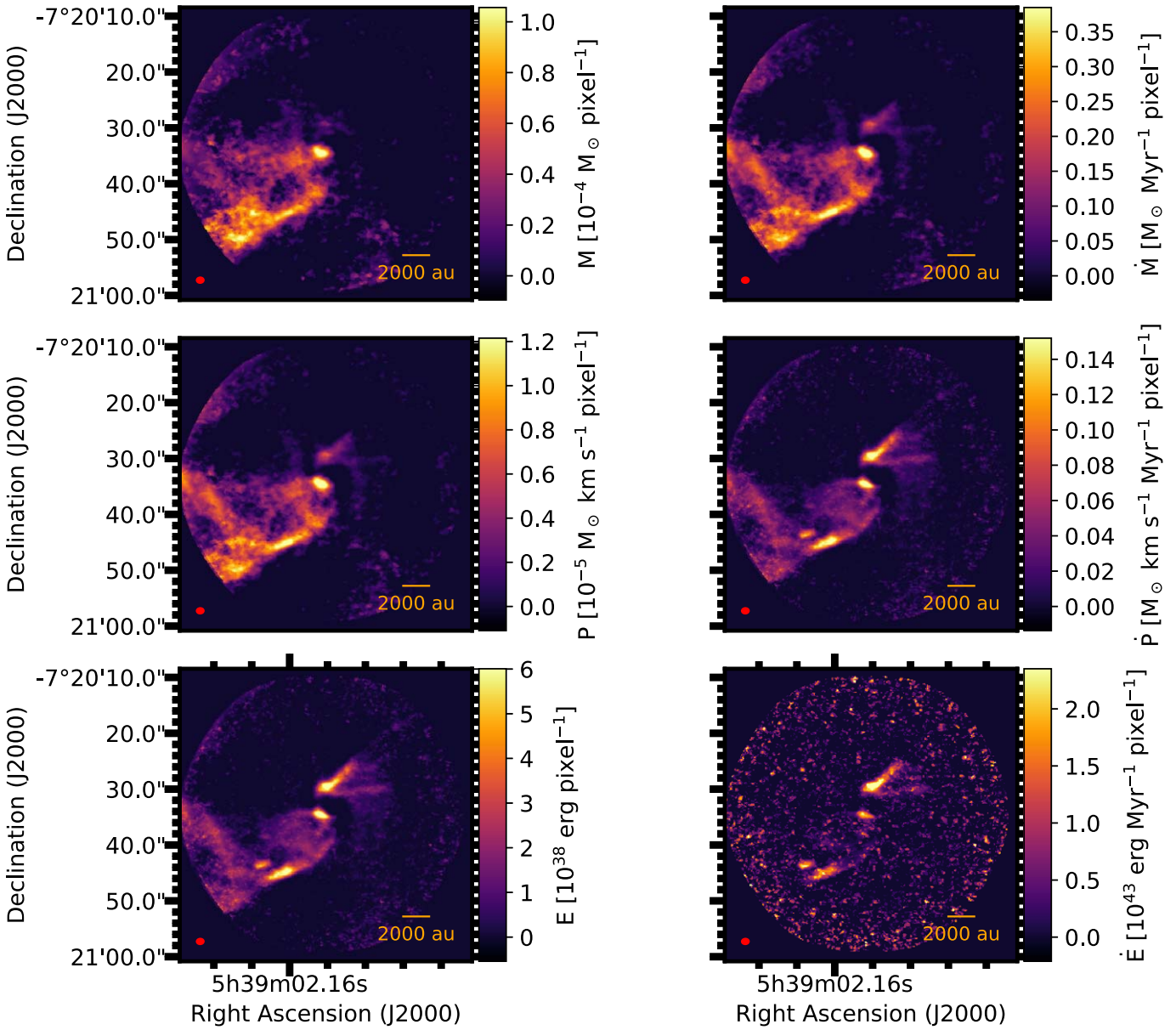

Figure 26. HOPS 127 outflow mass, momentum, energy maps, and the corresponding instantaneous rate maps. Note that the pixel size is $0\farcs17 \times 0\farcs17$. The red ellipses in the bottom left of the plots represent the synthesized beam.

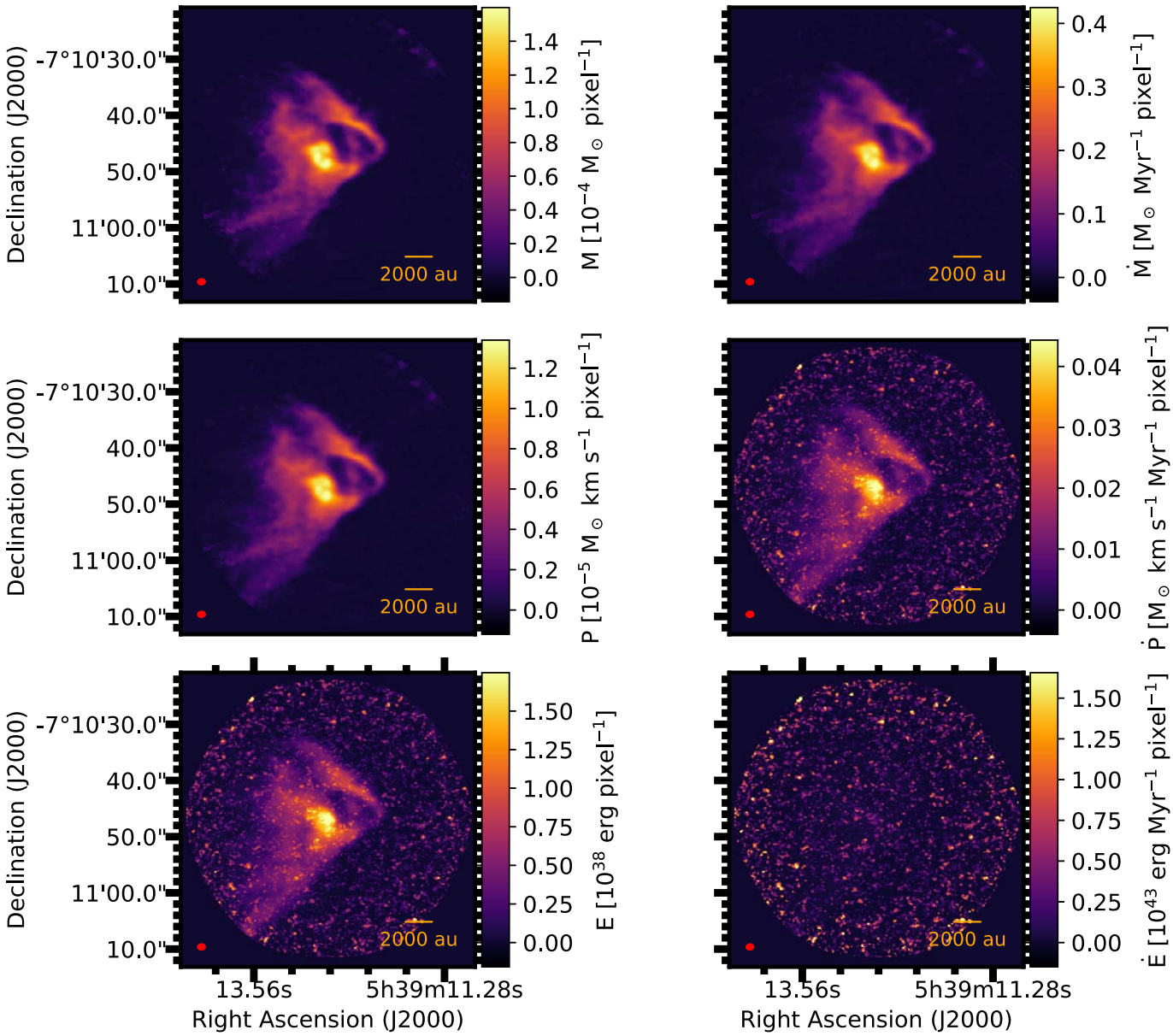

Figure 27. HOPS 129 outflow mass, momentum, energy maps, and the corresponding instantaneous rate maps. Note that the pixel size is $0\farcs17 \times 0\farcs17$. The red ellipses in the bottom left of the plots represent the synthesized beam. There is no detection in the energy ejection rate map due to the high noise level.

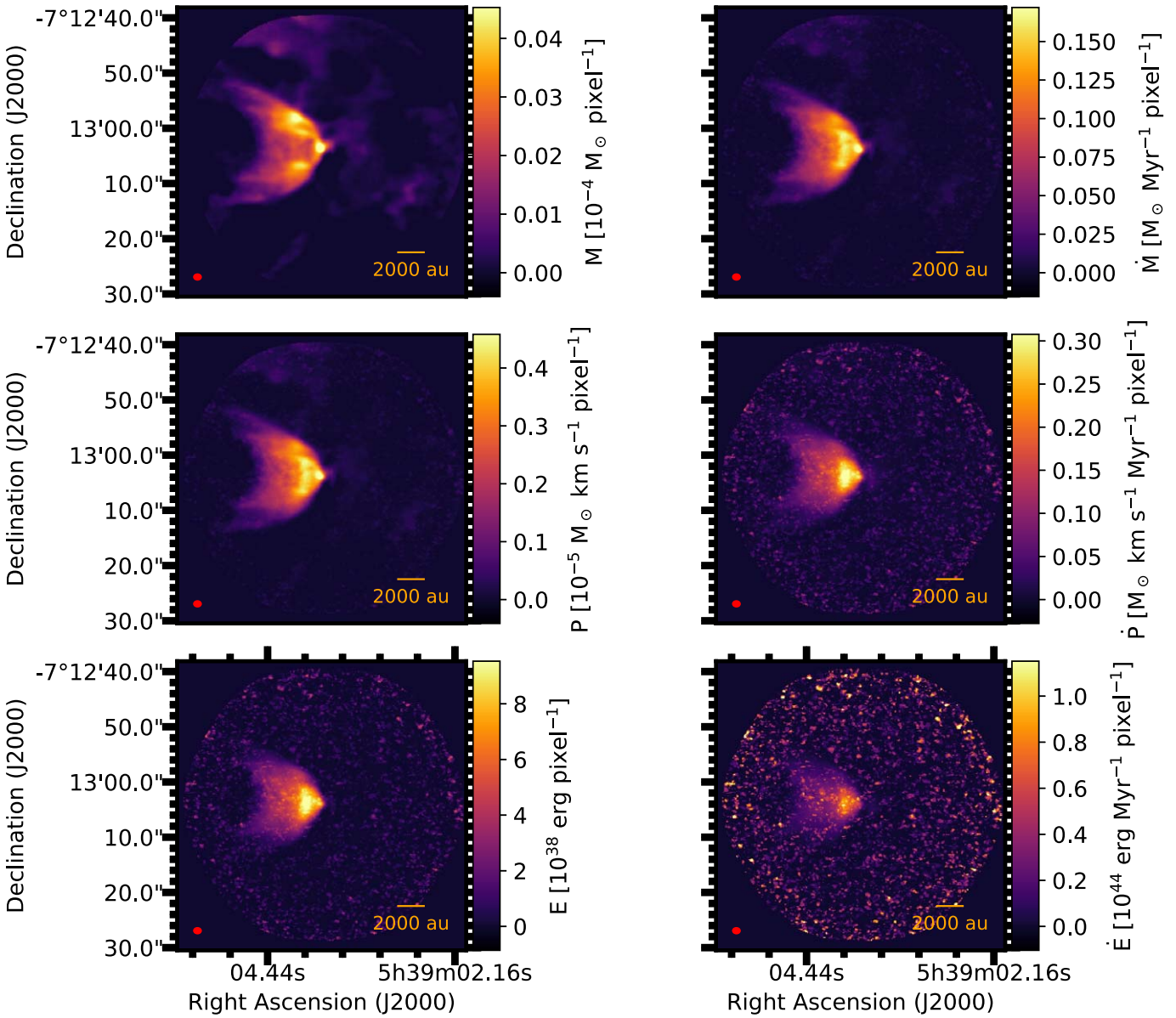

Figure 28. HOPS 130 outflow mass, momentum, energy maps, and the corresponding instantaneous rate maps. Note that the pixel size is $0\farcs17 \times 0\farcs17$. The red ellipses in the bottom left of the plots represent the synthesized beam.

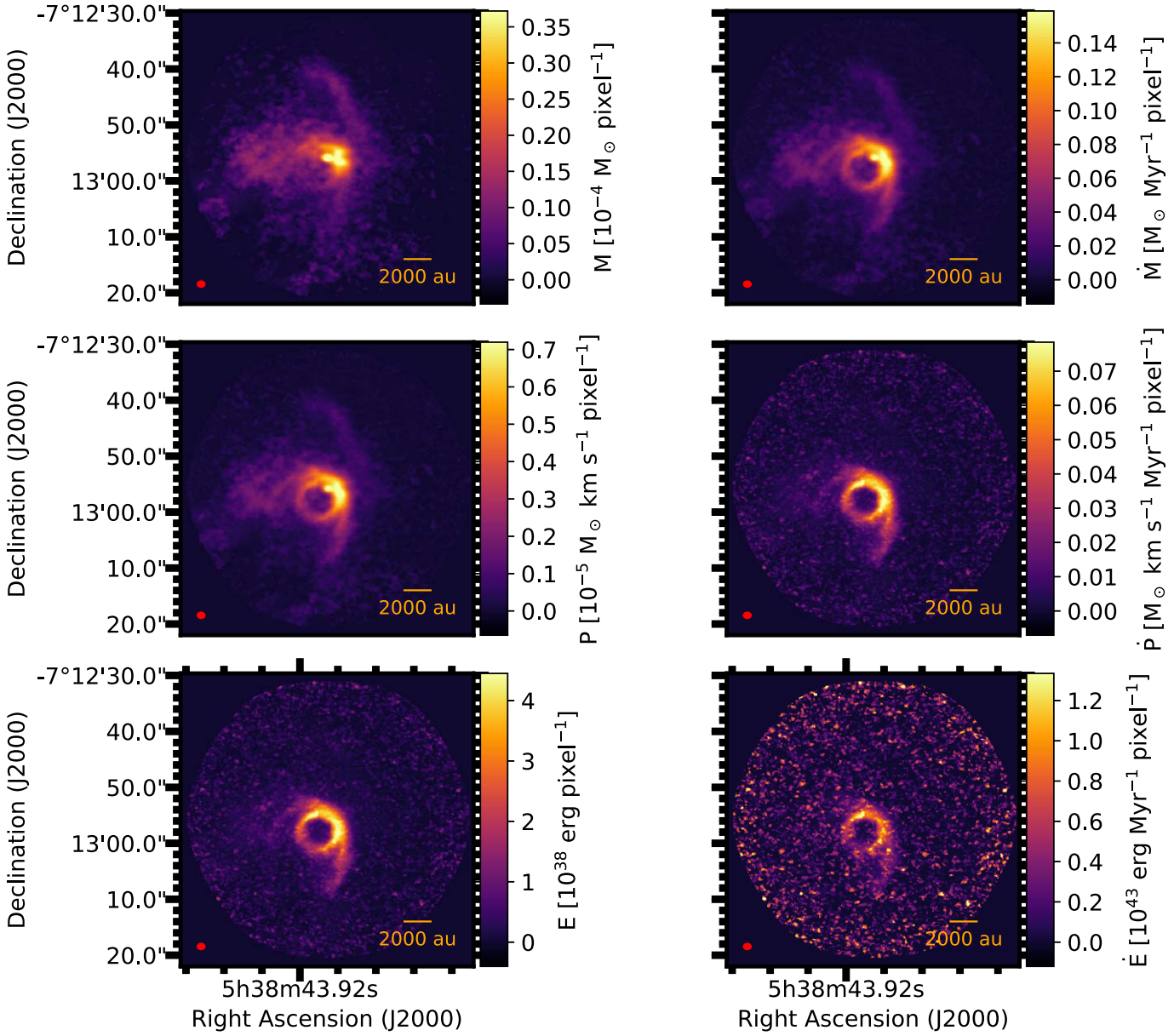

Figure 29. HOPS 134 outflow mass, momentum, energy maps, and the corresponding instantaneous rate maps. Note that the pixel size is $0\farcs17 \times 0\farcs17$. The red ellipses in the bottom left of the plots represent the synthesized beam.

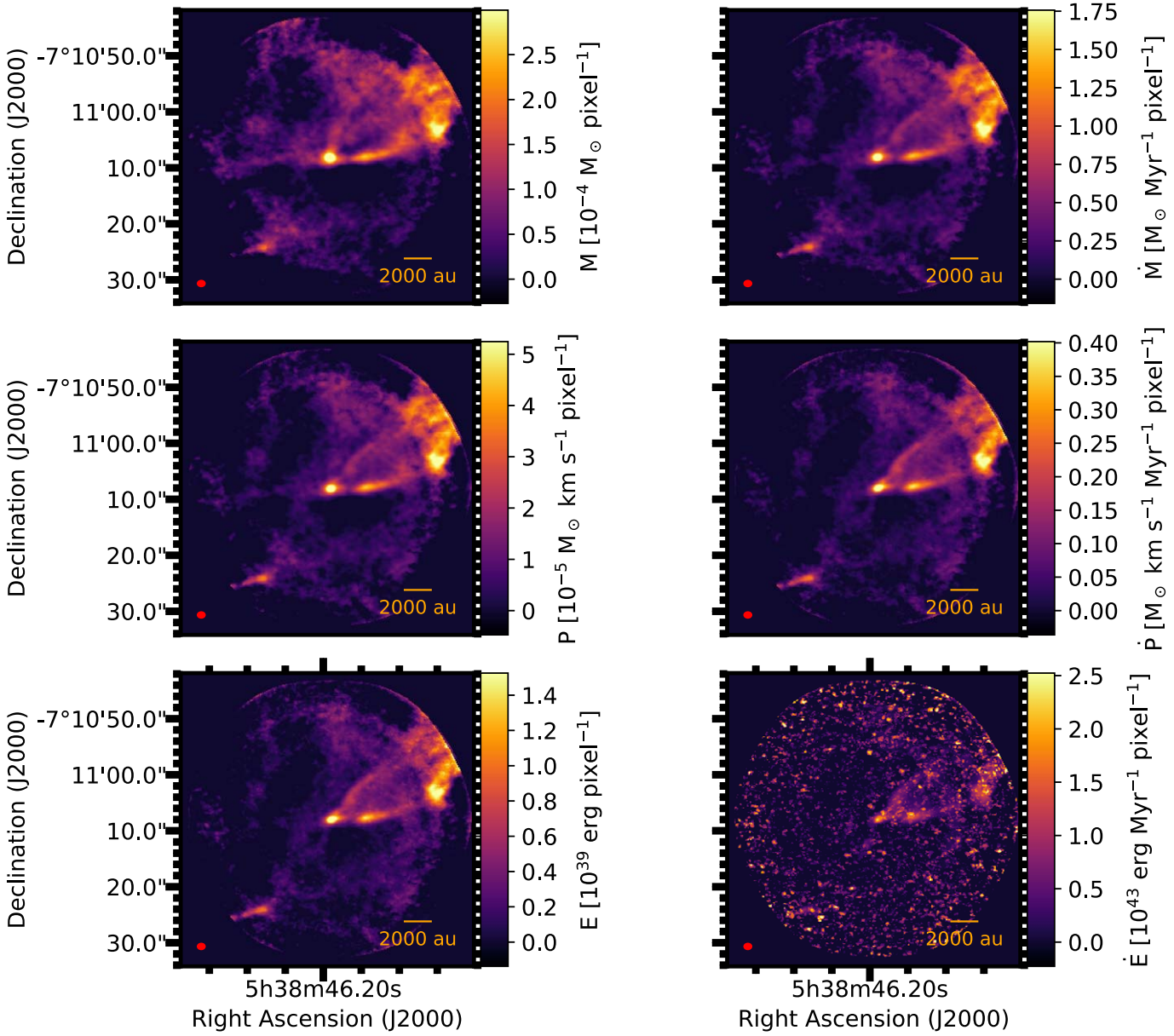

Figure 30. HOPS 135 outflow mass, momentum, energy maps, and the corresponding instantaneous rate maps. Note that the pixel size is $0\farcs17 \times 0\farcs17$. The red ellipses in the bottom left of the plots represent the synthesized beam.

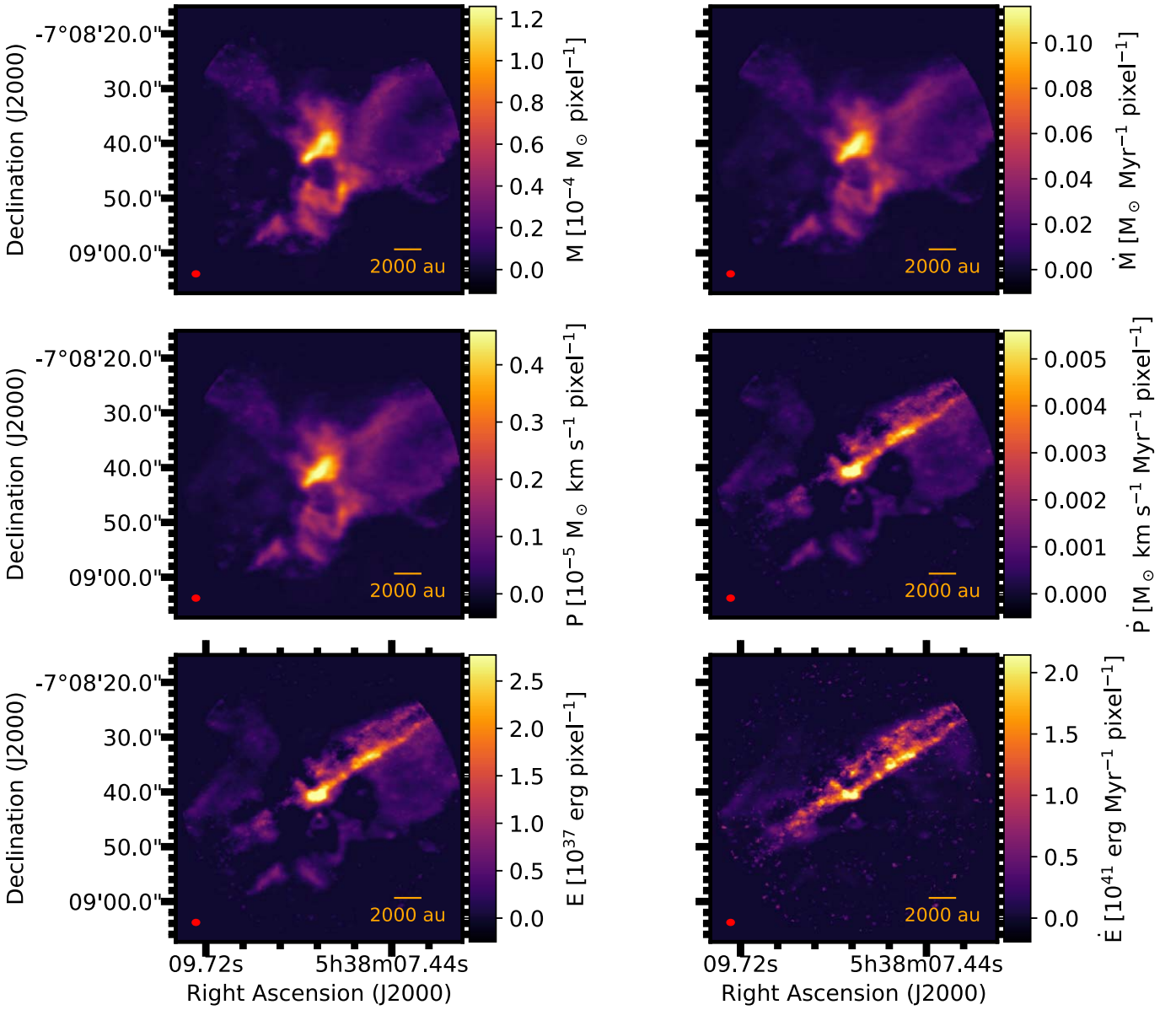

Figure 31. HOPS 150 outflow mass, momentum, energy maps, and the corresponding instantaneous rate maps. Note that the pixel size is $0\farcs17 \times 0\farcs17$. The red ellipses in the bottom left of the plots represent the synthesized beam. Two jets with molecular bullets appear clearly in the energy ejection rate maps. The southern jet coincides spatially with HOPS 150 A, but the northern jet originated from a nearby source outside the field of view.

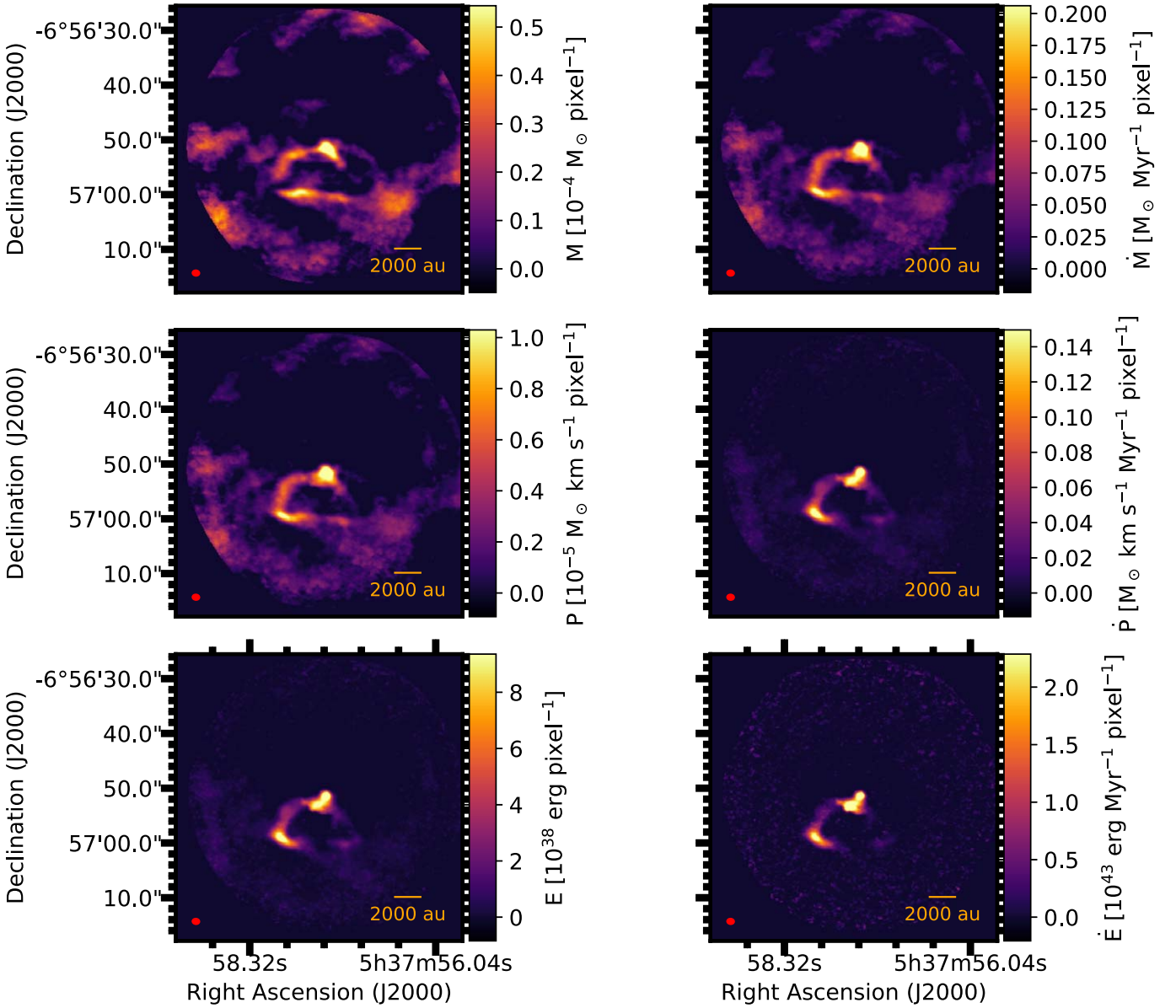

Figure 32. HOPS 157 outflow mass, momentum, energy maps, and the corresponding instantaneous rate maps. Note that the pixel size is $0\farcs17 \times 0\farcs17$. The red ellipses in the bottom left of the plots represent the synthesized beam.

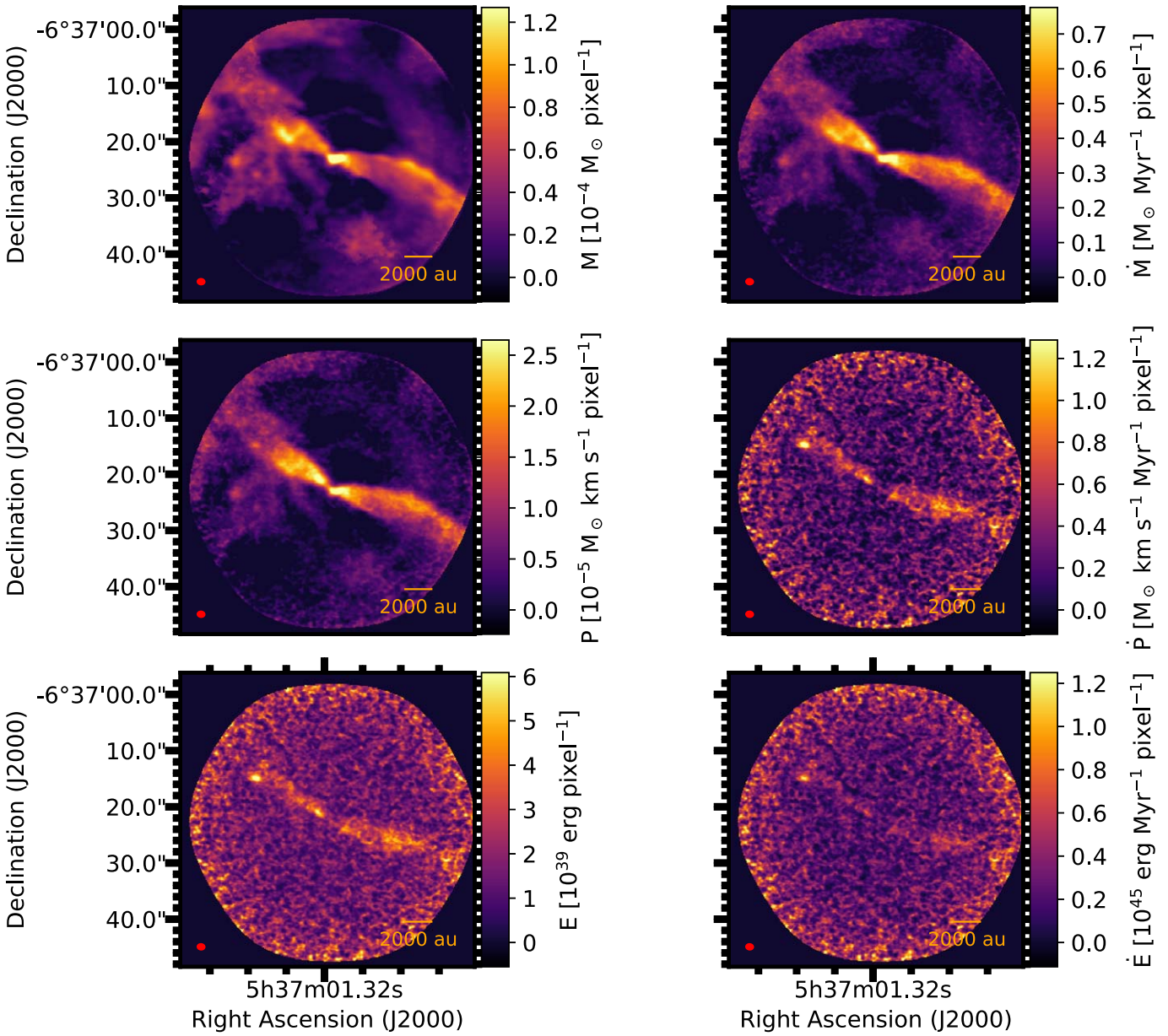

Figure 33. HOPS 164 outflow mass, momentum, energy maps, and the corresponding instantaneous rate maps. Note that the pixel size is $0\farcs17 \times 0\farcs17$. The red ellipses in the bottom left of the plots represent the synthesized beam.

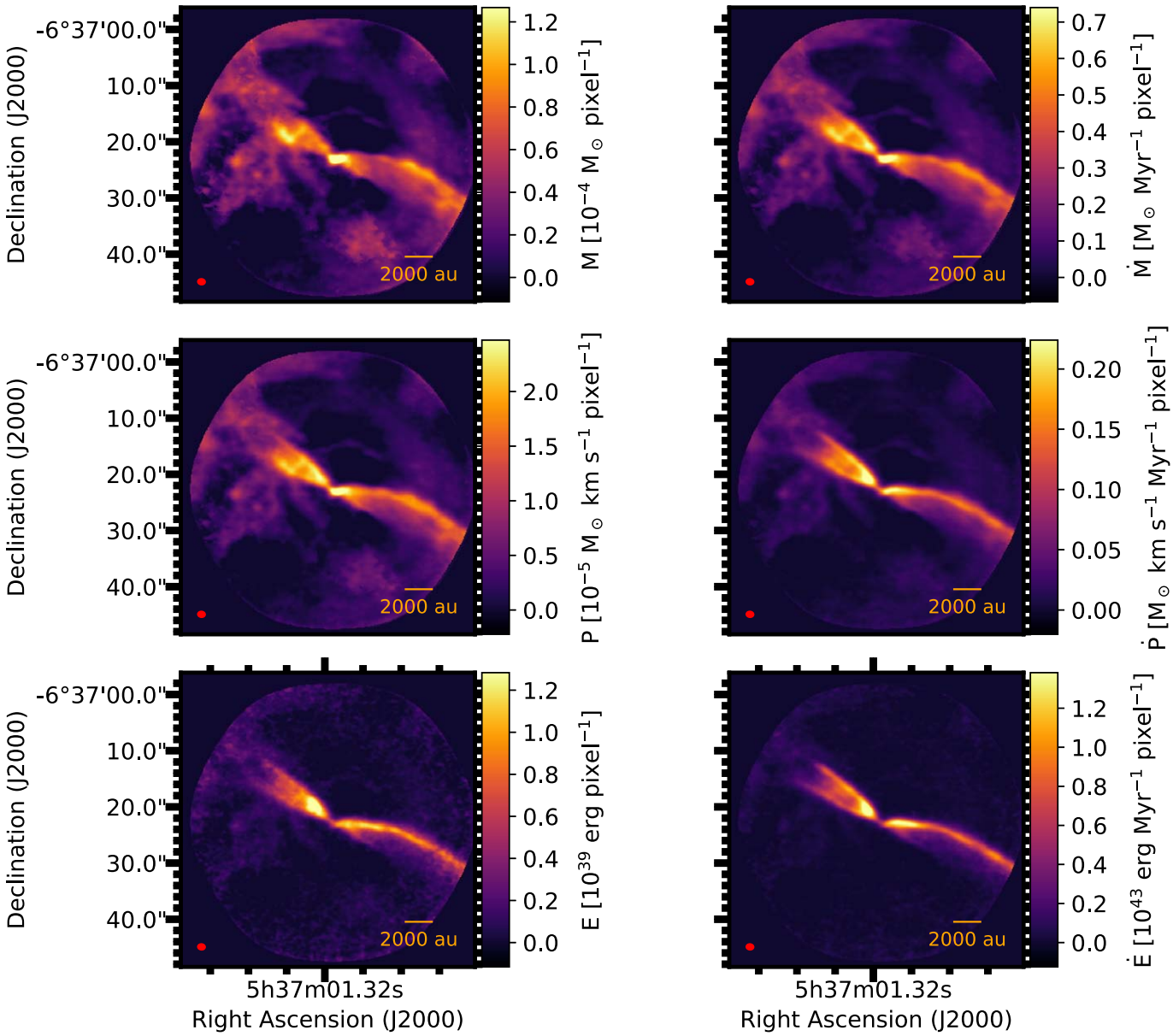

Figure 34. HOPS 164 outflow mass, momentum, energy maps, and 7the corresponding instantaneous rate maps. Note, we exclude the high-velocity jet components. The pixel size is $0\overset{''}{.}17 \times 0\overset{''}{.}17$. The red ellipses in the bottom left of the plots represent the synthesized beam.

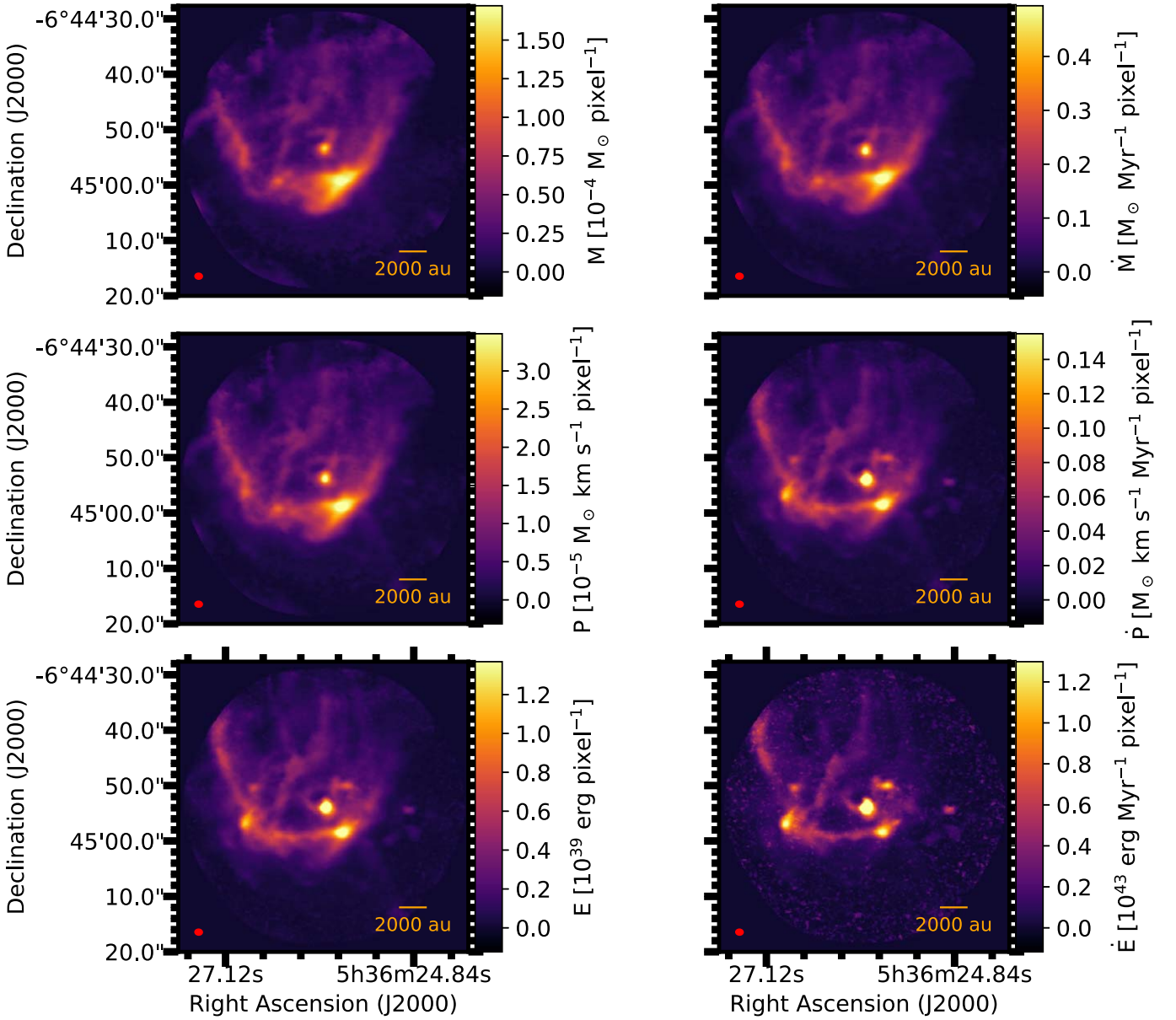

Figure 35. HOPS 166 outflow mass, momentum, energy maps, and the corresponding instantaneous rate maps. Note that the pixel size is $0\farcs17 \times 0\farcs17$. The red ellipses in the bottom left of the plots represent the synthesized beam.

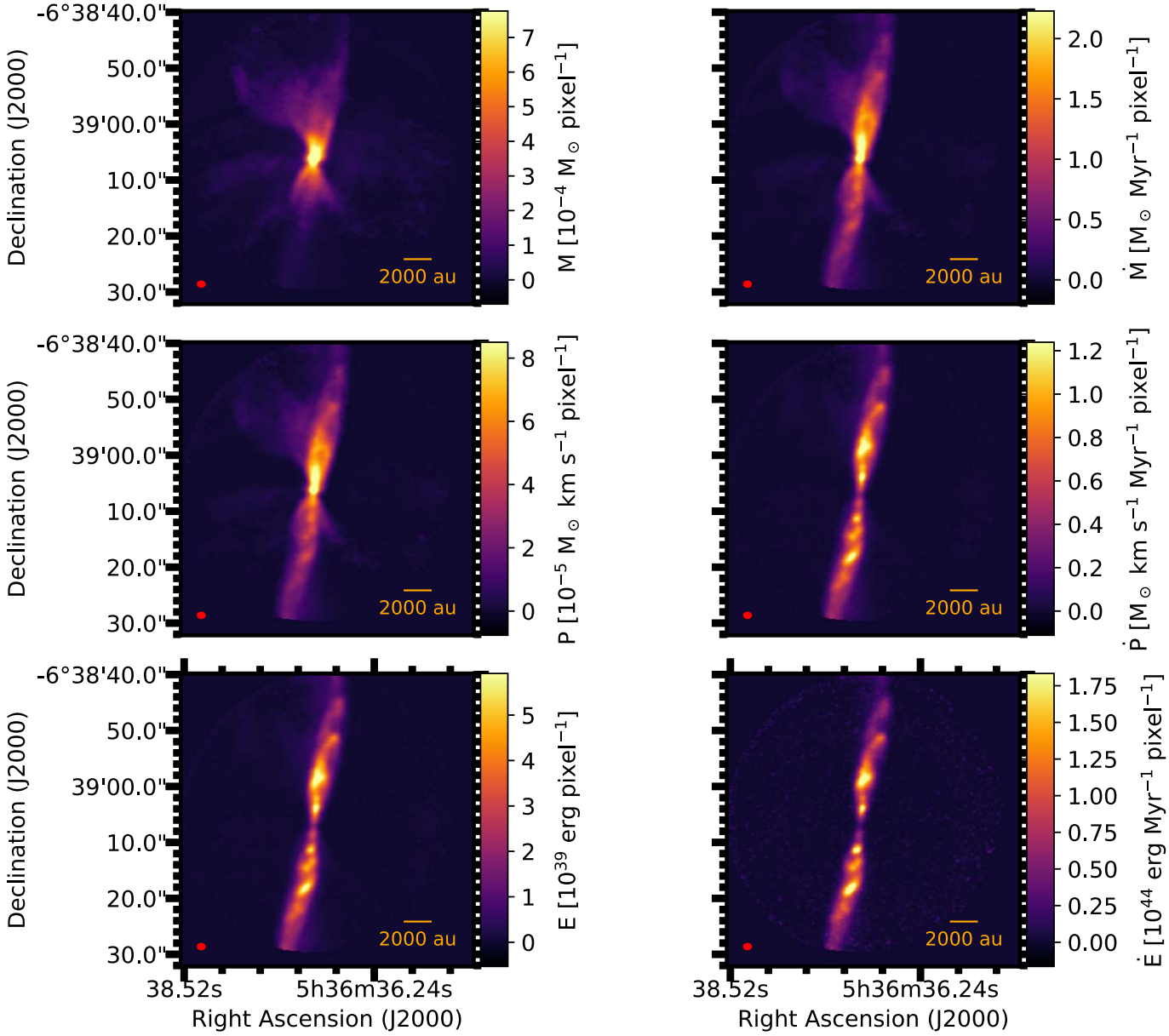

Figure 36. HOPS 169 outflow mass, momentum, energy maps, and the corresponding instantaneous rate maps. Note that the pixel size is $0\farcs17 \times 0\farcs17$. The red ellipses in the bottom left of the plots represent the synthesized beam.

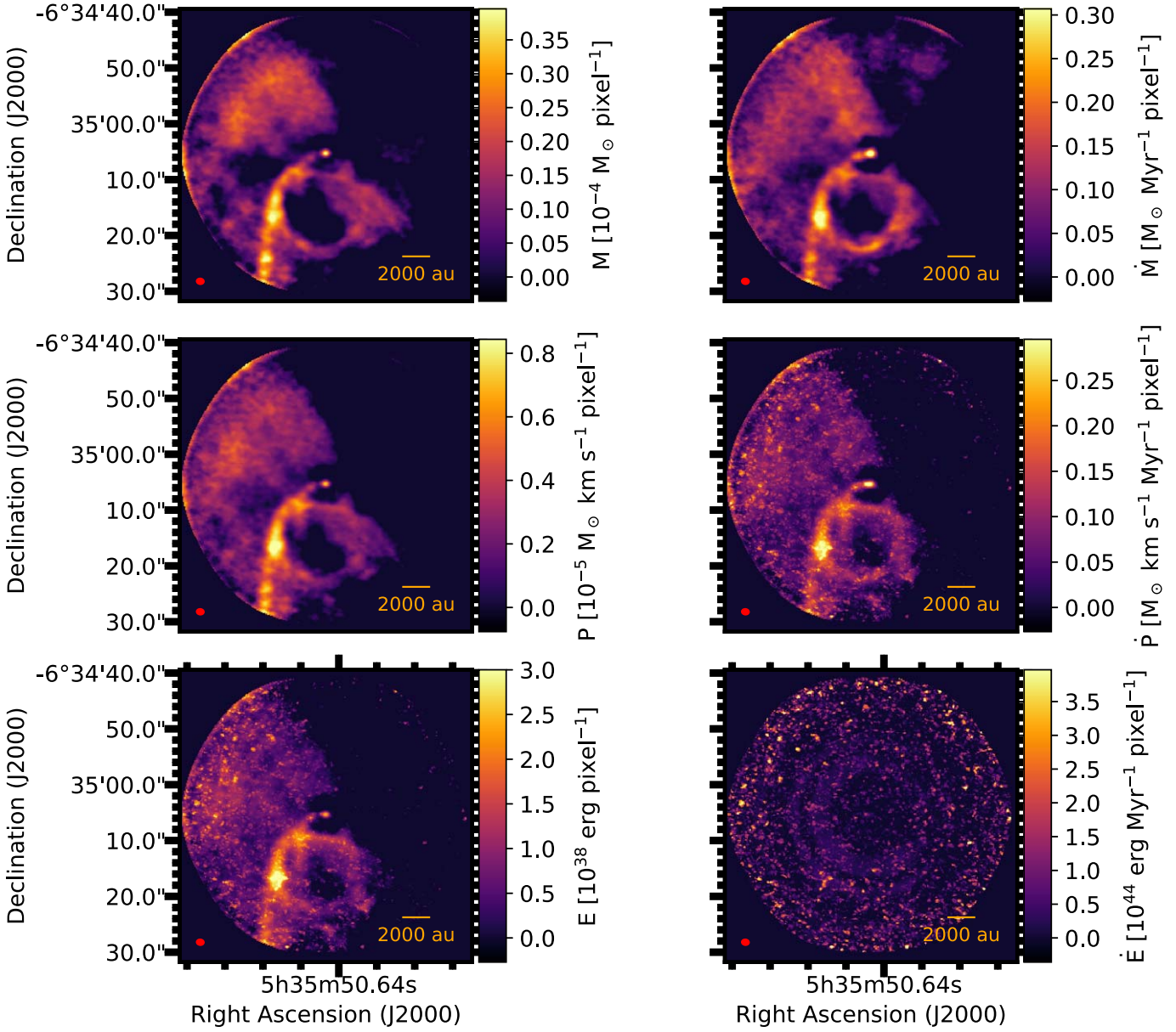

Figure 37. HOPS 177 outflow mass, momentum, energy maps, and the corresponding instantaneous rate maps. Note that the pixel size is $0\farcs17 \times 0\farcs17$. The red ellipses in the bottom left of the plots represent the synthesized beam. There is no detection in the energy ejection rate map due to the high noise level.

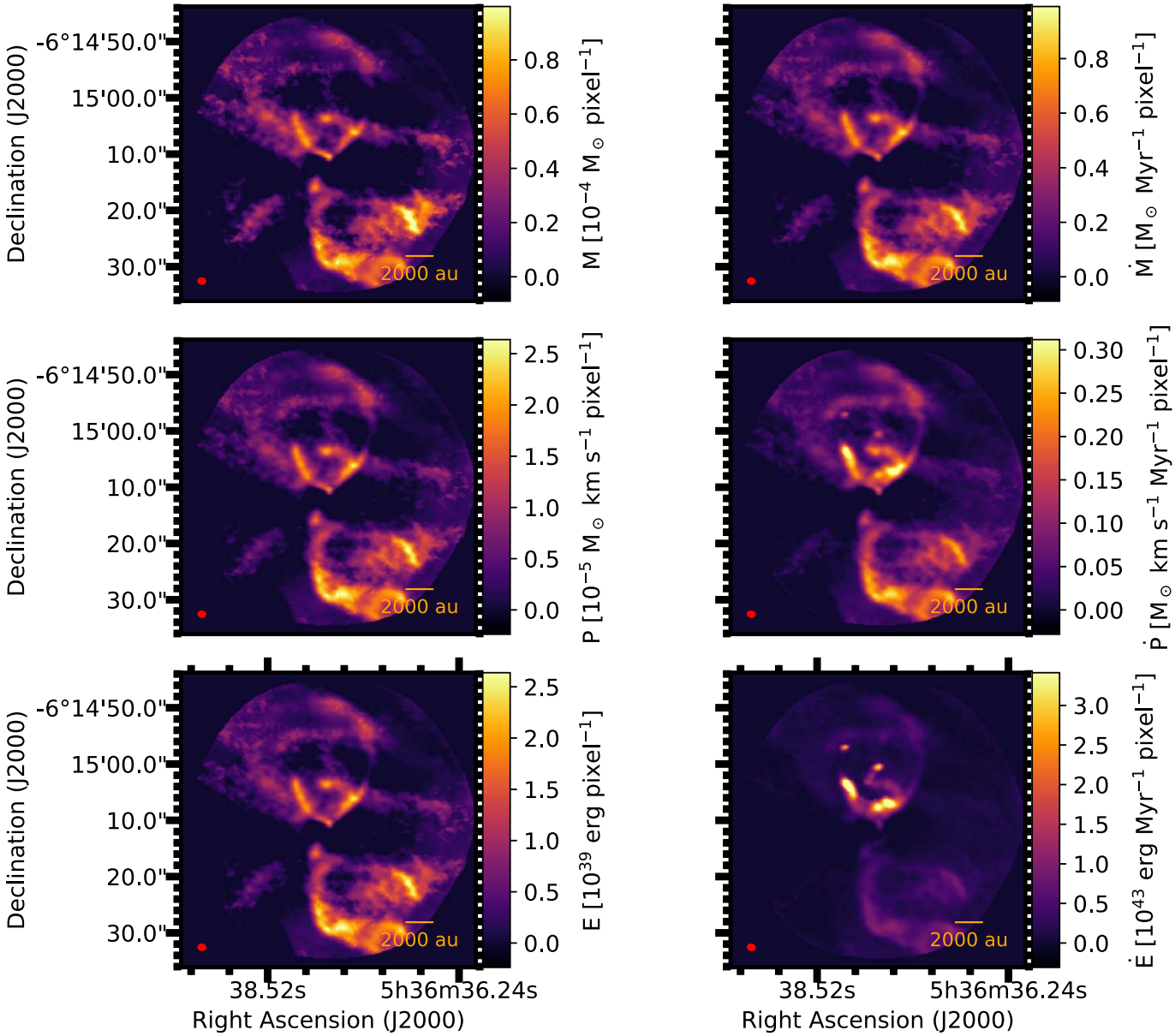

Figure 38. HOPS 185 outflow mass, momentum, energy maps, and the corresponding instantaneous rate maps. Note that the pixel size is $0\farcs17 \times 0\farcs17$. The red ellipses in the bottom left of the plots represent the synthesized beam.

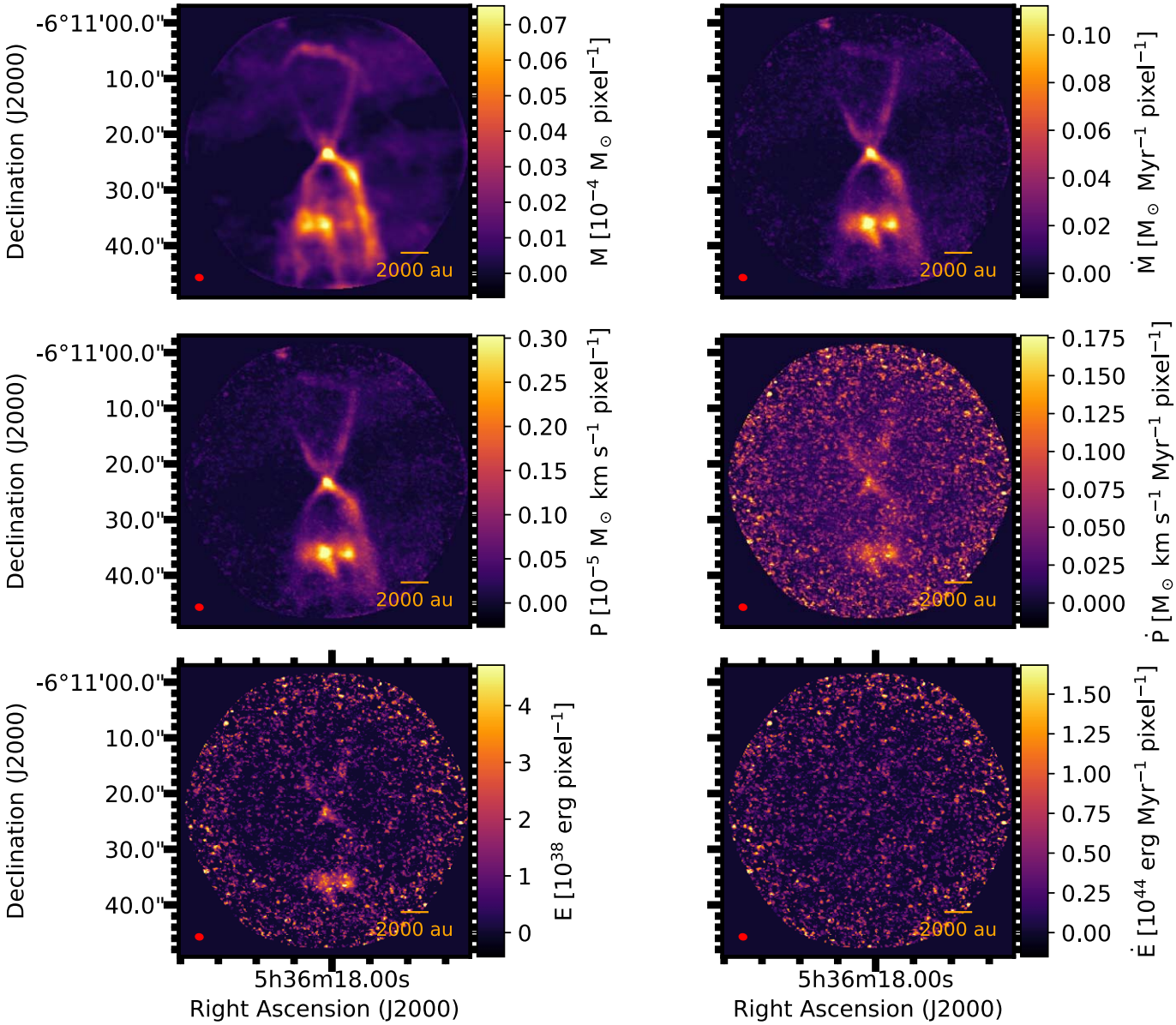

Figure 39. HOPS 191 outflow mass, momentum, energy maps, and the corresponding instantaneous rate maps. Note that the pixel size is $0\farcs17 \times 0\farcs17$. The red ellipses in the bottom left of the plots represent the synthesized beam. There is no detection in the energy ejection rate map due to the high noise level.

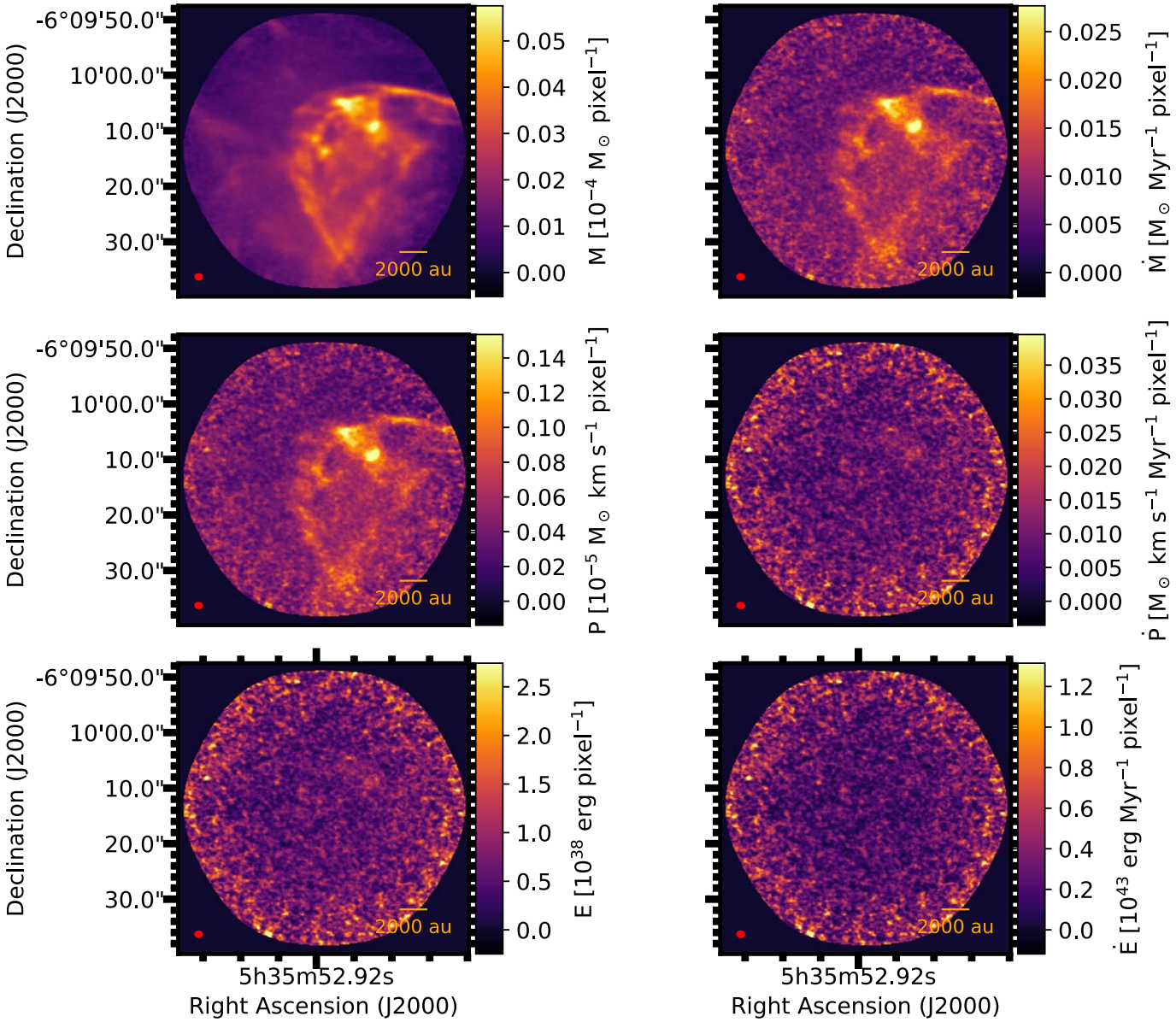

Figure 40. HOPS 194 outflow mass, momentum, energy maps, and the corresponding instantaneous rate maps. Note that the pixel size is $0\farcs17 \times 0\farcs17$. The red ellipses in the bottom left of the plots represent the synthesized beam. No clear detection is seen in the energy map, and the energy and momentum ejection rate maps.

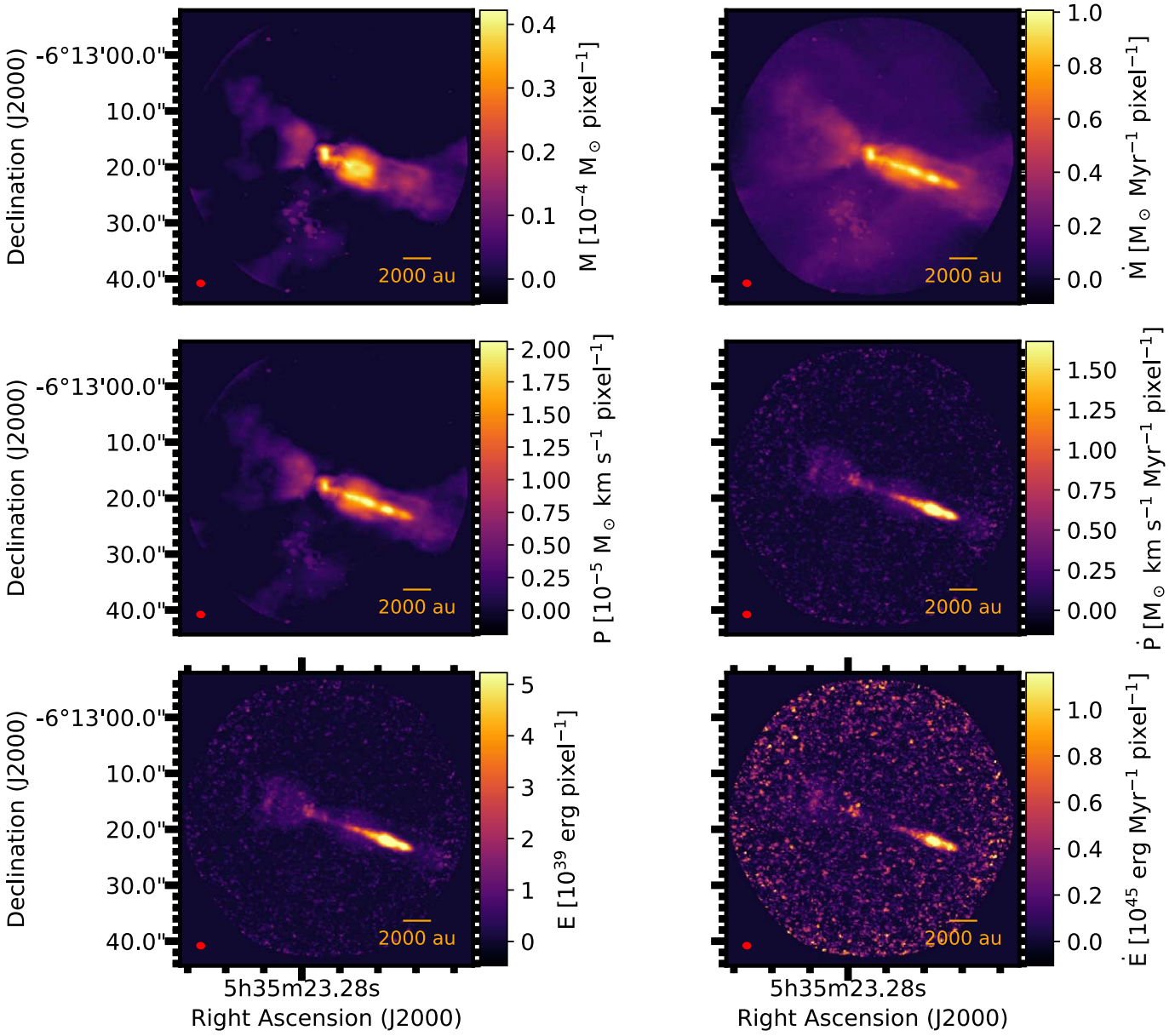

Figure 41. HOPS 198 outflow mass, momentum, energy maps, and the corresponding instantaneous rate maps. Note that the pixel size is $0\farcs17 \times 0\farcs17$. The red ellipses in the bottom left of the plots represent the synthesized beam.

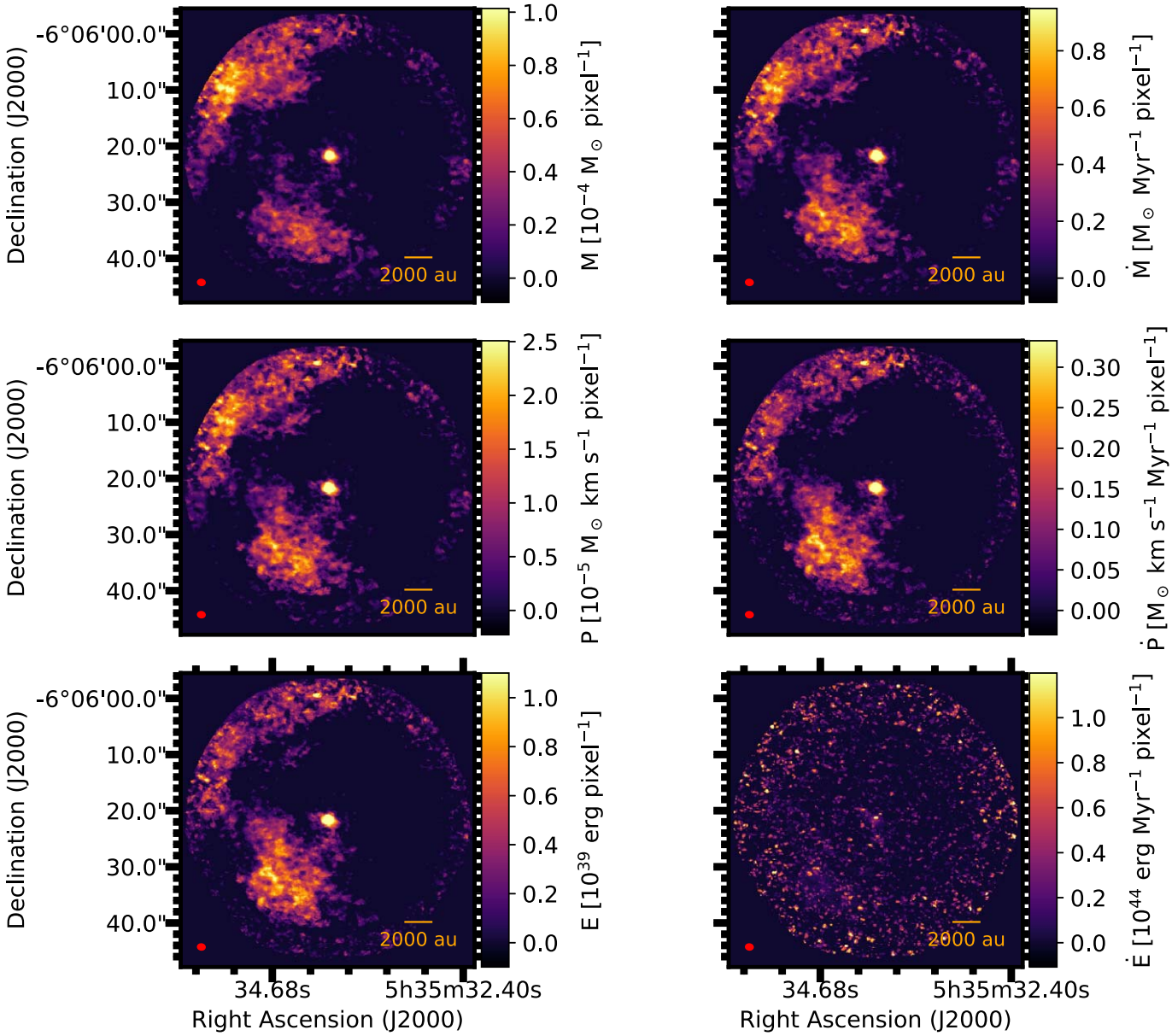

Figure 42. HOPS 200 outflow mass, momentum, energy maps, and the corresponding instantaneous rate maps. Note that the pixel size is $0\farcs17 \times 0\farcs17$. The red ellipses in the bottom left of the plots represent the synthesized beam.

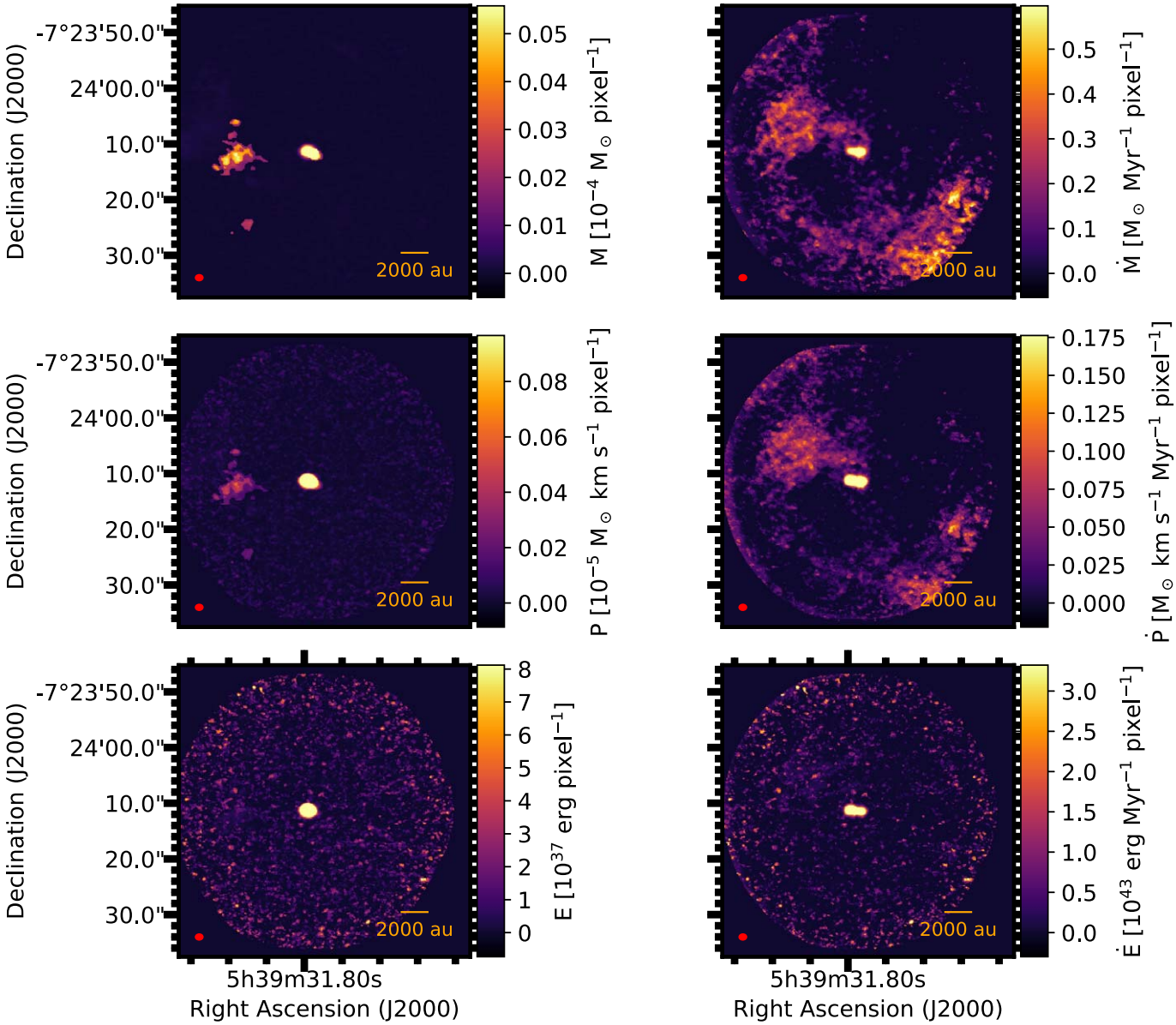

Figure 43. HOPS 408 outflow mass, momentum, energy maps, and the corresponding instantaneous rate maps. Note that the pixel size is $0\farcs17 \times 0\farcs17$. The red ellipses in the bottom left of the plots represent the synthesized beam.

Appendix G
Outflow Opening Angle, Momentum Opening Angle, and Energy Opening Angle

In this section, we present all the measurements for the traditional outflow cavity opening angle, momentum opening angle, and energy opening angle (see Tables 18 and 19).

Table 18
Summary of Outflow Opening Angles without Inclination Correction

Source	Traditional Opening Angle[a] (deg)	Momentum Opening Angle[a] (deg)	Energy Opening Angle[a] (deg)
HOPS 10	$38.0 \pm 3.4/62.6 \pm 3.6$	$77.1 \pm 12.7/48.6 \pm 2.8$	$23.3 \pm 2.6/64.4 \pm 4.7$
HOPS 11	$117.2 \pm 23.7/118.6 \pm 5.0$	$42.0 \pm 3.8/40.6 \pm 4.7$	$30.1 \pm 2.8/84.6 \pm 5.7$
HOPS 13	$50.0 \pm 2.4/57.6 \pm 5.6$	NA/NA	NA/NA
HOPS 127	$77.9 \pm 5.6/62.9 \pm 4.3$	NA/112.7 ± 9.1	NA/130.7 ± 32.5
HOPS 129	75.6 ± 6.4/NA	$45.2 \pm 8.0/82.9 \pm 6.5$	$38.6 \pm 5.6/56.7 \pm 7.5$
HOPS 130	68.3 ± 8.1/NA	91.9 ± 13.1/NA	143.6 ± 14.6/NA
HOPS 134	131.5 ± 17.1/NA	NA/NA	NA/NA
HOPS 135	NA/71.3 ± 5.3	NA/64.6 ± 4.2	$40.1 \pm 2.5/62.6 \pm 4.3$
HOPS 150[b]	NA/NA	106.1 ± 11.7/NA	NA/NA
HOPS 157	110.2 ± 11.0/NA	NA/NA	NA/NA
HOPS 164	$45.0 \pm 3.0/29.3 \pm 0.5$	$56.4 \pm 3.3/32.4 \pm 1.8$	$45.8 \pm 1.8/26.0 \pm 0.7$
HOPS 166	NA/NA	NA/NA	NA/155.5 ± 82.4
HOPS 169	$67.6 \pm 5.9/45.6 \pm 1.6$	$34.0 \pm 2.2/35.5 \pm 3.3$	$36.3 \pm 2.7/23.2 \pm 1.2$
HOPS 177	$134.9 \pm 19.0/91.6 \pm 12.0$	NA/NA	112.0 ± 5.2/NA
HOPS 185	$112.2 \pm 13.9/92.2 \pm 11.3$	NA/97.5 ± 8.0	NA/98.0 ± 7.2
HOPS 191	$113.2 \pm 8.7/77.6 \pm 8.5$	$83.8 \pm 4.7/71.6 \pm 5.7$	NA/NA
HOPS 194	NA/110.0 ± 11.1	NA/NA	NA/NA
HOPS 198	69.9 ± 4.5/NA	$60.0 \pm 3.7/66.3 \pm 3.7$	34.4 ± 4.1/NA
HOPS 200	137.2 ± 20.7/NA	NA/NA	NA/NA
HOPS 355	$24.3 \pm 1.3/34.3 \pm 1.5$	$31.2 \pm 1.6/27.1 \pm 1.8$	$40.8 \pm 5.4/26.3 \pm 3.3$
HOPS 408	NA/NA	$37.2 \pm 2.4/24.5 \pm 1.3$	$26.4 \pm 4.5/24.0 \pm 8.9$

Notes.
[a] For each source we give two estimates. The first value is the estimate for the blueshifted lobe and the second value is for the redshifted lobe. NA indicates the Gaussian fit used to derive the opening angle was not good, it did not converge or there is simply no outflow lobe for that source. The opening angle is defined as the FWQM of the fitted Gaussian.
[b] HOPS 150 is a binary system and it is contaminated by two collimated molecular outflows from two nearby sources. The Gaussian fits performed poorly for HOPS 150.
[c] HOPS 194 opening angle is measured directly from the $C^{18}O$ outflow cavity as shown in Figure 2. The uncertainty is adopted to be 10% of the measurement.

Table 19
Summary of the Outflow Opening Angles with Inclination Correction

Source	Traditional Opening Angle[a] (deg)	Momentum Opening Angle[a] (deg)	Energy Opening Angle[a] (deg)
HOPS 10	33.2 ± 2.9/55.5 ± 3.1	69.2 ± 11.0/42.7 ± 2.4	20.2 ± 2.3/57.2 ± 4.1
HOPS 11	64.4 ± 9.2/65.9 ± 1.9	16.8 ± 1.5/16.2 ± 1.8	11.8 ± 1.1/38.6 ± 2.2
HOPS 13	44.7 ± 2.1/51.7 ± 4.9	NA/NA	NA/NA
HOPS 127	65.8 ± 4.5/52.1 ± 3.4	NA/100.5 ± 7.3	NA/120.3 ± 26.3
HOPS 129	63.6 ± 5.1/NA	36.8 ± 6.4/70.5 ± 5.2	31.3 ± 4.5/46.7 ± 6.0
HOPS 130	65.3 ± 7.7/NA	88.6 ± 12.4/NA	141.6 ± 13.8/NA
HOPS 134	101.6 ± 9.5/NA	NA/NA	NA/NA
HOPS 135	NA/62.0 ± 4.4	NA/55.8 ± 3.5	34.0 ± 2.1/54.0 ± 3.6
HOPS 150[b]	NA/NA	79.8 ± 7.4/NA	NA/NA
HOPS 157	70.9 ± 5.5/NA	NA/NA	NA/NA
HOPS 164	35.4 ± 2.3/22.8 ± 0.4	44.9 ± 2.5/25.3 ± 1.4	36.1 ± 1.4/20.2 ± 0.5
HOPS 166	NA/NA	NA/NA	NA/116.1 ± 33.9
HOPS 169	46.7 ± 3.8/30.3 ± 1.0	22.3 ± 1.4/23.3 ± 2.1	23.9 ± 1.7/15.1 ± 0.8
HOPS 177	127.5 ± 16.0/81.7 ± 10.1	NA/NA	102.6 ± 4.4/NA
HOPS 185	108.2 ± 12.9/88.0 ± 10.5	NA/93.3 ± 7.4	NA/93.8 ± 6.7
HOPS 191	108.5 ± 8.0/72.8 ± 7.8	78.9 ± 4.3/66.9 ± 5.2	NA/NA
HOPS 194	NA/65.1 ± 5.0	NA/NA	NA/NA
HOPS 198	69.1 ± 4.4/NA	59.3 ± 3.6/65.5 ± 3.6	33.9 ± 4.0/NA
HOPS 200	134.6 ± 19.4/NA	NA/NA	NA/NA
HOPS 355	11.9 ± 0.6/17.0 ± 0.7	15.4 ± 0.8/13.3 ± 0.9	20.4 ± 2.6/12.9 ± 1.6
HOPS 408	NA/NA	32.2 ± 2.1/21.1 ± 1.1	22.7 ± 3.9/20.7 ± 7.6

Notes.
[a] For each source we give two estimates. The first value is the estimate for the blueshifted lobe and the second value is for the redshifted lobe. NA indicates the Gaussian fit used to derive the opening angle was not good, it did not converge or there is simply no outflow lobe for that source. The opening angle is defined as the FWQM of the fitted Gaussian. The errors are from the uncertainty of the Gaussian fit.
[b] HOPS 150 is a binary system and it is contaminated by two collimated molecular outflows from two nearby sources. The Gaussian fits performed poorly for HOPS 150.
[c] HOPS 194 opening angle is measured directly from the $C^{18}O$ outflow cavity as shown in Figure 2. The uncertainty is adopted to be 10% of the measurement.

ORCID iDs

Cheng-Han Hsieh (謝承翰) https://orcid.org/0000-0003-2803-6358
Héctor G. Arce https://orcid.org/0000-0001-5653-7817
Zhi-Yun Li https://orcid.org/0000-0002-7402-6487
Michael Dunham https://orcid.org/0000-0003-0749-9505
Stella Offner https://orcid.org/0000-0003-1252-9916
Ian W. Stephens https://orcid.org/0000-0003-3017-4418
Amelia Stutz https://orcid.org/0000-0003-2300-8200
Tom Megeath https://orcid.org/0000-0001-7629-3573
Shuo Kong https://orcid.org/0000-0002-8469-2029
Adele Plunkett https://orcid.org/0000-0002-9912-5705
John J. Tobin https://orcid.org/0000-0002-6195-0152
Yichen Zhang https://orcid.org/0000-0001-7511-0034
Diego Mardones https://orcid.org/0000-0002-5065-9175
Jaime E. Pineda https://orcid.org/0000-0002-3972-1978
Thomas Stanke https://orcid.org/0000-0002-5812-9232
John Carpenter https://orcid.org/0000-0003-2251-0602

References

Alves, J., Lombardi, M., & Lada, C. J. 2007, A&A, 462, L17
André, P., Di Francesco, J., Ward-Thompson, D., et al. 2014, in Protostars and Planets VI, ed. H. Beuther et al. (Tuscon, AZ: Univ. Arizona Press), 27
André, P., Men'shchikov, A., Bontemps, S., et al. 2010, A&A, 518, L102
Arce, H. G., & Goodman, A. A. 2001, ApJ, 554, 132
Arce, H. G., Mardones, D., Corder, S. A., et al. 2013, ApJ, 774, 39
Arce, H. G., & Sargent, A. I. 2006, ApJ, 646, 1070
Arce, H. G., Shepherd, D., Gueth, F., et al. 2007, in Protostars and Planets V, ed. B. Reipurth, D. Jewitt, & K. Keil (Tuscon, AZ: Univ. Arizona Press), 245
Bally, J. 2008, in Handbook of Star Forming Regions, Volume I: The Northern Sky, ed. B. Reipurth (San Francisco, CA: ASP), 459
Bally, J. 2016, ARA&A, 54, 491
Bontemps, S., Andre, P., Terebey, S., et al. 1996, A&A, 311, 858
Bradshaw, C., Offner, S. S. R., & Arce, H. G. 2015, ApJ, 802, 86
Bryan, G. L., Norman, M. L., O'Shea, B. W., et al. 2014, ApJS, 211, 19
Cabrit, S., & Bertout, C. 1992, A&A, 261, 274
Chen, H., Myers, P. C., Ladd, E. F., et al. 1995, ApJ, 445, 377
Cunningham, A. J., Klein, R. I., Krumholz, M. R., et al. 2011, ApJ, 740, 107
Curtis, E. I., Richer, J. S., Swift, J. J., et al. 2010, MNRAS, 408, 1516
Downes, T. P., & Cabrit, S. 2007, A&A, 471, 873
Duarte-Cabral, A., Bontemps, S., Motte, F., et al. 2013, A&A, 558, A125
Dunham, M. M., Allen, L. E., Evans, N. J., et al. 2015, ApJS, 220, 11
Dunham, M. M., Arce, H. G., Mardones, D., et al. 2014, ApJ, 783, 29
Dunham, M. M., Crapsi, A., Evans, N. J., et al. 2008, ApJS, 179, 249
Dunham, M. M., Stutz, A. M., Allen, L. E., et al. 2014, in Protostars and Planets VI, ed. H. Beuther et al. (Tuscon, AZ: Univ. Arizona Press), 195
Enoch, M. L., Evans, N. J., Sargent, A. I., et al. 2008, ApJ, 684, 1240
Feddersen, J. R., Arce, H. G., Kong, S., et al. 2020, ApJ, 896, 11
Fischer, W. J., Megeath, S. T., Furlan, E., et al. 2020, ApJ, 905, 119
Frank, A., Ray, T. P., Cabrit, S., et al. 2014, in Protostars and Planets VI, ed. H. Beuther et al. (Tuscon, AZ: Univ. Arizona Press), 451
Frerking, M. A., Langer, W. D., & Wilson, R. W. 1982, ApJ, 262, 590
Furlan, E., Fischer, W. J., Ali, B., et al. 2016, ApJS, 224, 5
Gratier, P., Pety, J., Bron, E., et al. 2021, A&A, 645, A27
Guszejnov, D., Grudić, M. Y., Hopkins, P. F., et al. 2021, MNRAS, 502, 3646
Guszejnov, D., Grudić, M. Y., Offner, S. S. R., et al. 2022, MNRAS, 515, 4929
Guszejnov, D., Markey, C., Offner, S. S. R., et al. 2022, MNRAS, 515, 167
Habel, N. M., Megeath, S. T., Booker, J. J., et al. 2021, ApJ, 911, 153
Hatchell, J., Fuller, G. A., & Richer, J. S. 2007, A&A, 472, 187
Hirano, N., Ho, P. P. T., Liu, S.-Y., et al. 2010, ApJ, 717, 58

Hsieh, C.-H., Arce, H. G., Mardones, D., et al. 2021, ApJ, 908, 92
Hsieh, C.-H., Hu, Y., Lai, S.-P., et al. 2019, ApJ, 873, 16
Hsieh, T.-H., Lai, S.-P., & Belloche, A. 2017, AJ, 153, 173
Hull, C. L. H., Girart, J. M., Kristensen, L. E., et al. 2016, ApJL, 823, L27
Jørgensen, J. K., Johnstone, D., Kirk, H., et al. 2008, ApJ, 683, 822
Jørgensen, J. K., Visser, R., Williams, J. P., et al. 2015, A&A, 579, A23
Kang, M., Choi, M., Wyrowski, F., et al. 2021, ApJS, 255, 2
Kauffmann, J., Bertoldi, F., Bourke, T. L., et al. 2008, A&A, 487, 993
Kim, M.-R., Lee, C. W., Dunham, M. M., et al. 2016, ApJS, 225, 26
Kong, S., Arce, H. G., Feddersen, J. R., et al. 2018, ApJS, 236, 25
Kong, S., Arce, H. G., Shirley, Y., et al. 2021, ApJ, 912, 156
Konigl, A., & Pudritz, R. E. 2000, in Protostars and Planets IV, ed. V. Mannings, A. P. Boss, & S. S. Russell (Tuscon, AZ: Univ. Arizona Press), 759
Könyves, V., André, P., Men'shchikov, A., et al. 2015, A&A, 584, A91
Kounkel, M., Megeath, S. T., Poteet, C. A., et al. 2016, ApJ, 821, 52
Kristensen, L. E., & Dunham, M. M. 2018, A&A, 618, A158
Ladd, E. F., Fuller, G. A., & Deane, J. R. 1998, ApJ, 495, 871
Lane, J., Kirk, H., Johnstone, D., et al. 2016, ApJ, 833, 44
Langer, W. D., & Penzias, A. A. 1993, ApJ, 408, 539
Lee, C.-F. 2020, A&ARv, 28, 1
Lee, C.-F., Mundy, L. G., Reipurth, B., et al. 2000, ApJ, 542, 925
Lee, C.-F., Tabone, B., Cabrit, S., et al. 2021, ApJL, 907, L41
Li, P. S., & Klein, R. I. 2019, MNRAS, 485, 4509
Li, Z.-Y., & Shu, F. H. 1996, ApJ, 472, 211
Lombardi, M., Bouy, H., Alves, J., et al. 2014, A&A, 566, A45
Machida, M. N., & Hosokawa, T. 2013, MNRAS, 431, 1719
Masson, C. R., & Chernin, L. M. 1993, ApJ, 414, 230
Matzner, C. D., & McKee, C. F. 1999, ApJL, 526, L109
Maud, L. T., Moore, T. J. T., Lumsden, S. L., et al. 2015, MNRAS, 453, 645
Megeath, S. T., Gutermuth, R., Muzerolle, J., et al. 2012, AJ, 144, 192
Megeath, S. T., Gutermuth, R., Muzerolle, J., et al. 2016, AJ, 151, 5
Megeath, S. T., Gutermuth, R. A., & Kounkel, M. A. 2022, PASP, 134, 042001
Mignone, A., Zanni, C., Tzeferacos, P., et al. 2012, ApJS, 198, 7
Motte, F., Andre, P., & Neri, R. 1998, A&A, 336, 150
Motte, F., André, P., Ward-Thompson, D., et al. 2001, A&A, 372, L41
Motte, F., Bontemps, S., Csengeri, T., et al. 2022, A&A, 662, A8
Mottram, J. C., van Dishoeck, E. F., Kristensen, L. E., et al. 2017, A&A, 600, A99
Myers, P. C. 2008, ApJ, 687, 340
Myers, P. C., & Ladd, E. F. 1993, ApJL, 413, L47
Nagy, Z., Menechella, A., Megeath, S. T., et al. 2020, A&A, 642, A137
Offner, S. S. R., & Arce, H. G. 2014, ApJ, 784, 61
Offner, S. S. R., & Chaban, J. 2017, ApJ, 847, 104
Offner, S. S. R., Lee, E. J., Goodman, A. A., et al. 2011, ApJ, 743, 91
Ostriker, E. C., Lee, C.-F., Stone, J. M., et al. 2001, ApJ, 557, 443
Oya, Y., Kibukawa, H., Miyake, S., et al. 2022, PASP, 134, 094301
Oya, Y., Sakai, N., Watanabe, Y., et al. 2018, ApJ, 863, 72
Pascucci, I., Cabrit, S., Edwards, S., et al. 2022, arXiv:2203.10068
Rabenanahary, M., Cabrit, S., Meliani, Z., et al. 2022, A&A, 664, A118
Raga, A. C., Canto, J., Calvet, N., et al. 1993, A&A, 276, 539
Rohde, P. F., Walch, S., Seifried, D., et al. 2022, MNRAS, 510, 2552
Rosen, A., & Smith, M. D. 2004, MNRAS, 347, 1097
Scandariato, G., Da Rio, N., Robberto, M., et al. 2012, A&A, 545, A19
Schwarz, K. R., Shirley, Y. L., & Dunham, M. M. 2012, AJ, 144, 115
Seale, J. P., & Looney, L. W. 2008, ApJ, 675, 427
Shu, F. H., Najita, J. R., Shang, H., et al. 2000, in Protostars and Planets IV, ed. V. Mannings, A .P. Boss, & S. S. Russell (Tuscon, AZ: Univ. Arizona Press), 789
Snell, R. L., Loren, R. B., & Plambeck, R. L. 1980, in IAU Symp. 87, Interstellar Molecules, ed. B. H. Andrew (Dordrecht: D. Reidel), 173
Solomon, P. M., Huguenin, G. R., & Scoville, N. Z. 1981, ApJL, 245, L19
Spitoni, E., Recchi, S., & Matteucci, F. 2008, A&A, 484, 743
Stanke, T., Arce, H. G., Bally, J., et al. 2022, A&A, 658, A178
Stanke, T., Smith, M. D., Gredel, R., et al. 2006, A&A, 447, 609
Stutz, A. M., Tobin, J. J., Stanke, T., et al. 2013, ApJ, 767, 36
Takahashi, S., Saito, M., Ohashi, N., et al. 2008, ApJ, 688, 344
Takemura, H., Nakamura, F., Ishii, S., et al. 2021, PASJ, 73, 487
Testi, L., & Sargent, A. I. 1998, ApJL, 508, L91
Tobin, J. J., Looney, L. W., Mundy, L. G., et al. 2007, ApJ, 659, 1404
Tobin, J. J., Offner, S. S. R., Kratter, K. M., et al. 2022, ApJ, 925, 39
Tobin, J. J., Sheehan, P. D., Megeath, S. T., et al. 2020, ApJ, 890, 130
van der Marel, N., Kristensen, L. E., Visser, R., et al. 2013, A&A, 556, A76
van Kempen, T. A., Hogerheijde, M. R., van Dishoeck, E. F., et al. 2016, A&A, 587, A17
Velusamy, T., Langer, W. D., & Thompson, T. 2014, ApJ, 783, 6
Wilson, T. L., & Matteucci, F. 1992, A&ARv, 4, 1
Wilson, T. L., Rohlfs, K., & Hüttemeister, S. 2009, in Tools of Radio Astronomy, ed. T. L. Wilson, K. Rohlfs, & S. Hüttemeister (Berlin: Springer-Verlag)
Xu, D., Offner, S. S. R., Gutermuth, R., et al. 2022a, ApJ, 926, 19
Xu, D., Offner, S. S. R., Gutermuth, R., et al. 2022b, ApJ, 941, 81
Yen, H.-W., Koch, P. M., Takakuwa, S., et al. 2017, ApJ, 834, 178
Yıldız, U. A., Kristensen, L. E., van Dishoeck, E. F., et al. 2015, A&A, 576, A109
Zhang, Y., Arce, H. G., Mardones, D., et al. 2016, ApJ, 832, 158